www.sciencemag.org/content/358/6369/eaal2052/suppl/DC1

# Supplementary Materials for

## Enzyme-free nucleic acid dynamical systems

Niranjan Srinivas,* James Parkin, Georg Seelig, Erik Winfree, David Soloveichik*

*Corresponding author. Email: niranjan@dna.caltech.edu (N.S.); david.soloveichik@utexas.edu (D.S.)

Published 15 December 2017, *Science* **358**, eaal2052 (2017)
DOI: 10.1126/science.aal2052

**This PDF file includes:**

Materials and Methods
Supplementary Text
Figs. S1 to S76
Tables S1 to S17
References

# Contents

## S1 Materials and methods

**DNA oligonucleotides.** All DNA oligonucleotides used in this study were purchased from Integrated DNA Technologies (IDT). Oligonucleotides of length less than 60 bases were ordered with HPLC purification, while those 60 bases or longer were ordered with IE-HPLC purification. Where applicable, fluorophores and quenchers were attached by IDT as well.

**Buffer conditions.** All DNA oligonucleotides were stored at 4 °C in TE buffer (10 mM Tris.HCl pH balanced to 8.0, with 1 mM EDTA.$Na_2$, purchased as 100x stock from Sigma-Aldrich). We define two buffer conditions. First, "TE/$Mg^{++}$", which was prepared by adding TE buffer containing 62.5 mM $MgCl_2$ in a ratio of 1:4 to the sample, thereby achieving a final $MgCl_2$ concentration of 12.5 mM, out of which 1 mM is bound to EDTA. Second, "TE/$Na^+$", which was prepared by adding the appropriate quantity of dry NaCl salt (purchased 99% pure from EM Science, lot number 43076317) to a given volume of TE buffer to achieve a final NaCl concentration of 0.5 M. All buffer solutions were pH adjusted to 8.0 and filtered with a 1 micron filter (Nalgene rapid-flow).

All spectrofluorimetry experiments with Designs 3, 4, and 5 reported here were performed in TE/$Na^+$ buffer. Spectrofluorimetry experiments with earlier Designs 1 and 2 were performed in TE/$Mg^{++}$ buffer.

**Quantitation of single strands.** Single strands were quantitated from absorbance at 260 nm (measured using a Thermo Scientific NanoDrop cuvette-free spectrophotometer) using calculated extinction coefficients (83). After thorough vortexing to ensure homogeneity in concentration, 3 samples of 2 µL each were typically used to measure absorbance. Two readings were taken from each sample and all data points were averaged. Typically, readings were within 2-5% of each other.

**Annealing protocol.** All annealing steps in this study were identical and were performed with an Eppendorf Mastercycler Gradient thermocycler. The samples were first heated up to 95 °C and then slowly cooled to 20 °C at the constant rate of 1 °C/min.

**Annealing Thresholds and Reporters.** Threshold complexes are an example of a class of Reporter complexes that are designed to irreversibly bind a target single-stranded molecule, thus activating fluorescence, therefore in this document they are often referred to as Reporters. For control experiments and rate constant measurements, we also have Reporters for Flux strands and Backward strands. All Reporter complexes were annealed with a 20% excess of top strand (which is labeled with quencher in each case). For experiments with Designs 3, 4, and 5, Reporters were annealed in TE/$Na^+$ buffer. For experiments with Designs 1 and 2, Reporters were annealed in TE/$Mg^{++}$ buffer.

Reporter complexes were not gel purified after annealing. Reporter complexes were annealed to have a bottom strand concentration of 5 µM, which also determines nominal concentration of Reporter since the top strand was added in excess. This procedure was chosen because of two reasons. First, accurate quantification of bottom strands leads to accurate estimates of the concentration of Reporter complex. This is important since the total concentration of Reporter complex is used for normalization of spectrofluorimetry data. In contrast, quantifying the concentration of multi-stranded complexes is relatively less accurate because of larger errors in estimating extinction coefficients. Second, since Reporter top strands have no toehold domains and are modified with quenchers, the excess addition of top strands ensures that all bottom strands form complexes, even with somewhat imperfect stoichiometry. This mitigates the chances of any active single-stranded DNA being present and ensures a stable fluorescence baseline.

**Annealing and purification of multi-stranded fuel complexes.** Each multi-stranded fuel complex (React and Produce) was prepared as follows. First, 5 nanomoles of the bottom strand was annealed with 6 nanomoles (20% excess) of each of the top strands in TE/$Mg^{++}$ buffer (at an approximate concentration of 25 μM).

After annealing, complexes were purified by non-denaturing (ND) polyacrylamide gel electrophoresis (PAGE) by running the samples on 12% gel at 150 V for approximately 6 hours. The purpose of the purification was (i) to remove the excess top strands that were added and (ii) remove multimers of the desired complexes that form due to the high concentrations in the annealing step. The acrylamide (19:1 acrylamide:bis) was diluted from 40% acrylamide stock purchased from Ambion. ND loading dye containing xylene cyanol FF in 50% glycerol was added to the React complexes, resulting in a final glycerol concentration of 10% by volume. Since the Produce complexes contain a quencher, 50% glycerol was added directly (rather than the ND loading dye) to achieve a final gycerol concentration of 10% by volume.

For Designs 3, 4, and 5, the appropriate bands were cut out and eluted in 1 mL of TE/$Na^{+}$ buffer for 18-24 hours. For Designs 1 and 2, the elution was done in TE/$Mg^{++}$ buffer instead.

**Dialysis of multi-stranded fuel complexes.** For Designs 3, 4, and 5, since the experiments were to be performed in TE/$Na^{+}$ buffer, a further reduction (approximately 2500 fold) in $Mg^{++}$ concentration was achieved using 2 rounds of dialysis. Each round of dialysis was expected to achieve a reduction of approximately 50 fold, since 1 ml of purified multi-stranded fuel complex was dialyzed with approximately 50 ml of TE/$Na^{+}$ buffer for 2 hours using a 2 ml Thermo Scientific Slide-A-Lyzer MINI dialysis device with a 10K MWCO membrane.

**Quantitation of multi-stranded fuel complexes.** The procedure for quantitating multi-stranded fuel complexes is essentially identical to the procedure for single strands, except for the calculation of extinction coefficients, which involves corrections for hyperchromicity (83). We expect the inferred concentrations to be less accurate because of larger uncertainties in the estimated extinction coefficients. Typical yields after purification ranged from 40% to 60%.

**Experimental protocols for spectrofluorimetry.** Spectrofluorimetry experiments were performed using a commercial SPEX Fluorolog-3 from Horiba, equipped with a water bath temperature controller. All spectrofluorimetry experiments were performed at 25 °C unless otherwise mentioned. Synthetic round-top quartz cuvettes (119-004F) from Hellma, with a total volume 1.6 ml, were used.

Prior to each experiment, all cuvettes were cleaned thoroughly. Each cuvette was washed 10 times in Milli-Q water, twice in 70% ethanol, and finally another 5 times in Milli-Q water. After washing, cuvettes were dried by gently tapping them on a Kimtech Science wipe placed on paper towels for cushioning. They were subsequently left to air-dry for about one hour. Cuvette caps were washed once thoroughly with Milli-Q water, once with 70% ethanol, and once again with Milli-Q water. They were then dried with Kimtech Science wipe and left to air-dry for an hour. After adding the sample, the exterior of the cuvette was washed with the same procedure as the caps.

For experiments involving the ROX fluorophore, excitation was at 584 nm, while emissions were at 602 nm. For experiments involving the Alexa-488 fluorophore, excitation was at 492 nm, while emissions were at 517 nm. For experiments involving the Alexa-647 fluorophore, excitation was at 650 nm, while emissions were at 670 nm. Band pass value of 2 nm was used for both excitation and emission monochrometers for all experiments except those measuring individual strand displacement and toehold exchange rate constants, for which a bandpass of 4 nm was used. All experiments were done with integration time of 10 seconds for each data point.

For experiments involving one fluorophore, measurements were taken every minute; for those with multiple fluorophores, measurement interval increased proportionally because each excitation/emission channel was allotted 1 minute for measurement.

**Dilution correction.** Spectrofluorimetry experiments involving the autocatalytic modules (e.g. Fig. 2 of the main text, Figs. S15, S16) and the Displacillator (e.g. Fig. S27) require the addition of Produce complexes while fluorescence data is being recorded. The volume of liquid added along with the Produce complexes is usually not negligible; in Displacillator experiments, it can be as high as 8-10% of the total volume of the reaction. This volume addition would reduce the concentration of all the fluorophores in solution, and thereby lead to a decrease in fluorescence signal that is purely due to dilution. To compensate for this effect, we introduce a dilution correction. If the volume of Produce complexes added is $\mathrm{v_P}$, and the total volume of the reaction before addition of the Produce complexes was $\mathrm{v_1}$, then we multiply all fluorescence counts after the addition by $(1 + \frac{\mathrm{v_P}}{\mathrm{v_1}})$.

## S1.1 Normalization details for spectrofluorimetry.

Here we describe our procedure[1] for normalizing fluorescence data (in AU) to get information about concentrations of the respective species (in nM). Fig. S1 describes the procedure for an experiment with an autocatalytic module; Fig. S2 illustrates the procedure for a Displacillator experiment.

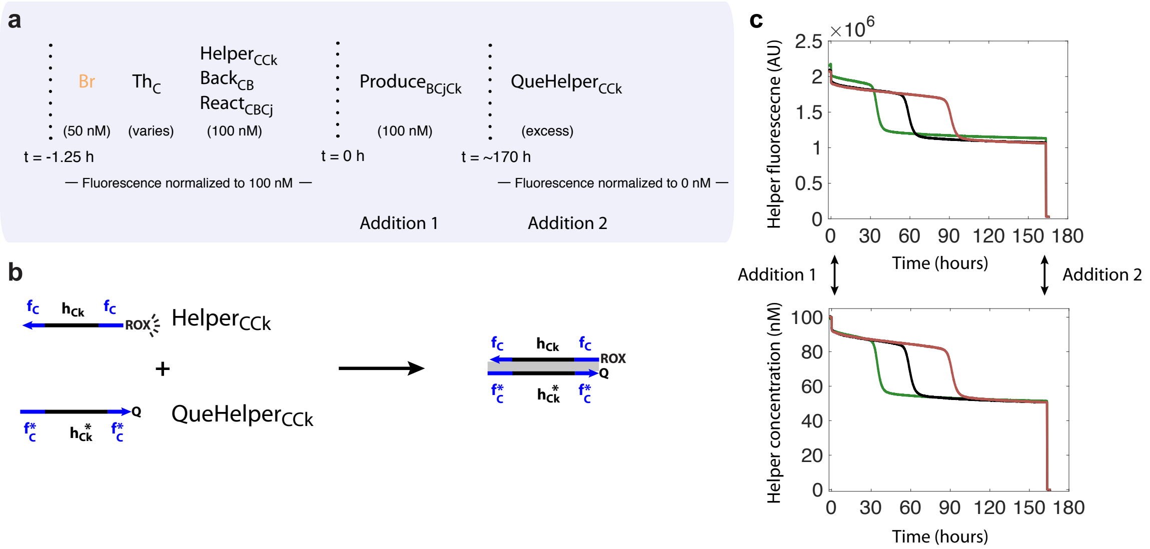

Figure S1: **Normalization procedure for autocatalytic modules.** (**a**) Experimental setup for the autocatalytic module C + B → 2 C (Design 4). Median fluorescence of the Helper strand measured for about 1.25 h (at least 25 data points) before the addition of the Produce complex was normalized to 100 nM. After the exponential amplification completes, excess QueHelper strand was added around 170 h in order to quench fluorescence of free Helper strands that remain in solution. After the quenching proceeds to completion, the median fluorescence (measured for at least 25 data points) was normalized to 0. (**b**) Mechanism of quenching by the QueHelper strands, which are essentially complements of the Helper strands with a quencher attached. (**c**) Smoothed raw data and normalized data, for comparison.

---

[1] See Section S8.3 for some differences in the procedures used for normalizing data in Design 5 only.

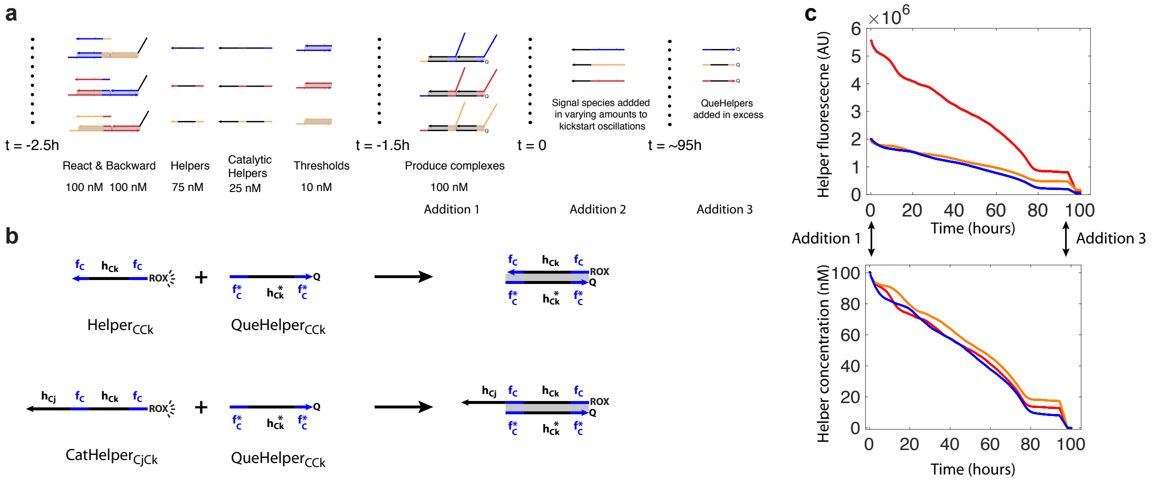

Figure S2: **Normalization procedure for the full Displacillator.** (**a**) Procedure for a Displacillator experiment (data shown from Design 4). Median fluorescence of the Helper and CatHelper strands measured for about 1.25 h (at least 25 data points) before the addition of the Produce complexes were normalized to 100 nM. After the fuel species are consumed, excess QueHelper strands were added around 95 h in order to quench the fluorescence of free Helper and CatHelper strands that remain in solution. After the quenching proceeds to completion, the median fluorescence (measured for at least 25 data points) were normalized to 0. (**b**) Mechanism of quenching of Helper and CatHelper strands by the QueHelper strands, shown for $\mathrm{Helper}_{\mathrm{CCk}}$ and $\mathrm{CatHelper}_{\mathrm{CjCk}}$ as an example. (**c**) Smoothed raw data and normalized data, for comparison.

| Reporter | Measured rate constant ( /M /s) | Diagram |
|---|---|---|
| $k_{\mathrm{RepFluxCAp}}$ | $7.7 \times 10^5$ | Fig. S53 |
| $k_{\mathrm{RepFluxBCj}}$ | $3.1 \times 10^6$ | Fig. S54 |
| $k_{\mathrm{RepFluxABr}}$ | $2.2 \times 10^6$ | Fig. S55 |
| $k_{\mathrm{RepBackBA}}$ | $6.8 \times 10^5$ | Fig. S56 |
| $k_{\mathrm{RepBackCB}}$ | $1.0 \times 10^6$ | Fig. S57 |
| $k_{\mathrm{RepBackACi2}}$ | $1.1 \times 10^5$ | Fig. S58 |

Table S1: **Independently measured rate constants for Flux Reporters (Design 4).** These Reporters respectively consume $\mathrm{Flux_{CAp}}$, $\mathrm{Flux_{BCj}}$, $\mathrm{Flux_{ABr}}$, $\mathrm{Back_{BA}}$, $\mathrm{Back_{CB}}$, and $\mathrm{Back_{ACi2}}$. All rate constants are given in /M /s, for experiments performed at 25 °C in TE buffer, pH 8.0, with 0.5 M $\mathrm{Na^+}$.

## S1.2 Characterizing individual rate constants

All experiments for measuring individual rate constants were performed at low concentrations, where the toehold occlusion effect will be negligible.

We emphasize that all data in Section S1.2 was normalized to the total concentration of the Reporter complex. This is good practice for two reasons. First, the Reporter complexes were annealed with an excess of top strand and were not gel purified. Therefore, their concentration is inferred directly from the concentration of the bottom strand. Since extinction coefficient calculations are more accurate for single strands, we believe that concentrations of the Reporter complexes are in general more accurately measured compared to fuel complexes. (Since fuel complexes are gel purified, their concentration estimates rely on extinction coefficients calculated for multi-stranded complexes, which are prone to larger errors).

### S1.2.1 Measuring Reporter rate constants

Here we describe how rate constants for triggering Reporter complexes (which also act as Thresholds for consuming initial leak of signal strands) were measured. Fig. S3 summarizes the experimental and analysis procedure for measuring $k_{\mathrm{RepA}}$. Similar experiments were performed for measuring $k_{\mathrm{RepB}}$ and $k_{\mathrm{RepC}}$. All these individual rate constants are summarized in Table S3, where they are listed as $k_{\mathrm{Th_A}}$, $k_{\mathrm{Th_B}}$, and $k_{\mathrm{Th_C}}$ respectively. Measurements similar to these were performed for Reporters for the Flux strands (see Fig. S22) and the Back strands (see Figs. S57- S56 for design diagrams). Measured rate constants for $\mathrm{RepFlux_{CAp}}$, $\mathrm{RepFlux_{BCj}}$, $\mathrm{RepFlux_{ABr}}$, $\mathrm{RepBack_{CB}}$, $\mathrm{RepBack_{ACi2}}$, and $\mathrm{RepBack_{BA}}$ are summarized in Table S1.

### S1.2.2 Measuring rate constants for desired strand displacement reactions

Table S2 summarized the independently measured rate constants for all desired strand displacement reactions. In this section we describe the experimental and analysis procedures with $\mathrm{k_{fwd1}^{CApAq}}$ and $\mathrm{k_{back}^{CApAq}}$ as illustrative examples.

Fig. S4 presents the experimental setup and data for measuring $\mathrm{k_{fwd1}^{CApAq}}$ and $\mathrm{k_{back}^{CApAq}}$. We note that exact amounts of each addition were inferred after normalization (e.g. the amounts of $\mathrm{Flux_{CAp}}$ added to Samples 1, 2, and 3 in panels b and c were inferred to be 2.2, 3.1, and 3.9 nM, respectively). The following model (say model A) was used to estimate $\mathrm{k_{fwd1}^{CApAq}}$:

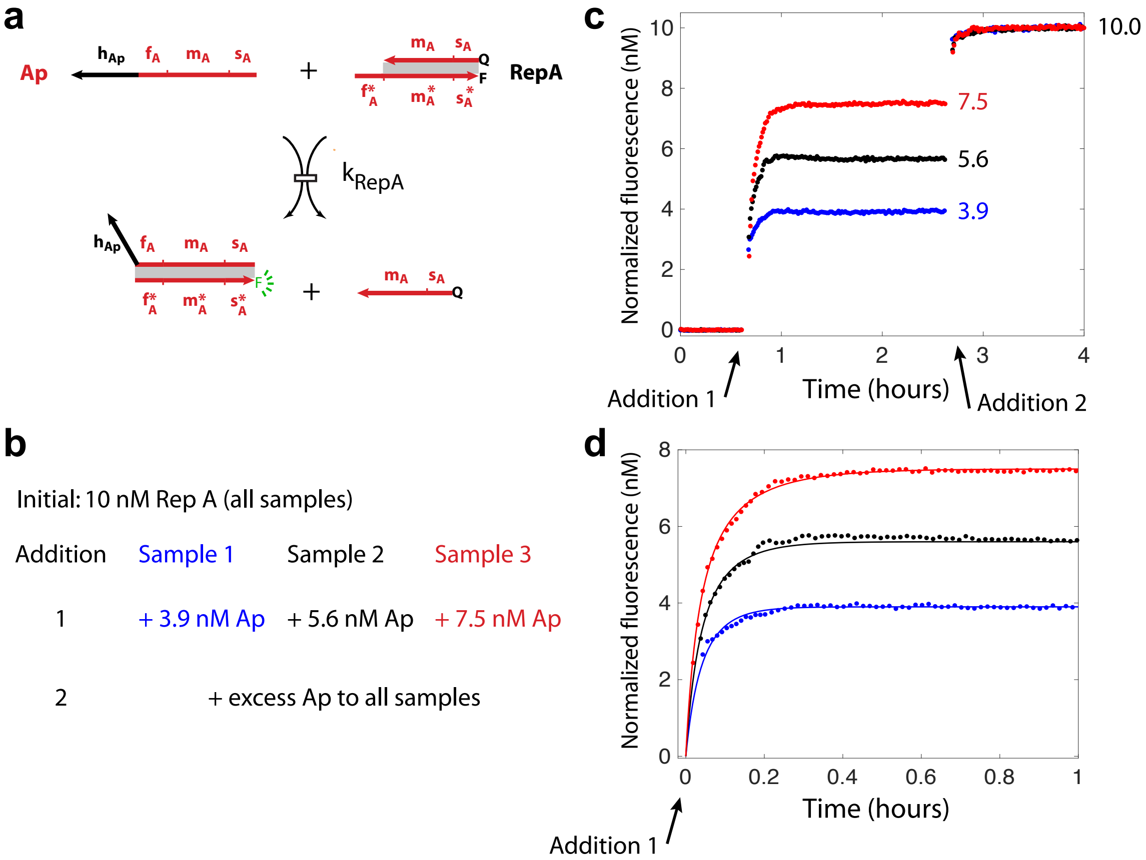

Figure S3: **Example experiment for measuring Reporter rate constants.** (**a**) Mechanism by which Ap triggers RepA. (**b**) Experimental setup. (**c**) Normalized fluorescence data (Design 4). Median baseline fluorescence of RepA before addition of Ap was normalized to 0; median fluorescence after addition of excess Ap was normalized to the initial concentration of RepA, which was 10 nM. The exact amounts of Ap added in Addition 1 were backed out from this normalization (target additions were 4, 6, and 8 nM respectively). (**d**) By fitting $\mathrm{Ap} + \mathrm{RepA} \xrightarrow{\mathrm{k_{RepA}}}$ Fluorescence to all three curves simultaneously, we obtained $k_{\mathrm{RepA}} = 7.4 \times 10^5$ /M/s.

$$\mathrm{Flux_{CAp}} + \mathrm{Produce_{CApAq}} \underset{k_{\mathrm{back}}^{\mathrm{CApAq}}}{\overset{k_{\mathrm{fwd1}}^{\mathrm{CApAq}}}{\rightleftharpoons}} \mathrm{ProduceInt_{CApAq}} + \mathrm{Ap} \tag{1}$$

$$\mathrm{Ap} + \mathrm{RepA} \xrightarrow{k_{\mathrm{RepA}}} \mathrm{Fluorescence}. \tag{2}$$

Similarly, the model below (model B) was used to estimate $\mathrm{k}_{\mathrm{back}}^{\mathrm{CApAq}}$:

$$\mathrm{Flux_{CAp}} + \mathrm{Produce_{CApAq}} \underset{k_{\mathrm{back}}^{\mathrm{CApAq}}}{\overset{k_{\mathrm{fwd1}}^{\mathrm{CApAq}}}{\rightleftharpoons}} \mathrm{ProduceInt_{CApAq}} + \mathrm{Ap} \tag{3}$$

$$\mathrm{Flux_{CAp}} + \mathrm{RepFlux_{CAp}} \xrightarrow{k_{\mathrm{RepFlux_{CAp}}}} \mathrm{Fluorescence}\ . \tag{4}$$

Since $k_{\mathrm{RepA}}$ and $k_{\mathrm{RepFlux_{CAp}}}$ were measured independently (Tables S3 and S1 respectively), the only unknown parameters were $\mathrm{k}_{\mathrm{fwd1}}^{\mathrm{CApAq}}$ and $\mathrm{k}_{\mathrm{back}}^{\mathrm{CApAq}}$. These were estimated as follows.

First, the fluorescence curves predicted by model A with $\mathrm{k}_{\mathrm{back}}^{\mathrm{CApAq}} = 0$ were fit to the data in Fig. S4d. This generated an initial estimate for $\mathrm{k}_{\mathrm{fwd1}}^{\mathrm{CApAq}}$. Similarly, the fluorescence curves predicted by model B with $\mathrm{k}_{\mathrm{fwd1}}^{\mathrm{CApAq}} = 0$ were fit to the data in Fig. S4g to generate an initial estimate of $\mathrm{k}_{\mathrm{back}}^{\mathrm{CApAq}}$. Then, model A was fit again to the data in Fig. S4d, with $\mathrm{k}_{\mathrm{back}}^{\mathrm{CApAq}}$ set to its initial estimate, to generate an updated estimate for $\mathrm{k}_{\mathrm{fwd1}}^{\mathrm{CApAq}}$. This new estimate of $\mathrm{k}_{\mathrm{fwd1}}^{\mathrm{CApAq}}$ was used to re-fit model B to the data in Fig. S4g to generate an updated estimate for $\mathrm{k}_{\mathrm{back}}^{\mathrm{CApAq}}$. This procedure was repeated until both estimates changed by less than 10%. The final values are summarized in Table S2.

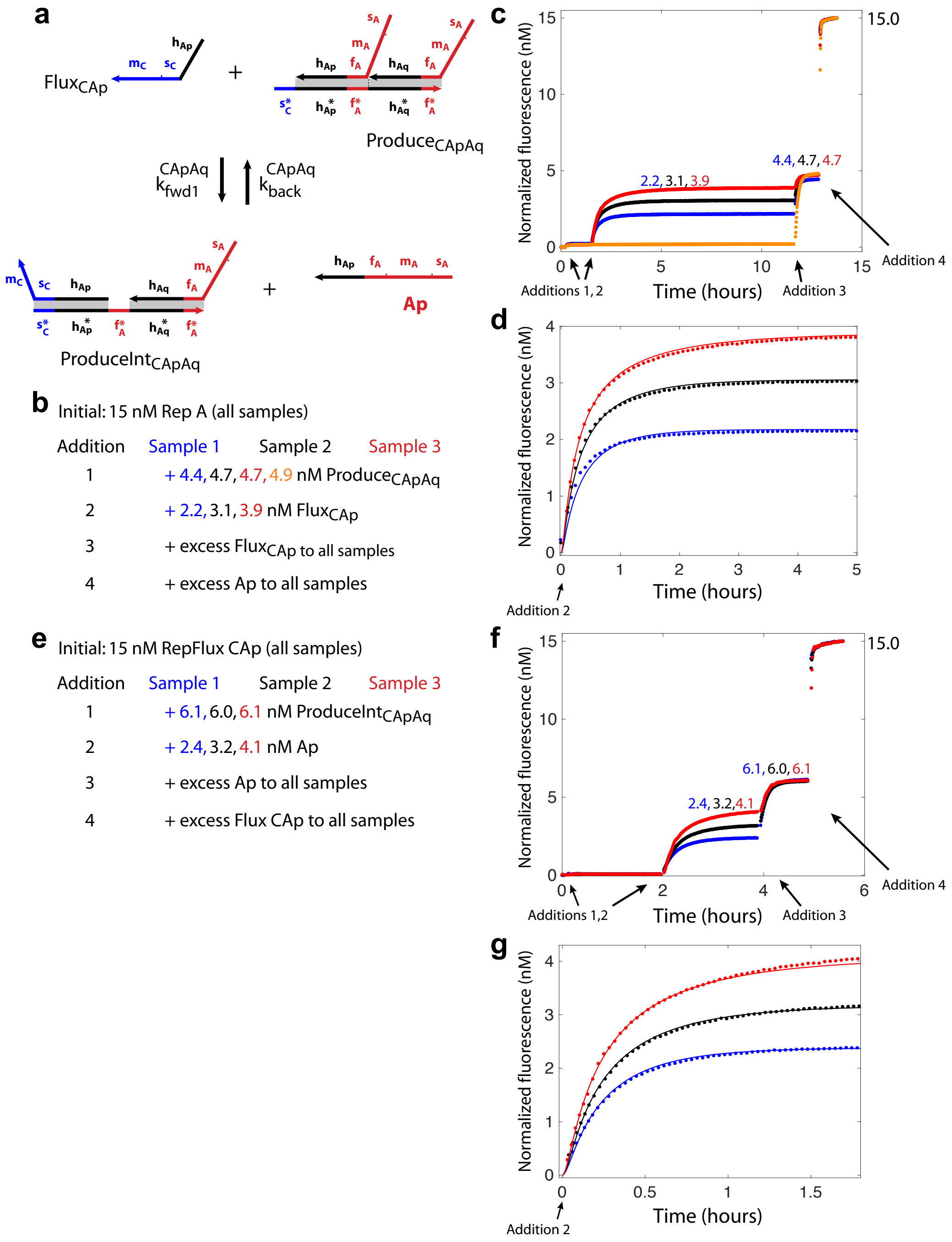

**b** Initial: 15 nM Rep A (all samples)

| Addition | Sample 1 | Sample 2 | Sample 3 |
|---|---|---|---|
| 1 | + 4.4, 4.7, 4.7, 4.9 nM Produce$_{CApAq}$ | | |
| 2 | + 2.2, 3.1, 3.9 nM Flux$_{CAp}$ | | |
| 3 | + excess Flux$_{CAp}$ to all samples | | |
| 4 | + excess Ap to all samples | | |

**e** Initial: 15 nM RepFlux CAp (all samples)

| Addition | Sample 1 | Sample 2 | Sample 3 |
|---|---|---|---|
| 1 | + 6.1, 6.0, 6.1 nM ProduceInt$_{CApAq}$ | | |
| 2 | + 2.4, 3.2, 4.1 nM Ap | | |
| 3 | + excess Ap to all samples | | |
| 4 | + excess Flux CAp to all samples | | |

Figure S4: **Example procedure for measuring reversible reactions in the react and produce steps.** (**a**) Reversible toehold exchange reaction in the produce step for A + C → 2 A. (**b**) Experimental setup for measuring $\mathrm{k_{fwd1}^{CApAq}}$. (**c**) Fluorescence data (Design 4). The orange curve represents Sample 4, which is an un-triggered control. Median baseline fluorescence of $\mathrm{RepA}$ is normalized to 0; median fluorescence after Addition 4 is normalized to initial concentration of $\mathrm{RepA}$ (15 nM). (**d**) Model fits as described in Section S1.2.2. (**e**) Experimental setup for measuring $\mathrm{k_{back}^{CApAq}}$. (**f**) Fluorescence data. Median baseline fluorescence of $\mathrm{RepFlux_{CAp}}$ is normalized to 0; median fluorescence after Addition 4 is normalized to the initial concentration of $\mathrm{RepFlux_{CAp}}$ (15 nM). (**g**) Model fits, as described in Section S1.2.2.

# S2 CRN-to-DNA implementation scheme: Additional details

## S2.1 History domain

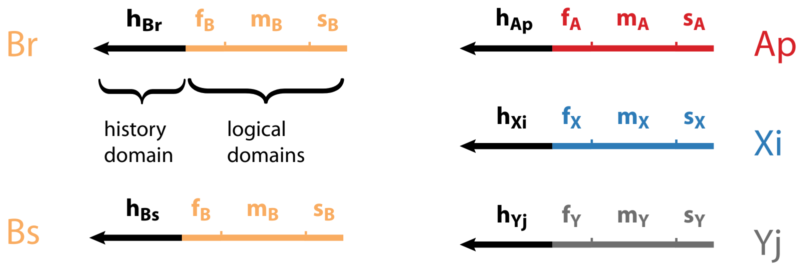

Figure S5: **Domain types for signal strands.** Each signal strand comprises a history domain in black (e.g. $\mathrm{h_{Br}}$) and a logical unit that comprises three domains: the first toehold (e.g. $\mathrm{f_B}$), a branch migration region (e.g. $\mathrm{m_B}$), and the second toehold (e.g. $\mathrm{s_B}$). The logical unit is common to all signal strands that represent a particular formal species; the history domain is specific to a particular position on the Produce complex. The domains in the logical unit participate in all desired strand displacement reactions (e.g. Fig. S9). The history domain facilitates correct annealing of the Produce complex. Signal strands with the same logical unit (e.g. Br and Bs) represent the same formal species (B) and are designed to behave identically in solution.

## S2.2 Naming scheme

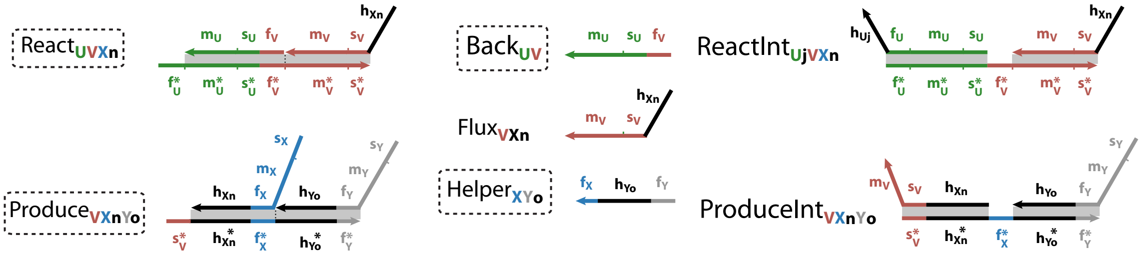

Figure S6: **Molecular complex naming convention.** Our naming scheme is illustrated with the molecules used in the general reaction $\mathrm{U} + \mathrm{V} \rightarrow \mathrm{X} + \mathrm{Y}$ as an example. The scheme is both precise and general – the name and the molecule fully determine each other. Note that each molecule only captures the reactivity and logical function of that molecule: e.g. neither the name $\mathrm{React_{UVXn}}$ nor the corresponding molecule encode any information about the second output released downstream during the produce step. Similarly, $\mathrm{Flux_{VXn}}$ does not include any information about the species U that was consumed to release it. Also, each molecule is fully determined by its name: e.g. $\mathrm{ReactInt_{UjVXn}}$ includes the specific history domain $\mathrm{h_{Uj}}$, which keeps track of the particular signal strand Uj. The waste complexes (not shown) also have precise and general names.

# S3 Molecular implementation of autocatalytic single-reaction CRNs

## S3.1 Detailed specification of the desired reaction pathways

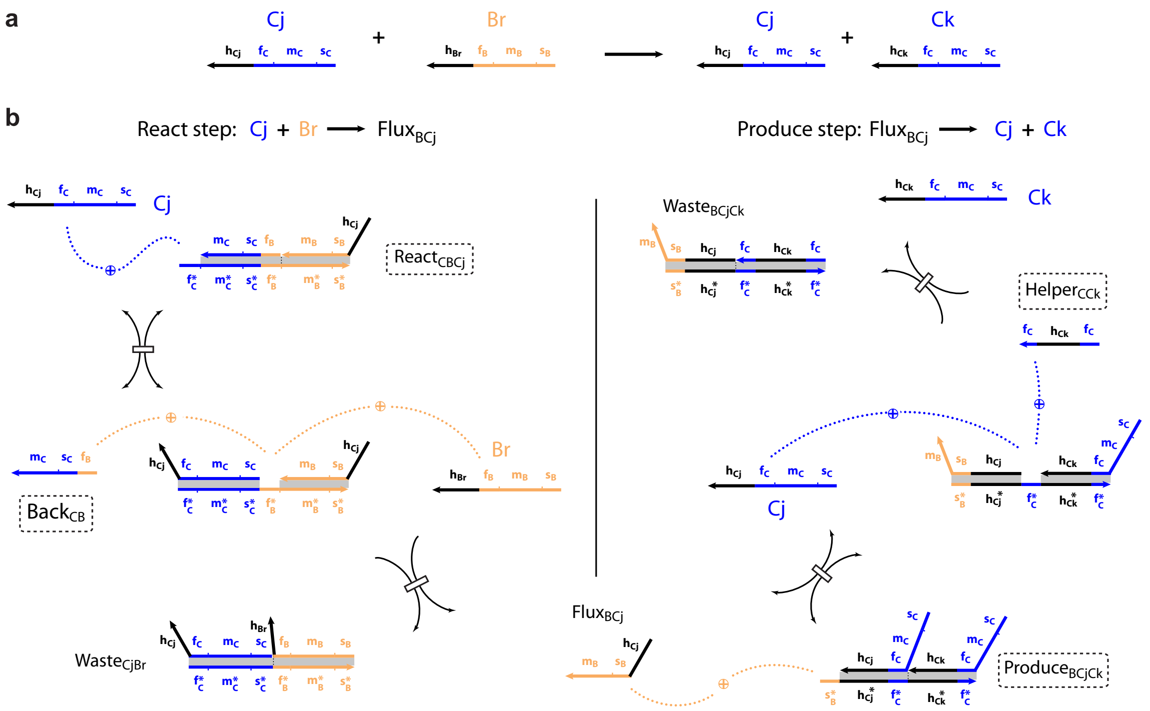

Figure S7: **DNA implementation for C + B → 2 C.** Dashed box indicates fuel species. (**a**) Net reaction. (**b**) Detailed reaction pathway.

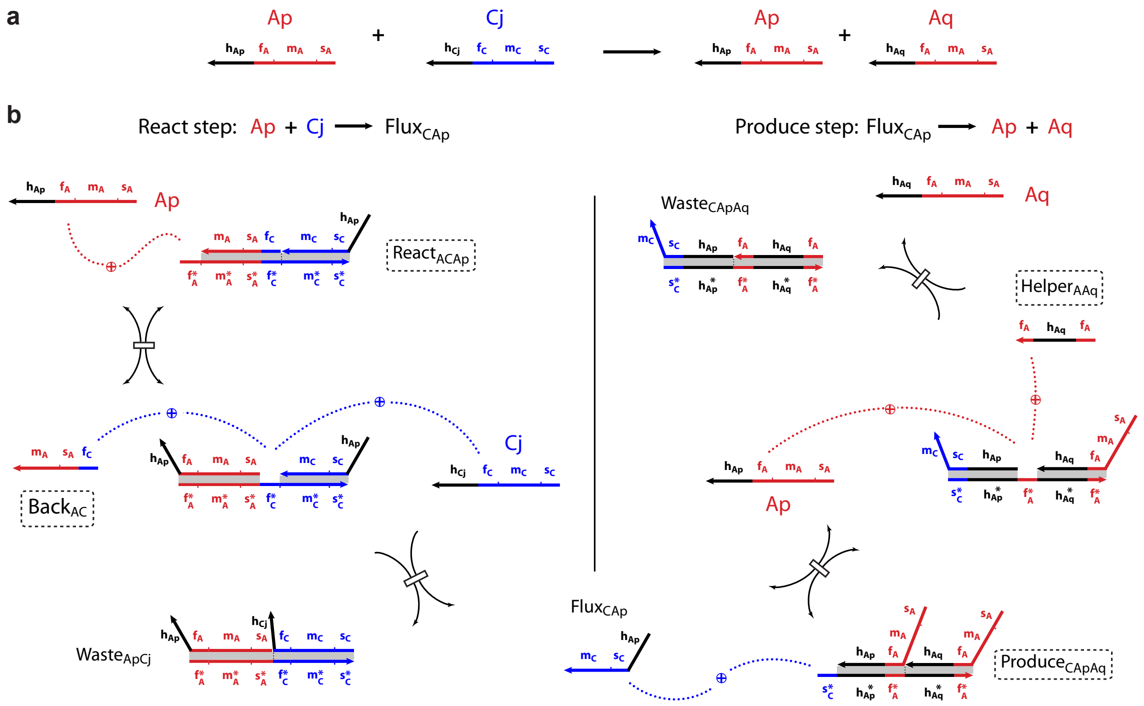

Figure S8: **DNA implementation for $\mathbf{A} + \mathbf{C} \rightarrow 2\,\mathbf{A}$.** Dashed box indicates fuel species. (**a**) Net reaction. (**b**) Detailed reaction pathway.

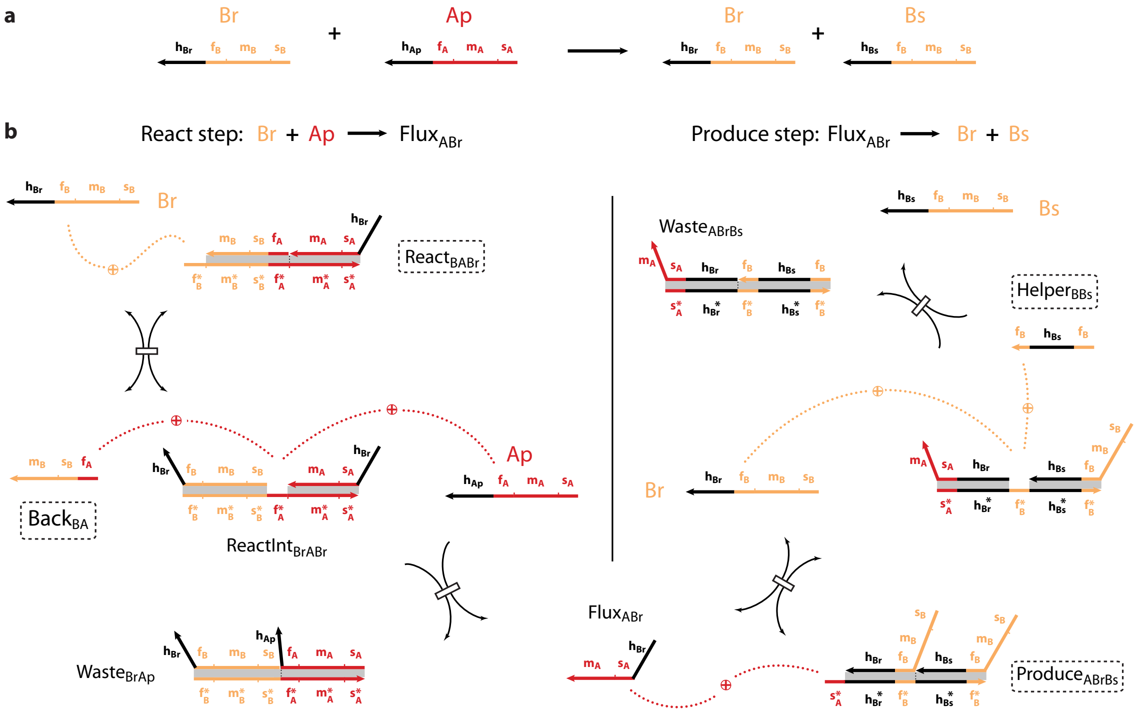

Figure S9: **DNA implementation for B + A → 2 B.** Dashed box indicates fuel species. (**a**) Net reaction. (**b**) Detailed reaction pathway.

## S3.2 Proposed molecular mechanisms for leak reactions

These leak pathways were first encountered in the context of our efforts to engineer autocatalytic single-reaction CRNs, and are therefore presented in that context. However, these leak pathways are more general - they would be present in any DNA implementation constructed using the general scheme presented in this work.

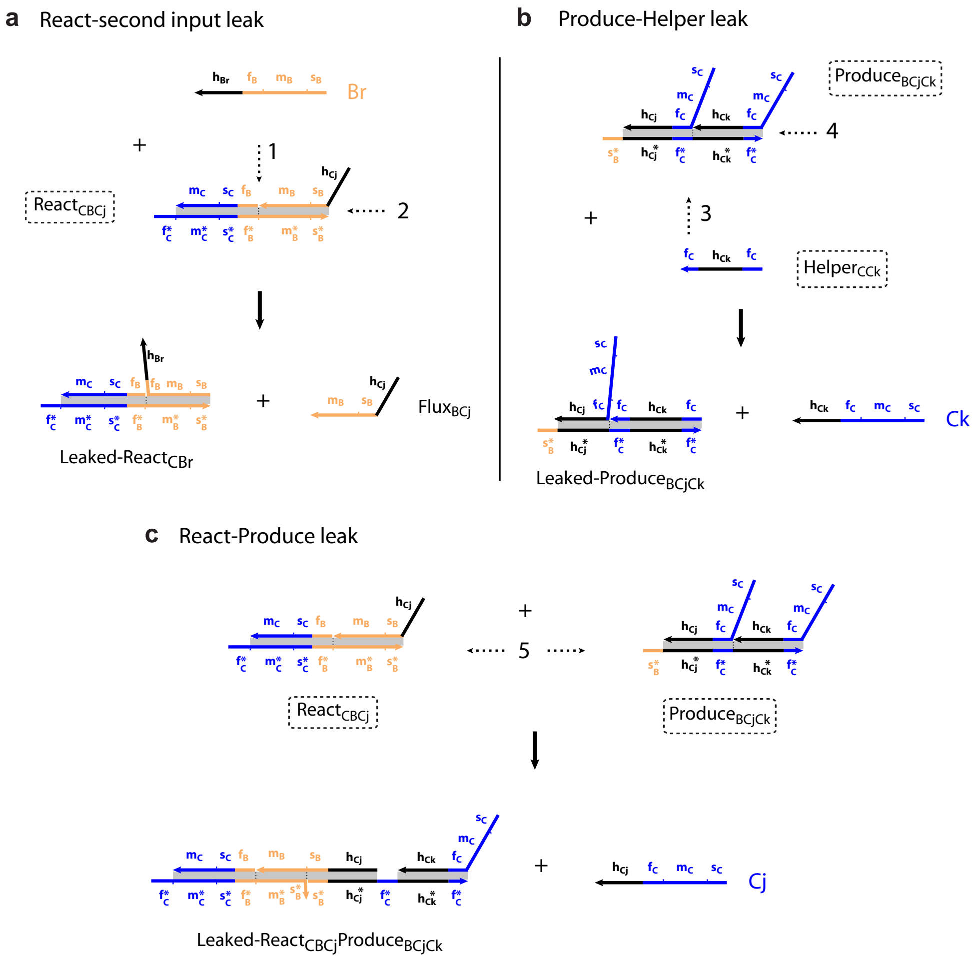

Figure S10: **Examples of leak pathways.** Numbered dashed arrows indicate locations of invasion. (**a**) The second input (here, Br) can invade at locations 1 (the junction) and 2 (the end of the helix) in the React complex. Once strand displacement finishes, the Flux strand and a spurious complex are formed. (**b**) The Helper strand and Produce complex can react similarly to release the second output (here, Ck) and a spurious complex. (**c**) Spontaneous thermal fraying at the end of the helix in the React complex may enable the Produce complex to invade at location 5, resulting in the release of the first output (here, Cj) and a spurious complex. Spurious complexes may participate in downstream reactions through legitimate strand displacement pathways (Fig. S11).

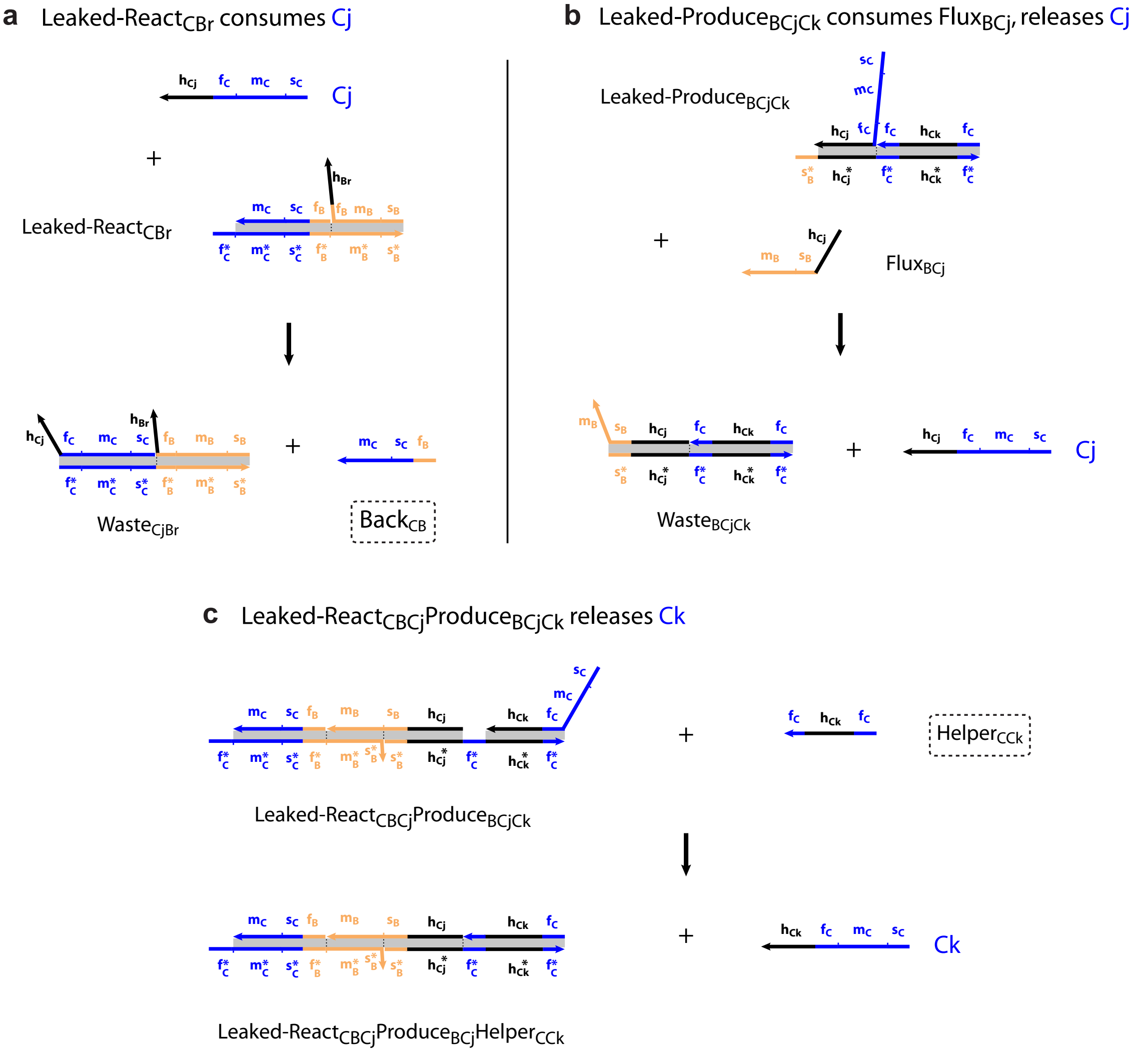

Figure S11: **Toehold-mediated reactions with products from leak reactions.** Spurious products that are formed due to leak pathways may undergo reactions that are legitimate steps in desired reaction pathways. Therefore leak reactions may affect dynamical behavior in ways that are more complex than merely the unexpected release of signal strands or Flux strands. (**a** - **c**) Downstream reactions involving products from Fig. S10a-c, respectively.

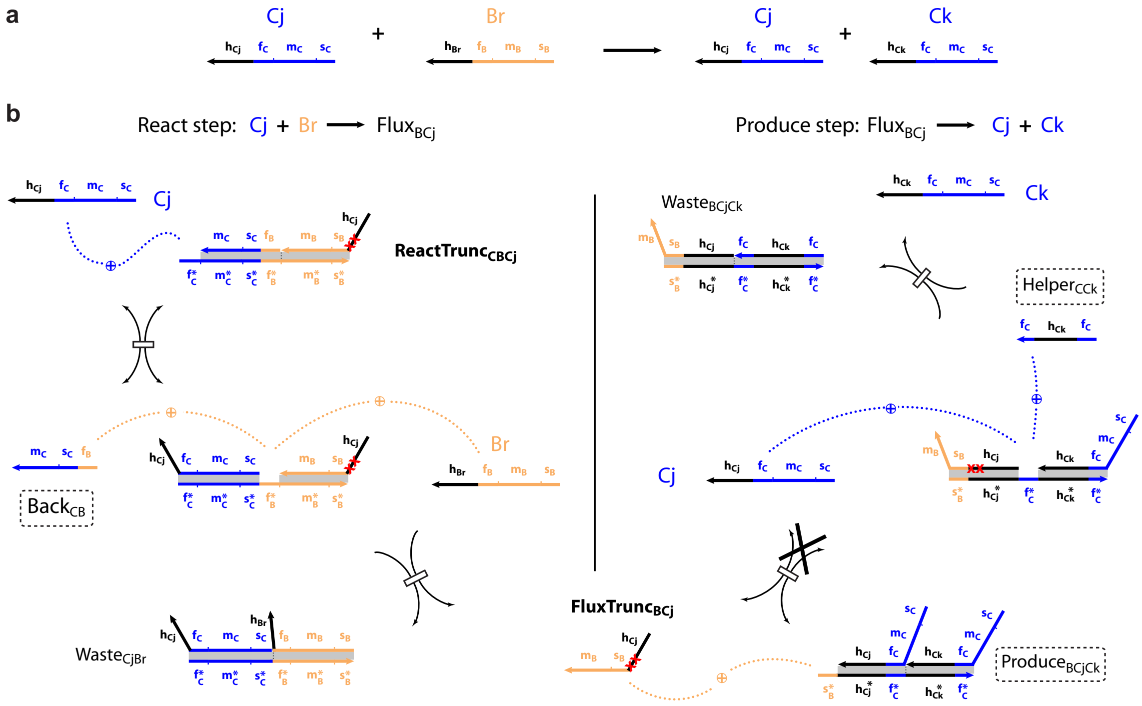

Figure S12: **Potential consequences of synthesis errors.** Synthesis errors, such as truncations, can adversely affect reaction stoichiometry in the DNA implementation. In particular, synthesis errors in toehold regions and the initial bases of branch migration domains can dramatically reduce the rates of desired strand displacement reactions. For example, for the net reaction shown in (**a**), truncations in the Flux strand (indicated by red crosses) can prevent efficient triggering of the produce step, thereby resulting in consumption of signal strands in the react step without the corresponding release of signal strands in the produce step, as illustrated in (**b**). This leads to incorrect reaction stoichiometry.

## S3.3 Toehold occlusion

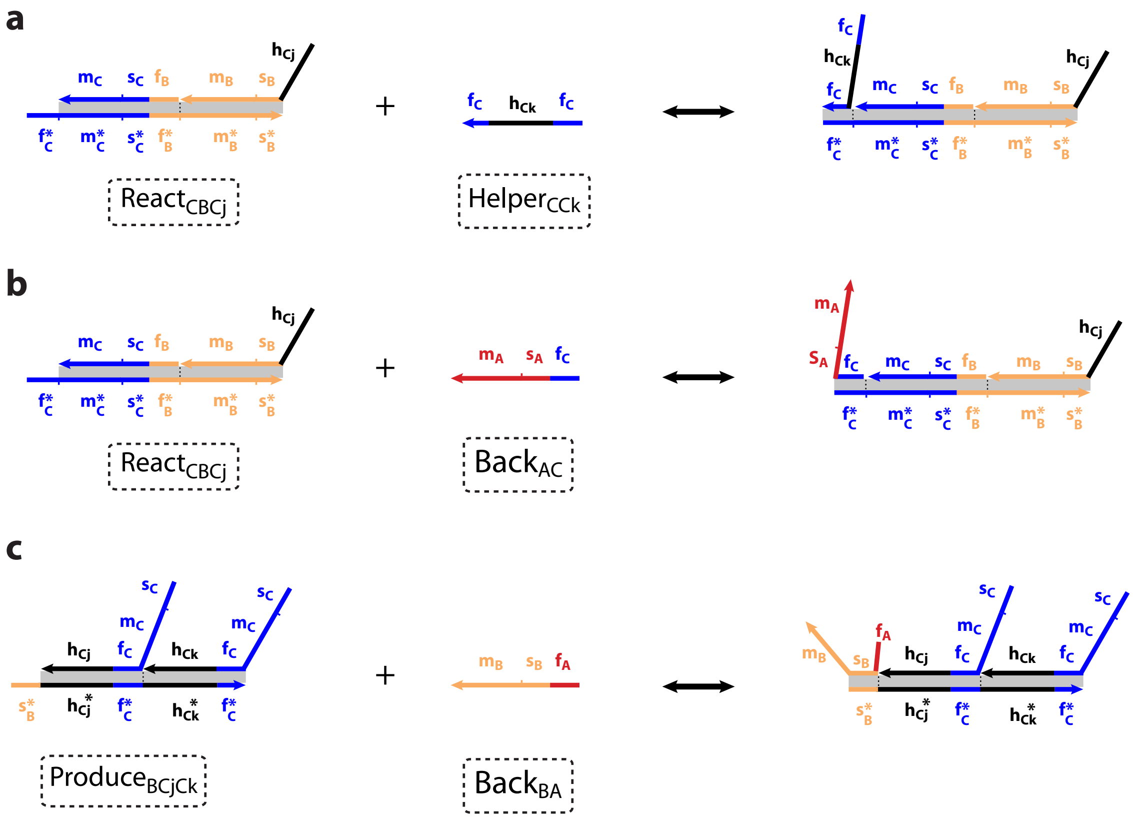

Figure S13: **Illustrative (but not exhaustive) examples of toehold-only interactions in the molecular implementation of our oscillator.** Note that all these interactions (but not all interactions) are between fuel species at high concentration. There are interactions within the same autocatalytic module (e.g. (**a**)) and across modules (e.g. (**b**), (**c**)).

### S3.4 Counteracting damping: the catalytic Helper mechanism

One way of counteracting damping and "tuning up" our Displacillator would be to engineer an alternative mechanism for the produce step where, in addition to the second output of the Produce complex, the Flux strand is also released. If that can be engineered, the Flux strand could interact with more Produce complexes and release more outputs, thereby effectively increasing output stoichiometry. Inspired by Zhang et.al. (40)'s entropy-driven catalyst, we introduced the "catalytic Helper" mechanism (see Fig. S14) to mediate such an alternative pathway. Note that in our case, the entropic benefit is a bonus and not the only reason our desired pathway is thermodynamically favorable.

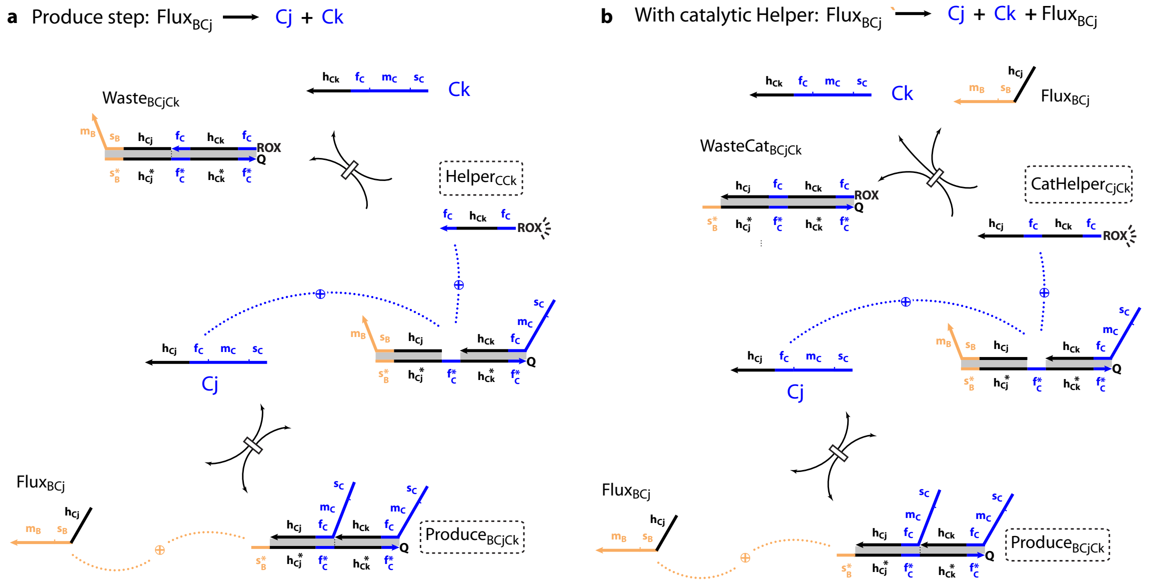

Figure S14: **Catalytic Helper mechanism.** (**a**) Produce step for the reaction $\mathrm{C} + \mathrm{B} \rightarrow 2\,\mathrm{C}$ facilitated by the traditional Helper strand. (**b**) Produce step for the reaction $\mathrm{C} + \mathrm{B} \rightarrow 2\,\mathrm{C}$ using the "catalytic Helper" strand. The catalytic Helper strand (here, $\mathrm{CatHelper}_{\mathrm{CjCk}}$) is simply the Helper strand extended at the 3' end with the history domain of the first output of the Produce complex (here, $\mathrm{h}_{\mathrm{Cj}}$). Apart from releasing the second output (here, $\mathrm{Ck}$), CatHelper strands also displace the Flux strand by toehold exchange, which is then free to interact with another Produce complex to release more outputs, thereby effectively "tuning up" the output stoichiometry of the desired CRN. Note that both the Helper and CatHelper strands are tagged with a fluorophore (here, ROX) at the 5' end. Since the Produce complex is tagged with a quencher at the 3' end of the bottom strand, the consumption of the Helper and CatHelper strands can be quantitatively measured through fluorimetry (Section S5.1).

### S3.5 Comparing the kinetics of the autocatalytic modules

#### S3.5.1 Kinetic measurements for individual strand displacement and toehold exchange reactions

Rate constants for the following reactions comprising the DNA implementation of the autocatalytic module $\mathrm{B} + \mathrm{A} \rightarrow 2\,\mathrm{B}$ were measured independently. For the input signals in these experiments, we

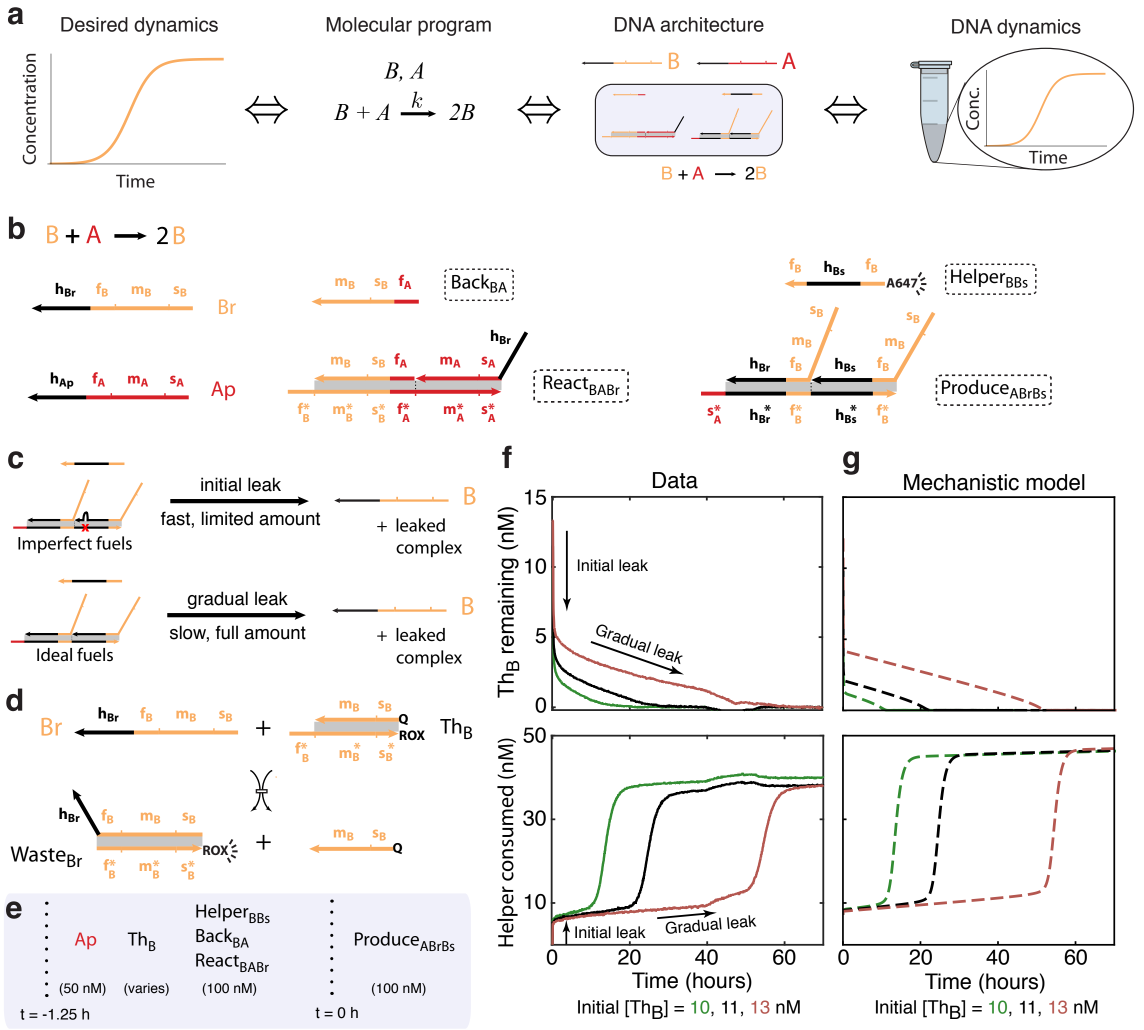

Figure S15: **Characterization of autocatalytic module $\mathbf{B} + \mathbf{A} \rightarrow \mathbf{2\,B}$.** (**a**) Schematic for engineering a single-reaction CRN with exponential amplification using our systematic pipeline. (**b**) Domain-level illustration of the DNA species involved (fuel species indicated by dashed boxes). (**c**) A limited amount of imperfect fuel species, such as those with DNA synthesis errors, release signal strands and waste products through fast spurious pathways ("initial leak"). Ideal fuel species release similar products through slow "gradual" leak. (**d**) A Threshold complex ($\mathrm{Th_B}$) is designed to consume leaked autocatalyst. (**e**) Experimental setup. Vertical dotted lines separate initial contents of the test tube and timed additions. Addition of Produce complexes kickstarts release of autocatalyst through initial and gradual leak. (**f**) Experimental data showing concentration of $\mathrm{Th_B}$ (top) and the amount of $\mathrm{Helper_{BBs}}$ consumed (bottom) for three independent samples with differing initial amounts of $\mathrm{Th_B}$. (**g**) The essential features of the autocatalytic dynamics were captured by a quantitative mechanistic model at the level of individual strand displacement reactions (see S6). Besides independently measured parameters and empirical parameters that were fit to the full oscillator data, only the initial threshold amounts were fit to the autocatalytic data shown here. These additional parameters capture the uncertainty in pipetting and initial leak, and effectively control the "triggering" time of autocatalysis. Note that to minimize the number of fit parameters, a global substoichiometric yield parameter was used, which could not fully account for the final "Helper consumed" amount in each autocatalytic module.

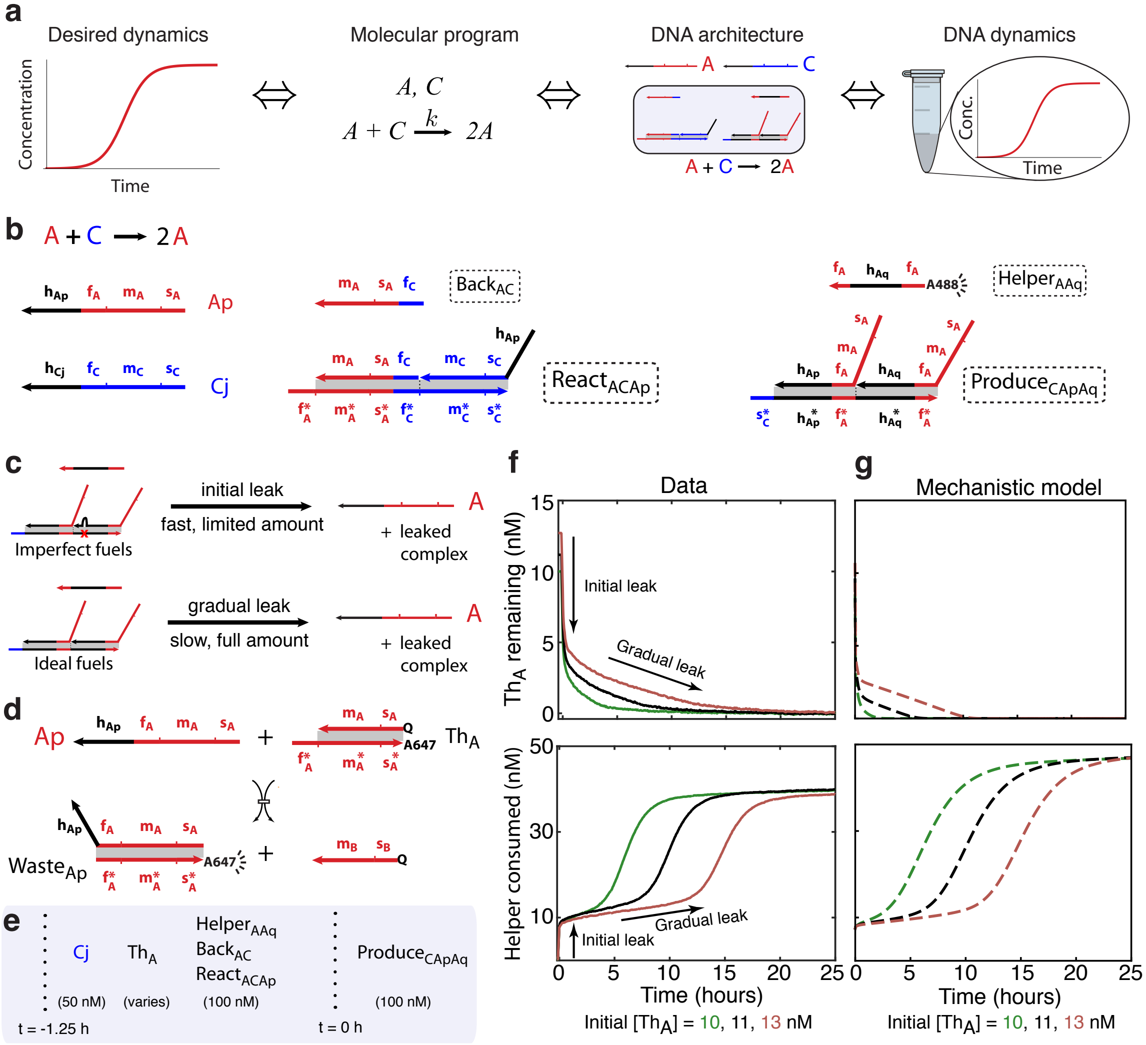

Figure S16: **Characterization of autocatalytic module A + C → 2 A.** (**a**) Schematic for engineering a single-reaction CRN with exponential amplification using our systematic pipeline. (**b**) Domain-level illustration of the DNA species involved (fuel species indicated by dashed boxes). (**c**) A limited amount of imperfect fuel species, such as those with DNA synthesis errors, release signal strands and waste products through fast spurious pathways ("initial leak"). Ideal fuel species release similar products through slow "gradual" leak. (**d**) A Threshold complex ($\mathrm{Th_A}$) is designed to consume leaked autocatalyst. (**e**) Experimental setup. Vertical dotted lines separate initial contents of the test tube and timed additions. Addition of Produce complexes kickstarts release of autocatalyst through initial and gradual leak. (**f**) Experimental data showing concentration of $\mathrm{Th_A}$ (top) and the amount of $\mathrm{Helper_{AAq}}$ consumed (bottom) for three independent samples with differing initial amounts of $\mathrm{Th_A}$. (**g**) The essential features of the autocatalytic dynamics were captured by a quantitative mechanistic model at the level of individual strand displacement reactions (see S6). Besides independently measured parameters and empirical parameters that were fit to the full oscillator data, only the initial threshold amounts were fit to the autocatalytic data shown here. These additional parameters capture the uncertainty in pipetting and initial leak, and effectively control the "triggering" time of autocatalysis. Note that to minimize the number of fit parameters, a global substoichiometric yield parameter was used, which could not fully account for the final "Helper consumed" amount in each autocatalytic module.

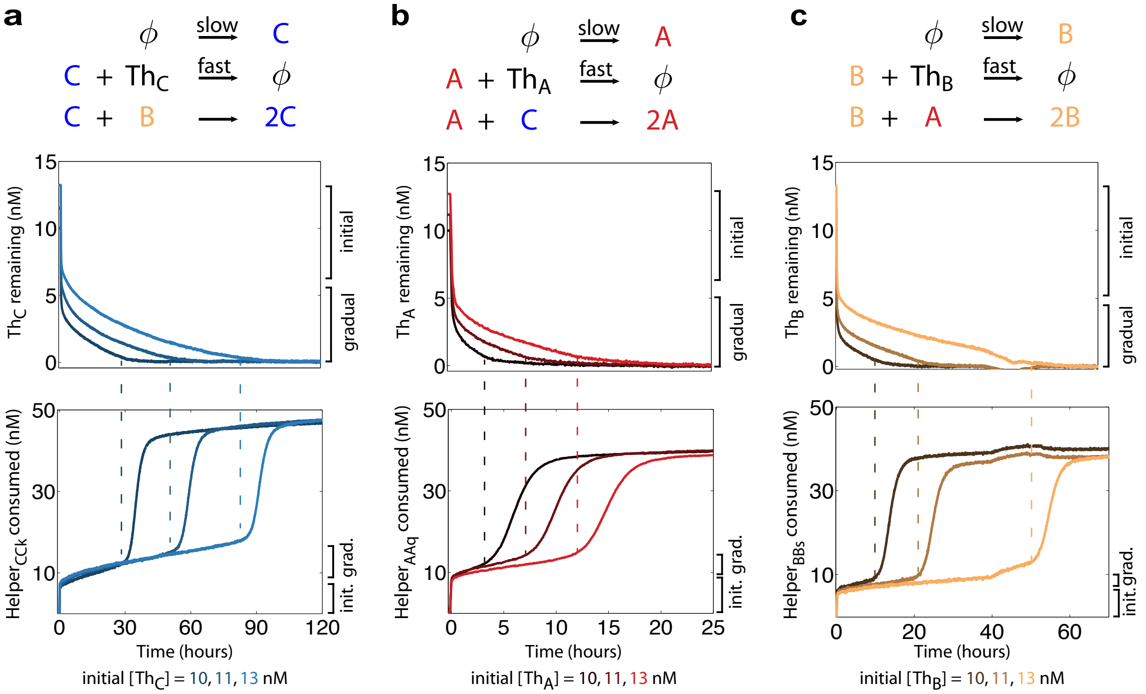

Figure S17: **Comparison of exponential kinetics in all three autocatalytic modules, with delays tuned by Threshold concentrations.** (**a**) The $C + B \rightarrow 2\,C$ module. (**b**) The $A + C \rightarrow 2\,A$ module. (**c**) The $B + A \rightarrow 2\,B$ module. Note that the time-axes are different for the three modules. Fig. S18 illustrates our method for estimating leak rates for each module; Table S4 summarizes these estimates. The data illustrates the substoichiometric yield effect (Fig. S12): in panel (b), for example, the total consumption of $\mathrm{Helper_{AAq}}$, including that consumed by initial leak, is approximately 40 nM. This total value is 20% less than what we would expect, given that the total initial concentration of C was approximately 50 nM. The substoichiometric yield effect is probably even larger, since some of the initial consumption of $\mathrm{Helper_{AAq}}$ would arise from initial leak with $\mathrm{Produce_{CApAq}}$, which is independent of C (e.g. Fig. S10b). Substoichiometric yield is also observed in experiments with individual fuel complexes (e.g. Fig. S26).

| Complex | $k_{\mathrm{fwd1}}$ | $k_{\mathrm{back}}$ | $k_{\mathrm{fwd2}}$ | Diagrams |
|---|---|---|---|---|
| $\mathrm{React_{ACApi2}}$ | $2.7 \times 10^5$ | $1.1 \times 10^6$ | $1.4 \times 10^5$ | Figs. S59, S62, S65 |
| $\mathrm{React_{BABr}}$ | $1.8 \times 10^5$ | $6.2 \times 10^5$ | $2.7 \times 10^5$ | Figs. S60, S63, S66 |
| $\mathrm{React_{CBCj}}$ | $8.6 \times 10^4$ | $9.8 \times 10^5$ | $3.0 \times 10^5$ | Figs. S61, S64, S67 |
| $\mathrm{Produce_{CApAq}}$ | $2.1 \times 10^5$ | $2.2 \times 10^5$ | $1.2 \times 10^6$ | Figs. S68, S71, S74 |
| $\mathrm{Produce_{ABrBs}}$ | $6.0 \times 10^5$ | $4.6 \times 10^5$ | $1.5 \times 10^6$ | Figs. S69, S72, S75 |
| $\mathrm{Produce_{BCjCk}}$ | $1.6 \times 10^6$ | $2.4 \times 10^5$ | $2.6 \times 10^6$ | Figs. S70, S73, S76 |

Table S2: **Independently measured rate constants for reactions within the react steps and produce steps in the Displacillator (Design 4).** All rate constants are given in /M /s, for experiments performed at 25 °C in TE buffer, pH 8.0, with 0.5 M $\mathrm{Na^+}$. Notation for rate constants of the designed strand displacement and toehold exchange reactions is specified by example in Equations 5 - 8. Note that rate constants involving the catalytic Helper pathway have not been characterized. Section S1.2 discusses the experimental methods and modeling used for estimating these rate constants.

| Threshold | Measured rate constant ( /M /s) | Diagram |
|---|---|---|
| $k_{\mathrm{ThA}}$ | $7.4 \times 10^5$ | Fig. S50 |
| $k_{\mathrm{ThB}}$ | $1.7 \times 10^6$ | Fig. S51 |
| $k_{\mathrm{ThC}}$ | $1.2 \times 10^6$ | Fig. S52 |

Table S3: **Independently measured rate constants for threshold reactions (Design 4).** These reactions involve the consumption of signal strands ($\mathrm{Ap}$, Br, and Cj) by thresholds ($\mathrm{Th_A}$, $\mathrm{Th_B}$, and $\mathrm{Th_C}$, respectively). All rate constants are given in /M /s, for experiments performed at 25 °C in TE buffer, pH 8.0, with 0.5 M $\mathrm{Na}^+$. Equation 9 specifies the reaction and the notation used for the rate constant. Section S1.2 discusses the experimental methods and modeling used for estimating these rate constants.

used history variants $\mathrm{Ap}$ and $\mathrm{Br}$ only; we assume that rate constants for $\mathrm{Aq}$ and $\mathrm{Bs}$ would be very similar. The same type of measurements were made for the other autocatalytic modules. All these measured rate constants are specified in Table S2. Figs. S7- S9 provide diagrams that illustrate these reactions.

$$\mathrm{Br} + \mathrm{React}_{\mathrm{BABr}} \underset{k_{\mathrm{back}}^{\mathrm{BABr}}}{\overset{k_{\mathrm{fwd1}}^{\mathrm{BABr}}}{\rightleftharpoons}} \mathrm{ReactInt}_{\mathrm{BrABr}} + \mathrm{Back}_{\mathrm{BA}} \tag{5}$$

$$\mathrm{ReactInt}_{\mathrm{BrABr}} + \mathrm{Ap} \xrightarrow{k_{\mathrm{fwd2}}^{\mathrm{BABr}}} \mathrm{Flux}_{\mathrm{ABr}} + \mathrm{Waste}_{\mathrm{BrAp}} \tag{6}$$

$$\mathrm{Flux}_{\mathrm{ABr}} + \mathrm{Produce}_{\mathrm{ABrBs}} \underset{k_{\mathrm{back}}^{\mathrm{ABrBs}}}{\overset{k_{\mathrm{fwd1}}^{\mathrm{ABrBs}}}{\rightleftharpoons}} \mathrm{Br} + \mathrm{ProduceInt}_{\mathrm{ABrBs}} \tag{7}$$

$$\mathrm{ProduceInt}_{\mathrm{ABrBs}} + \mathrm{Helper}_{\mathrm{BBs}} \xrightarrow{k_{\mathrm{fwd2}}^{\mathrm{ABrBs}}} \mathrm{Bs} + \mathrm{Waste}_{\mathrm{ABrBs}} \tag{8}$$

In addition, the kinetics of the consumption of $\mathrm{Br}$ by the threshold $\mathrm{Th_B}$ was also measured. Note that the analogous reaction for the consumption of $\mathrm{Bj}$ was not characterized; it was assumed that the rate constant for that reaction would be similar. The kinetics of consumption of $\mathrm{Cj}$ and $\mathrm{Ap}$ were also characterized. All these rate constants are listed in Table S3. Fig. 2D of the main text and Fig. S15 and Fig. S16 provide diagrams that illustrate these reactions.

$$\mathrm{Br} + \mathrm{Th_B} \xrightarrow{\mathrm{k_{ThB}}} \mathrm{Waste_{Br}} \tag{9}$$

## S3.6 Estimating leak rates for the three autocatalytic modules

Each designed strand displacement reaction pathway in a reaction network contributes unintended, or leak, reaction pathways (see Section S4.1). Some leak pathways are active before all reaction components are mixed together in solution and alter the initial species concentrations. Therefore, we must estimate the extent that leak impacts initial conditions for each reaction pathway, separately, and account for these errors when selecting initial species concentrations for experiments involving the full rock-paper-scissors reaction network. In this section, we describe our method of measuring leak parameters from autocatalyst reactions of the type shown in Fig. S17.

These experiments show the relationship between initial Threshold concentration and the time delay before entering the exponential growth phase of the reaction. To estimate the initial leak from these data, we assume the following:

1. Two sources of leak
   (a) Initial leak, which instantly consumes an Helper and releases output strand.
   (b) Gradual leak, which is a constant rate of Helper consumption and output strand release.
2. Thresholding is faster than the autocatalytic reaction. That is, gradual leak interacts only with Threshold complexes until they are all spent.
3. When there are no longer active Threshold complexes, the system enters the autocatalytic phase and rapidly accelerates Helper consumption.

Assumptions 1 and 2 imply a linear relationship between initial Threshold concentration and delay, the time to trigger all of the Threshold complexes and initiate the autocatalytic phase of the reaction. Assumption 3 suggests that $t_c$, the moment all Threshold complexes have been triggered, can be defined as the moment the Helper consumption rate surpassses a threshold rate. For gradual leak $\alpha$, initial leak $\beta$, and threshold-crossing time $t_c$

$$[\text{Threshold}](t) = [\text{Threshold}]_0 - \alpha t - \beta$$

$$[\text{Threshold}](t_c) = 0$$

$$[\text{Threshold}]_0 = \alpha t_c + \beta$$

We find parameters $\alpha$ and $\beta$ by determining the threshold-crossing times $t_c$ for each experimental sample and performing linear regression on the data points $(t_c, [\text{Threshold}]_0)$. These leak parameters were used in the mechanistic model described in Section S6. This estimation procedure assumes that actual Threshold concentration is close to the desired Threshold concentration, i.e. that pipetting errors are low. The clear linear relationship between initial Threshold concentration and observed time delay (Fig. S18; bottom row) suggests that this assumption holds.

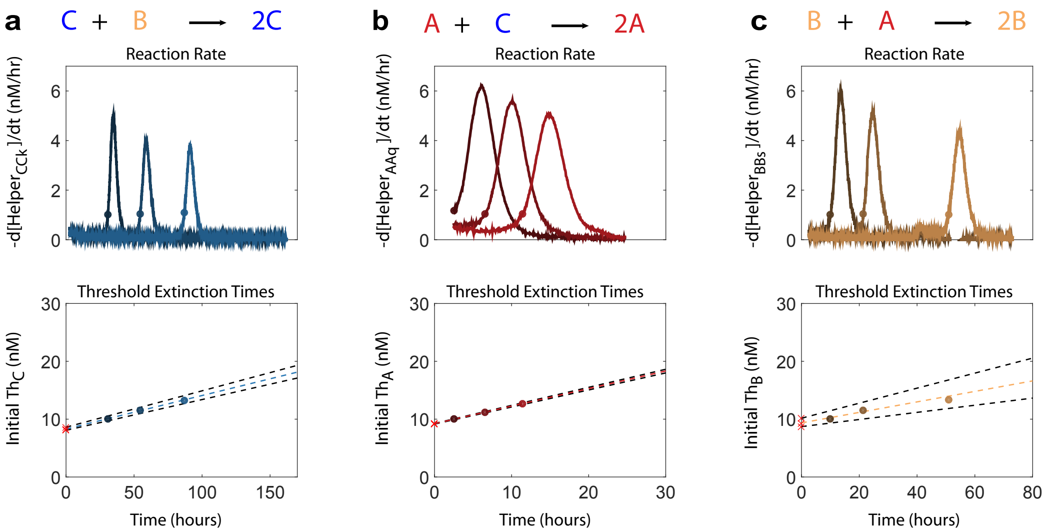

Figure S18: **Leak estimation from Design 4 autocatalyst reactions.** (**a**) The $\mathrm{C} + \mathrm{B} \rightarrow 2\,\mathrm{C}$ module. (**b**) The $\mathrm{A} + \mathrm{C} \rightarrow 2\,\mathrm{A}$ module. (**c**) The $\mathrm{B} + \mathrm{A} \rightarrow 2\,\mathrm{B}$ module. The initial and gradual leak parameters are estimated by fitting a line to the initial Threshold concentration and the time delay before the exponential phase. We define the time delay to be the first time-point at which the rate of Helper consumption is larger than 1 nM/hr, an arbitrary threshold close to the onset of exponential phase. This is represented in the first row of plots. The second row shows the threshold-crossing time-points matched with their respective initial Threshold concentrations. The dashed, colored lines are linear regression fits for each reaction pathway. The red x-marks on the Initial Threshold axes indicate the fitted initial leak parameter. To get a sense for the range of reasonable leak parameters, we performed the linear fit on all distinct pairs of data-points for each reaction, generating three estimates for each parameter. We then took the maximum and minimum value for each parameter, regardless of which data-points they are associated with, as the maximum and minimum leak parameter sets implied by the data. These extrema sets are plotted as black dashed lines with red x-marks in the second row of plots.

| Module | Initial leak (nM) | Gradual leak velocity (nM/hr) | Gradual leak rate constant (/M/s) |
|---|---|---|---|
| $\mathrm{B} + \mathrm{A} \rightarrow 2\,\mathrm{B}$ | 9.35 | 0.091 | 3.13 |
| $\mathrm{C} + \mathrm{B} \rightarrow 2\,\mathrm{C}$ | 8.31 | 0.058 | 1.99 |
| $\mathrm{A} + \mathrm{C} \rightarrow 2\,\mathrm{A}$ | 9.36 | 0.295 | 10.07 |

Table S4: **Leak parameters derived from autocatalyst experiments using Design 4.**

# S4 Discovery of the design principles through multiple iterations of the design pipeline

This section summarizes our process of discovery through multiple rounds of design. Section S4.1 provides a brief overview of the major sequence design considerations and challenges; Section S4.2 discusses Design 1; Section S4.3 presents the *in silico* heuristics and design process we formulated for evaluating later designs; Section S4.5 and Section S4.6 discuss Design 3 and Design 4 respectively. **All data in this work is from Design 4, unless explicitly stated otherwise in the text or in a figure caption.**

## S4.1 Sequence design challenges

As described in the main text, an experimental implementation is judged based on how faithfully it captures the dynamics specified by the domain-level model. Sequence design is the process of finding DNA sequences such that the resulting molecular system stays as faithful to the domain-level abstraction as possible. The following major issues were considered during the design process:

- **Achieving desired rates for intended pathways.** In general, the problem of designing sequences for strand displacement reactions under kinetic constraints, in order to achieve a prescribed rate constant, is challenging - well-characterized rules and design tools do not exist (36, 45, 63). Therefore we attempt to control kinetics through thermodynamic proxies, such as toehold strength. At 25° C, rate constants increase exponentially with the toehold binding strength up to about 8 to 9 kcal/mol, whereupon the rate constant saturates (see Fig. 3 of Zhang & Winfree (35)). We chose our six toeholds, $\mathrm{f_A}$, $\mathrm{f_B}$, $\mathrm{f_C}$, $\mathrm{s_A}$, $\mathrm{s_B}$, and $\mathrm{s_C}$, to be roughly equally strong. For three reasons, we chose toehold energies such that strand displacement rates with those toeholds would be just within the saturation regime, i.e., between 8 and 9 kcal/mol. First, such strong toeholds result in fast strand displacement rates relative to gradual leak rates. Second, small variations in toehold energy would not be expected to result in large variation in (relative) strand displacement rates in the saturation regime. Third, stronger binding would prevent fast dissociation and lead to more toehold occlusion, as discussed below.

- **Balancing toehold strengths in different contexts**. Each toehold occurs in multiple local contexts: e.g. the internal and external contexts illustrated in Fig. S26. In particular, toehold exchange reactions in the react step involve the "forward" toehold in an external context and the "backward" toehold in an internal context. The relative rates of the forward and reverse toehold exchange steps depends crucially on the relative binding energies of the two toeholds (see Fig. 4 of Zhang & Winfree (35)). In particular, if the stronger toehold initiates displacement with roughly the same rate constant as "irreversible" strand displacement (i.e. it is in the saturation regime), then the rate constant for the reverse direction mediated by the weaker toehold will be slower than the forward direction by a factor of $e^{|\Delta\Delta G^\circ|/RT}$, where $|\Delta\Delta G^\circ|$ is the absolute difference in toehold energies. In balancing toehold strengths, we concluded that it is important to consider the energetic contributions of co-axial stacking at nicks (84), dangling single-stranded nucleotides at helix ends (27), and single-stranded tails protruding at nicks (36), in addition to the standard nearest-neighbor base-pair stacking energies (85).

- **Achieving fast unimolecular dissociation rates.** Strong toeholds are not without drawbacks. Toeholds need to be weak enough to ensure that toehold dissociation rates are fast (else, unimolecular dissociation steps would become rate-limiting). Moreover, fast dissociation rates would ensure that complexes that are not designed to interact with each other but that have complementary toehold regions will not be co-localized significantly, an effect we call toehold occlusion (see Fig. S13).
- **Avoiding unintended secondary structure.** Several species (the signal strands, Flux, Back, and Helper strands) need to be almost completely single-stranded, with no intra-molecular base pairing, most of the time. Secondary structure in key locations, such as toeholds or the first few base pairs involved in branch migration, is known to slowdown strand displacement rates (36, 86, 87).
- **Minimizing initial and gradual leaks.** As discussed below, several design rules and heuristics aim to minimize the magnitude of initial and gradual leaks. These strategies are summarized at a high level in Fig. 3 of the main text and in detail in Section S4.3– S4.6.

For reasons discussed below, Designs 1 and 2 have opposite $5'$-$3'$ orientation for all the strands and multi-stranded complexes relative to Designs 3–5 and all the domain-level diagrams.

## S4.2 Sequence design 1

### S4.2.1 Design criteria

Design 1-PRE (preliminary) employed the following criteria:

- All "top" strands (signal strands, Flux, Back, and Helper strands) were designed to use the 'ACT' alphabet (no 'G's). This is standard practice in dynamic DNA nanotechnology (35, 39, 86) for avoiding unintended intramolecular secondary structure.
- Toeholds were designed to be of the form 'WWWSSSW' where W stands for a "weak" base (A or T) and S stands for a "strong base" (C or G). By ensuring that each toehold has exactly 3 strong base-pairs, we attempted to achieve similar toehold binding strengths. When combined with the choice of 'ACT' alphabet for top strands, this rule forces all toeholds in the top strands to be 'WWWCCCW' and all toeholds in the complementary "bottom" strands to be 'WWWGGGW'.
- To minimize the initiation of spurious branch migration, we designed domains intended for branch migration ($\mathrm{m_A}, \mathrm{m_B}, \mathrm{m_C}$, and history domains) to be as different as possible at each end. Further, the first and last base of every branch migration domain was constrained to be a strong base, in order to reduce fraying of the helices at the ends. Sequences in the middle of branch migration regions were essentially randomly generated.
- Lastly, Design 1-PRE was verified by eye with the NUPACK web interface (28) to ensure that the desired multi-stranded complexes and intermediates were well-formed and that the top strands were (mostly) free of secondary structure.

### S4.2.2 Design 1: Results

We encountered very high initial leaks (8 - 15% of the fuel concentration) with Design 1-PRE. Despite our best efforts at purification of fuel complexes, which included the use of PAGE-purified strands, ultramers, modified annealing and gel-purification protocols, we could not reduce this initial leak to much less than 10%. Further, the amount of initial leak scaled monotonically with the concentration of the fuel complex (experiments not shown). This observation suggested that the initial leak arises due to a fraction of mis-folded fuel complexes.

We also observed very high gradual leaks (20-40 /M/s). We hypothesized that gradual leaks were due to blunt-end strand displacement initiated by invasion at the ends of helices (Fig. S10C) due to fraying (36). To minimize such spurious pathways, we added 2-nucleotide clamps to the React and Produce complexes (Fig. S19). We call this design, augmented with 2-nucleotide clamps, Design 1.

Although Design 1 had lower gradual leak, the reduction was not substantial (Fig. S20). No reduction in initial leak was observed. **The 2-nt clamps present in Design 1 are also included in all subsequent sequence designs, even if they may sometimes be omitted, for convenience, in domain level diagrams**. Sequences that comprise Design 1 are provided in Section S9.

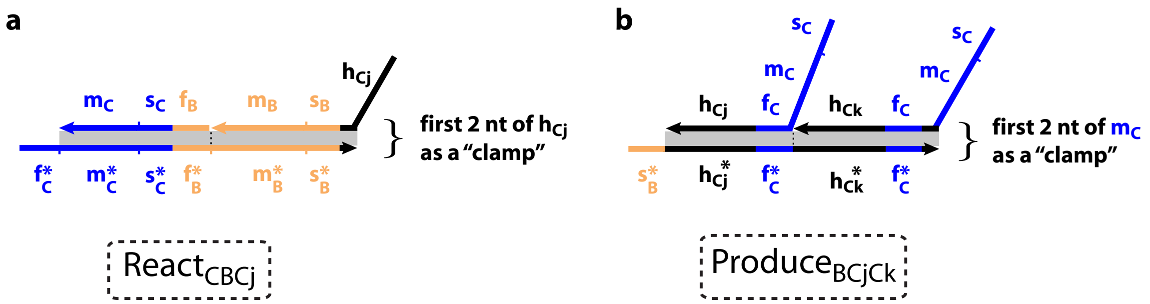

Figure S19: **Clamps to reduce leak.** After preliminary experiments with Design 1-PRE demonstrated very high gradual leak rates, we added 2-nucleotide "clamps" to all React (**a**) and Produce (**b**) complexes as illustrated here, to obtain Design 1. These clamps are meant to mitigate some of the gradual leak pathways shown in Fig. S10, such as the React-Produce gradual leaks in panel (c) of that figure. The clamps did reduce gradual leak, but not substantially. **They are included in Design 1 and all subsequent designs, even if they may sometimes be omitted, for convenience, in domain level diagrams.**

### S4.2.3 Estimating gradual leak rates

Even with the 2-nucleotide clamps, we observed Produce-Helper gradual leak rates as high as 150 /M /s and React-second input gradual leak rates as high as 50 /M /s in Design 1 (Fig. S20). We now describe the procedure used for obtaining numerical estimates of gradual leak rate constants with the $\mathrm{Produce}_{\mathrm{CApAq}}$-$\mathrm{Helper}_{\mathrm{AAq}}$ leak (Sample 3 in Fig. S20) as an example.

First, the total amount "leaked" (say $l$, in M) was measured within an (arbitrary) time window within which the slope of the curve can be approximated to be constant. For Sample 3 in Fig. S20, this could be between 5 and 7 hours. Then, we divide $l$ by the length of the time window (in s) to obtain the instantaneous flux $f$ (in M/s). Assuming that the concentrations of the species involved ($\mathrm{Produce}_{\mathrm{CApAq}}$ and $\mathrm{Helper}_{\mathrm{AAq}}$) would not change significantly within the time window,

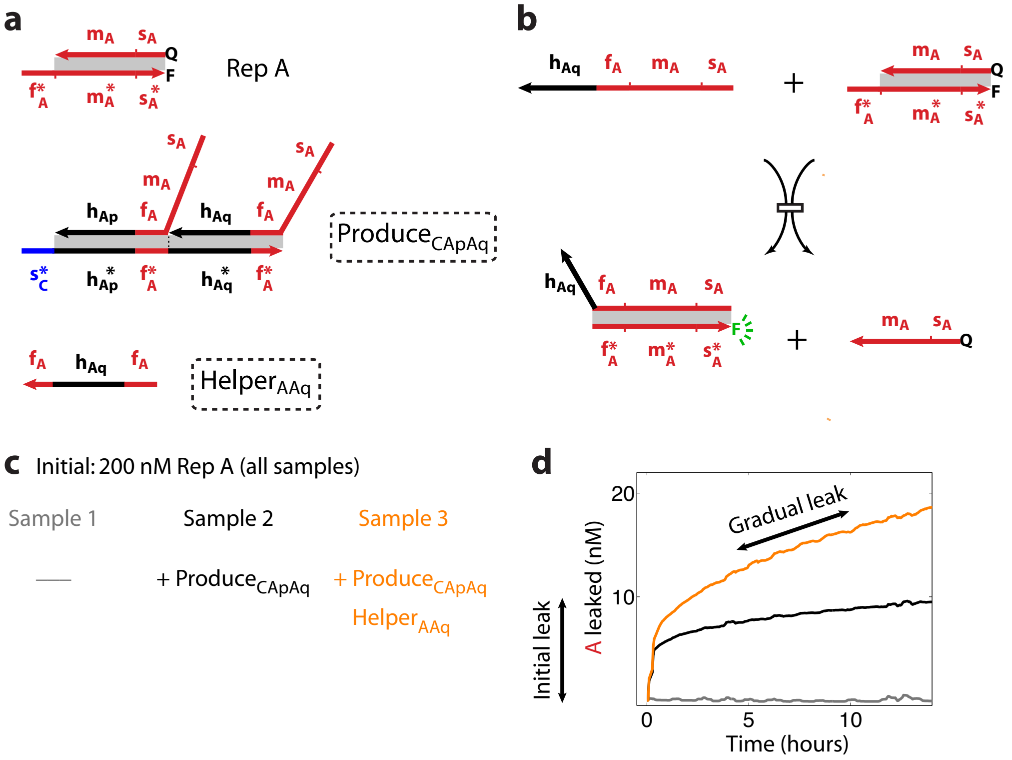

Figure S20: **Example leaks in Design 1.** Shown are measurements of $\mathrm{Produce_{CApAq}}$-$\mathrm{Helper_{AAq}}$ leaks. (**a**) The molecules involved. RepA, short for “Reporter for A”, is an alternate name for $\mathrm{Th_A}$. Here the primary purpose is just fluorescence readout of the concentration of A, using the regular Threshold mechanism shown in panel b. (**b**) Aq displaces the strand with the quencher (Q), leading to a waste product where the Fluorophore (F) can emit light at its characteristic wavelength. This mechanism works for Ap as well, yielding a quantitative readout of A. c. Experimental setup. All three samples are essentially negative controls for the function of $\mathrm{Produce_{CApAq}}$, since no $\mathrm{Flux_{CAp}}$ is present. Sample 1 shows stable baseline fluorescence of RepA. In Samples 2 and 3, the addition of 100 nM of $\mathrm{Produce_{CApAq}}$ causes initial leak of A. The initial leak is higher in Sample 3 because 50 nM of $\mathrm{Helper_{AAq}}$ was also added, which suggests that $\mathrm{Helper_{AAq}}$ facilitates this leak. After the initial leak, the slow but persistent gradual leak of A in Sample 3 is the $\mathrm{Produce_{CApAq}}$-$\mathrm{Helper_{AAq}}$ leak. A much smaller $\mathrm{Produce_{CApAq}}$-RepA gradual leak is observed in Sample 2.

and assuming a bimolecular rate law for the gradual leak, we then estimate the leak rate constant $k_{\mathrm{leak}}$ (in /M /s) by dividing $f$ by the estimated concentrations of the species involved at the beginning of the time window (5 hours). We found that this rough estimate did not usually vary more than by a factor of 2-3 for reasonable choices of the time window.

### S4.3 Heuristics for evaluating sequence designs *in silico*

Our experience with Design 1 suggested that we did not really know what we should design for (or against). To understand that better, we developed some heuristic measures which attempted to quantitatively capture various undesired spurious interactions. Using these heuristic measures, we hoped to quantify the “goodness” of candidate designs and sequence design algorithms (by comparing the best designs we could obtain from each algorithm). We now introduce the heuristic measures.

First, we define a "NUPACK interaction score", I (S1, S2), between single-stranded species S1 and S2. I (S1, S2) is the percentage of strands that are in any dimer (S1:S1, S1:S2, or S2:S2), as predicted by NUPACK when S1 and S2 are each at a concentration of 1 µM. For this calculation (i) the temperature is set to be 25°C and (ii) the salt concentration to be 50 mM Na$^{+}$ and 12.5 mM Mg$^{++}$, and (iii) complexes comprising at most 2 strands are considered. Therefore, with some algebra,

$$\mathrm{I}\left(\mathrm{S1}, \mathrm{S2}\right) = 100 * \left(\frac{[\mathrm{S1}:\mathrm{S1}] + [\mathrm{S1}:\mathrm{S2}] + [\mathrm{S2}:\mathrm{S2}]}{\mathrm{c}}\right), \tag{10}$$

where c = 1 µM.

The "Top Strand Interactions (TSI)" score is the sum of interaction scores for every distinct pair of top strands (signal strands, Flux, Back, and Helper strands). That is, if $\{S_i\}$ are the top strands,

$$\mathrm{TSI} := \sum_{\substack{(i,j)\\ i \leq j}} \mathrm{I}\left(\mathrm{S_i}, \mathrm{S_j}\right). \tag{11}$$

The "Toehold Occlusion (TO)" score is the sum of I ($t^*$, S) for every toehold-complement $t^*$ and top strand S, assuming S does not contain toehold $t$. If S does contain toehold $t$, I ($t^*$, S) is replaced by I ($t^*$, $S_{<t}$) + I ($t^*$, $S_{>t}$) where $S_{<t}$ is the subsequence of S, starting at the 5' end, before encountering domain $t$ and $S_{>t}$ is the subsequence after domain $t$. Strictly, the above definition of $S_{>t}$ could contain an occurrence of $t$ if $t$ occurs multiple times in the original strand $S$; if that is the case, iteratively apply the same rule. That is,

$$\mathrm{TO} := \sum_{\substack{(t,S)\\ t\,\in\,\text{Toeholds}\\ S\,\in\,\text{Top Strands}}} \mathrm{F}\left(\mathrm{t}, \mathrm{S}\right), \tag{12}$$

where

$$F(t,S) := \begin{cases} I\left(t^*, S\right) & \text{, if S does not contain } t \\ F(t^*, S_{<t}) + F(t^*, S_{>t}), & \text{if S contains } t. \end{cases}$$

The "Weighted Sum - Branch Migration (WS-BM)" score identifies the largest subsequence matches (not necessarily aligned by position) between distinct branch migration domains, which include the $\mathrm{m_A}, \mathrm{m_B}, \mathrm{m_C}$ and history domains. WS-BM is essentially a weighted sum of such subsequence matches. (Note that there are no intended matches between branch migration domains.) A subsequence match of length 5 contributes 1 point, length 6 contributes 2 points, length 7 contributes 4 points, and so on until lengths greater than or equal to 10 contribute 32 points.

If $\{R_i\}$ is the set of branch migration domains,

$$\text{WS-BM} := \sum_{\substack{(R_i,R_j)\\ i\,<\,j}} \left(\max_{(s,s')\,\in\Phi(R_i)\times\Phi(R_j)} W_{exp}(s,s')\right), \tag{13}$$

where $\Phi(R_i)$ is the multiset of all subsequences of the sequence $R_i$ and $W_{exp}$ is the weight function defined by

$$W_{exp}(s, s') := \begin{cases} 0 & \text{if } |s| < 5 \text{ or } s \neq s' \\ 2^{|s|-5} & \text{if } |s| \in [5, 10] \text{ and } s = s' \\ 32 & \text{if } |s| > 10 \text{ and } s = s'. \end{cases}$$

Note that the sum only accumulates the weight of the largest matching subsequence for any given pair of domains.

The "Maximum Branch Migration subsequence (Max-BM)" score seeks to quantify the same kind of non-ideality in the design but measures the length of the longest subsequence match between distinct branch migration domains, rather than a weighted sum over all pairs of branch migration domains. That is,

$$\text{Max-BM} := \max_{\substack{(R_i, R_j) \\ i < j}} \left( \max_{s \in \Phi(R_i) \cap \Phi(R_j)} |s| \right). \tag{14}$$

The "Weighted Sum Inter-Strand (WSIS)" evaluates unintended subsequence matches between all pairs of strands in a DNA reaction network, weighted by the matching subsequence's length. This calculation finds subsequences of a strand that are exact matches to (or exact complements of) a subsequence another strand. Only spurious matches, as opposed to those guaranteed by the design specification, contribute to the WSIS. A subsequence match (based on identity or complementarity) of length 6 contributes 1 point, length 7 contributes 2 points, and so on up to matches of length 12 and above, which contribute 7 points.

$\{S_i\}$ is a set from which pairs of strands are drawn during WSIS calculation. For reasons not discussed here that relate to the operating details of our sequence design software, this set contains one copy of each fuel strand and two copies of each signal strand. As a result, all spurious matches involving one signal strand are counted twice and matches involving two different signal strands are counted four times. The software is aware of which members in the set are identical copies of a signal strand and so does not consider matches in these comparisons to be spurious.

$$\begin{aligned} \{S_i\} = \{&\mathrm{Ap}, \mathrm{Ap}, \mathrm{Aq}, \mathrm{Aq}, \mathrm{Br}, \mathrm{Br}, \mathrm{Bs}, \mathrm{Bs}, \mathrm{Cj}, \mathrm{Cj}, \mathrm{Ck}, \mathrm{Ck}, \\ &\mathrm{Back}_{\mathrm{BA}}, \mathrm{Back}_{\mathrm{CB}}, \mathrm{Back}_{\mathrm{AC}}, \mathrm{Flux}_{\mathrm{ABr}}, \mathrm{Flux}_{\mathrm{BCj}}, \mathrm{Flux}_{\mathrm{CAp}}, \\ &\mathrm{Helper}_{\mathrm{BBs}}, \mathrm{Helper}_{\mathrm{CCk}}, \mathrm{Helper}_{\mathrm{AAq}}, \\ &\mathrm{ReactBot}_{\mathrm{BABr}}, \mathrm{ReactBot}_{\mathrm{CBCj}}, \mathrm{ReactBot}_{\mathrm{ACAp}}, \\ &\mathrm{ProduceBot}_{\mathrm{ABrBs}}, \mathrm{ProduceBot}_{\mathrm{BCjCk}}, \mathrm{ProduceBot}_{\mathrm{CApAq}}\} \end{aligned} \tag{15}$$

$$\text{WSIS} := \sum_{\substack{(S_i, S_j) \\ i < j}} \left( \sum_{(s, s') \in \Phi(S_i) \times \Phi(S_j)} W_{lin}(s, s') \right),$$

where $\Phi(S_i)$ is the multiset of all subsequences of strand $S_i$ and $W_{lin}$ is the weight function defined by

$$W_{lin}(s, s') := \begin{cases} 0 & \text{if } |s| < 6 \text{ or if } s \text{ does not match } s' \text{ or if } s \text{ is an intended match} \\ |s| - 5 & \text{if } |s| \in [6, 12] \text{ and } s \text{ matches } s' \text{ unintentionally} \\ 7 & \text{if } |s| > 12 \text{ and } s \text{ matches } s' \text{ unintentionally.} \end{cases}$$

In the implementation, matches of length up to 12 were considered.

As an example, suppose that the $3'$ end of domain $\mathrm{m_A}$ has 2 nucleotides unintentionally identical to the $3'$ end of domain $\mathrm{h_{Aq}}$. Then if strand $S_i$ is signal strand Ap and strand $S_j$ is the catalytic $\mathrm{Helper_{AAq}}$, there will be an exact identity match between the $3'$ half of signal strand Ap (domains $\mathrm{h_{Ap}}$, $\mathrm{f_A}$, and 2 nt of $\mathrm{m_A}$) and the corresponding part of the CatHelper strand (domains $\mathrm{h_{Ap}}$, $\mathrm{f_A}$, and 2 nt of $\mathrm{h_{Aq}}$). Accordingly, this would be identified as an unintentional match of length greater than 12 and scored as specified above (note however that our implementation considers spurious matches of length up to 12 only). The merit of scoring this "2 nucleotide" sequence design error as a "12 nucleotide unintentional match" is that sequence uniqueness near junctions can be especially important for self-assembly and structural integrity (29).

The "Weighted Sum Inter-Strand Mismatch (WSIS-M)" is identical to the WSIS score, except that it only counts subsequence matches (either based on identity or complementarity) that have a 1-base mismatch. To illustrate with a particular example, subsequences 'ATAACCA' and 'ATATCCA' would be considered a match.

Lastly, this design process involving custom heuristic scores was further updated before it was incorporated into the automated Piperine compiler for enzyme-free nucleic acid dynamical systems. These changes, which include inferences from debugging experiments performed with Designs 3 and 4, are outlined in Section S7.

### S4.3.1 Candidate sequence design methods

Since (i) toehold strengths are critical for controlling reaction kinetics and (ii) excessive spurious interaction between toeholds assumed to be orthogonal at the domain level is undesirable, we decided to design the toeholds first. Our objective was to obtain toeholds strong enough to elicit fast kinetics, with toehold strengths being as close as possible, yet as mutually orthogonal as possible. For this purpose we used StickyDesign (55), a software package used to design "sticky ends" for experimental DNA-tile based self-assembly. Without accounting for flanking bases (which do affect nearest neighbor contributions to the toehold strength), for Design 2 we targeted toehold strengths between 8.0 and 9.0 kcal/mol and toehold cross-talk binding energies of less than or equal to 2.5 kcal/mol. (Note that for Design 5, and the Piperine compiler, a more sophisticated energy model was used, which better accounts for flanking bases, toehold truncations, neighboring tails, etc., as described in Section S7).

We also enforced the following constraints in order to mitigate leak reactions. Since fraying due to thermal fluctuations at the ends of helices is thought to contribute to gradual leak pathways of the kind in Fig. S10, a per refs. (36, 86, 87), we constrained helices and junctions to end with two strong (C/G) base pairs. As a direct consequence of this decision, we had to choose between (i) allowing 1-2 base pairs to continually branch migrate back and forth on either side of the junction in the Produce complexes or (ii) violate the 'ACT' alphabet rule by incorporating Guanines (G) at specific places in top strands (see Fig. S21). Since option (i) could complicate toehold energy calculations, we chose to violate the ATC alphabet.

Once the toeholds were chosen, we tried multiple sequence design algorithms that were available at that time to design the rest of the system. Among these were SpuriousSSM (54), which minimizes unintended subsequence matches within and between complexes (a variant on "sequence symmetry minimization" (29)); DomainDesign (86), which focuses on designing domains of user-specified lengths to be as orthogonal as possible to each other based on thermodynamic calculations;

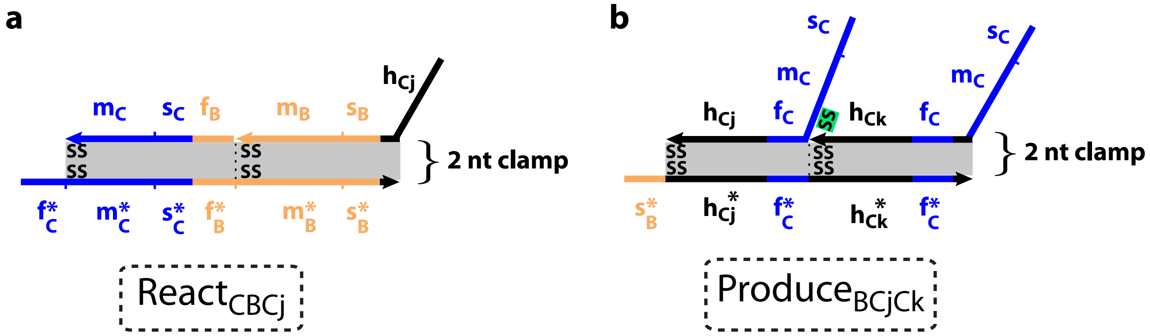

Figure S21: **Strategy to reduce gradual leak at nicks.** To reduce gradual leaks that are thought to be facilitated by thermal fraying of base pairs at junctions or ends of helices, in Design 2 we attempted to close such helices and junctions with two consecutive “strong” (S) base pairs. This strategy is illustrated with the React (**a**) and Produce (**b**) complexes. In this strategy, there is a trade off between the ACT alphabet and preventing branch migration at the junction in the Produce complexes. With the ACT alphabet, back and forth branch migration of 2 nucleotides around the junction is unavoidable since both $\mathrm{m_C}$ and $\mathrm{h_{Ck}}$ will need to begin with ‘CC’. To avoid this, we violated the ACT alphabet rule by fixing the first base of $\mathrm{m_C}$ (first of the two highlighted bases in this figure) to be a ‘G’. In some situations, e.g. $\mathrm{React_{ACAp}}$, the second highlighted base was also a ‘G’ (optimized by the designer to reduce spurious scores). **Warning:** As discussed in Section S4.5 and Figs. S23–S25, the strong base pairs at the 3′ end of the branch migration domain (green ‘SS’) resulted in a new leak pathway as well as intramolecular secondary structure that slowed down some desired reactions. To avoid these new problems, in Design 4 the two 3′-most nucleotides of the $\mathrm{m_?}$ domains were modified by hand to avoid use of ‘G’ and possibly include an ‘A’ or ‘T’, and the $\mathrm{h_?}$ domains were similarly modified to reduce secondary structure although some ‘G’ nucleotides were retained (see Section S4.6). Similarly, in Design 5, the 3′ end of all $\mathrm{m_?}$ domains is 3′-CT-5′, while the 3′ end of all $\mathrm{h_?}$ domains is 3′-AC-5′, which reduces leak while ensuring that the ACT alphabet rule is fully respected (see Section S7.

| Method | TSI | TO | WS-BM | Max-BM | WSIS | WSIS-M |
|---|---|---|---|---|---|---|
| Design 1 | 0.8 | **466.0** | 18 | 6 | **12469** | **8009** |
| SpuriousSSM (Design 2) | 7.2 | 21.6 | 10 | 6 | 30 | 2514 |
| DomainDesign | 12.2 | 19.6 | 7 | 6 | 1239 | 4016 |
| NUPACK | 1.6 | 56.2 | **73** | **10** | **13574** | **8674** |
| NUPACK-ND | 1.4 | 14.8 | **306** | **13** | **23529** | **27578** |
| NUPACK-ND-BM | 2.2 | 34.0 | 9 | **8** | **25872** | **8429** |

Table S5: **Heuristic scores of sequences considered for Design 2.** The best designs from various sequence design methods were evaluated using our custom heuristic measures. The heuristic measures and sequence design methods used are described in the text. Scores in bold were thought to be unacceptably high relative to other methods; this determination was based on a subjective intuition acquired by repeated design attempts.

and NUPACK (28) which minimizes ensemble-defect (31) to match the user-specified structure for each complex based on thermodynamic calculations.

The best designs we could obtain from each candidate algorithm were compared with each other and Design 1 on the basis of our custom heuristic measures. The results are summarized in Table S5. Note that there are three different designs based on NUPACK: "NUPACK" was run without any artificial negative-design constraints. "NUPACK-ND" included additional negative design constraints, intended for minimizing spurious interactions between single strands and toehold complements, in the form of artificial target "complexes" between species that were not supposed to interact: wherein the "desired" structure was specified to be without any base pairing between the two species. "NUPACK-ND-BM" included additional such constraints between branch migration domains. In addition, the following sequences were excluded by the use of NUPACK's "prevent" constraints: 'GGGG' (to avoid G-potential quartets) and 'WWWWWW' (6 contiguous weak A/T base-pairs).

Table S5 suggests that, given our toeholds, SpuriousSSM and DomainDesign gave the best designs according to our heuristic measures. Some caveats are in order while interpreting the results. First, our heuristic measures include measures that focus on spurious matches at the level of sequence identity, without a thermodynamic or kinetic evaluation of how physically important those spurious sequence identity matches might be in the test tube. Second, at the time this analysis was performed, NUPACK's second generation algorithms for "test tube design" (32), which perform negative design against competing complexes which could form in a user-specified test tube, had not been released. We have not tested the performance of the second generation NUPACK sequence design algorithms in this analysis. Further, we have no compelling evidence that, with respect to experimental performance, the heuristic design methods adopted here are preferable than the alternatives; we just know that they are good enough. Design 4 and Design 5 – designed using a refinement of the approach described here, as discussed in Sections S4.6 and S7 respectively – both resulted in functional DNA strand displacement oscillators. A future experimental study systematically comparing design methods for DNA strand displacement dynamical systems would be highly desirable.

| Species 1 | Species 2 | $k_{\text{leak}}$ (/M/s) |
|---|---|---|
| $\mathrm{Produce}_{\mathrm{CApAq}}$ | $\mathrm{Helper}_{\mathrm{AAq}}$ | 82 |
| $\mathrm{Produce}_{\mathrm{CApAq}}$ w/o G | $\mathrm{Helper}_{\mathrm{AAq}}$ | 11 |
| $\mathrm{Produce}_{\mathrm{CApAq}}$ w/o GG | $\mathrm{Helper}_{\mathrm{AAq}}$ | 3 |
| $\mathrm{Produce}_{\mathrm{CApAq}}$ | $\mathrm{Helper}_{\mathrm{AAq}}$ w/o CC | 28 |

Table S6: **Measured rate constants for leak at a nick, including remote-toehold effects (Design 3).** Bimolecular rate constants for the leak rates were estimated from the experiments described in Fig. S23.

## S4.4 Sequence design 2

Based on the analysis in Section S4.3.1, we decided to use SpuriousSSM for designing our second attempt. Experimentally, we found that Design 2 had much less gradual leak — as low as 1-10 /M /s. Gradual leaks of this magnitude are illustrated in Fig. S22 with an example from Design 3. However, Design 2 did not show any reduction in initial leak, which remained high (10% of the fuel concentration).

## S4.5 Sequence design 3

Typically, a domain level design specification can function with either orientation ($5'$-$3'$) for the DNA strands involved. However, it has been suggested in the literature (53) that certain $5'$-$3'$ orientations for the molecules may be preferable in practice because of asymmetries in the distribution of synthesis errors along the $5'$-$3'$ axis. In the hope that reversing $5'$-$3'$ orientations might change the distribution of synthesis errors to a more favorable one, which may in turn result in lower initial leak, we decided to try Design 3, which is the same as Design 2 but with $5'$-$3'$ orientations reversed.

Since the free energy contributions of individual nearest-neighbor base pair stacks towards double helix stability are not symmetric with respect to $5'$-$3'$ orientation, reversing the orientation of our design would perturb the thermodynamics of all our domains, including toeholds. This is undesirable as it could potentially alter the kinetics of desired strand displacement pathways. In spite of this, we went ahead with testing Design 3.

Experimentally, we found that Design 3 did have much lower initial leaks — reduced to 3-5% of the fuel concentration (see Fig. S22). This was an improvement from 10% in Designs 1 and 2. In addition, gradual leaks remained low, except in one particular case, that of $\mathrm{Produce}_{\mathrm{CApAq}}$ and $\mathrm{Helper}_{\mathrm{AAq}}$, where it was very high, approximately 150 /M /s.

### S4.5.1 Understanding the exceptionally high Produce-Helper leak

In order to understand the exceptionally high leak between $\mathrm{Produce}_{\mathrm{CApAq}}$ and $\mathrm{Helper}_{\mathrm{AAq}}$ (150 /M/s in $12.5\,\mathrm{mM}\,\mathrm{Mg}^{++}$ and 80 /M/s in $0.5\,\mathrm{M}\,\mathrm{Na}^{+}$), we performed careful debugging experiments where we measured the gradual leak between various modified versions of the $\mathrm{Produce}_{\mathrm{CApAq}}$ and $\mathrm{Helper}_{\mathrm{AAq}}$ species, including 1-2 base deletions. These experiments are summarized in Fig. S23; the inferred bimolecular leak rate constants, according to the methodology described in Section S4.2.3, are summarized in Table S6. These results suggest that an interaction between the partially complementary bases shown in Fig. S24 ('GGTA' on the overhang near the junction in $\mathrm{Produce}_{\mathrm{CApAq}}$ and 'ATCC' in the $\mathrm{Helper}_{\mathrm{AAq}}$ strand) could be responsible for accelerating the leak reaction between

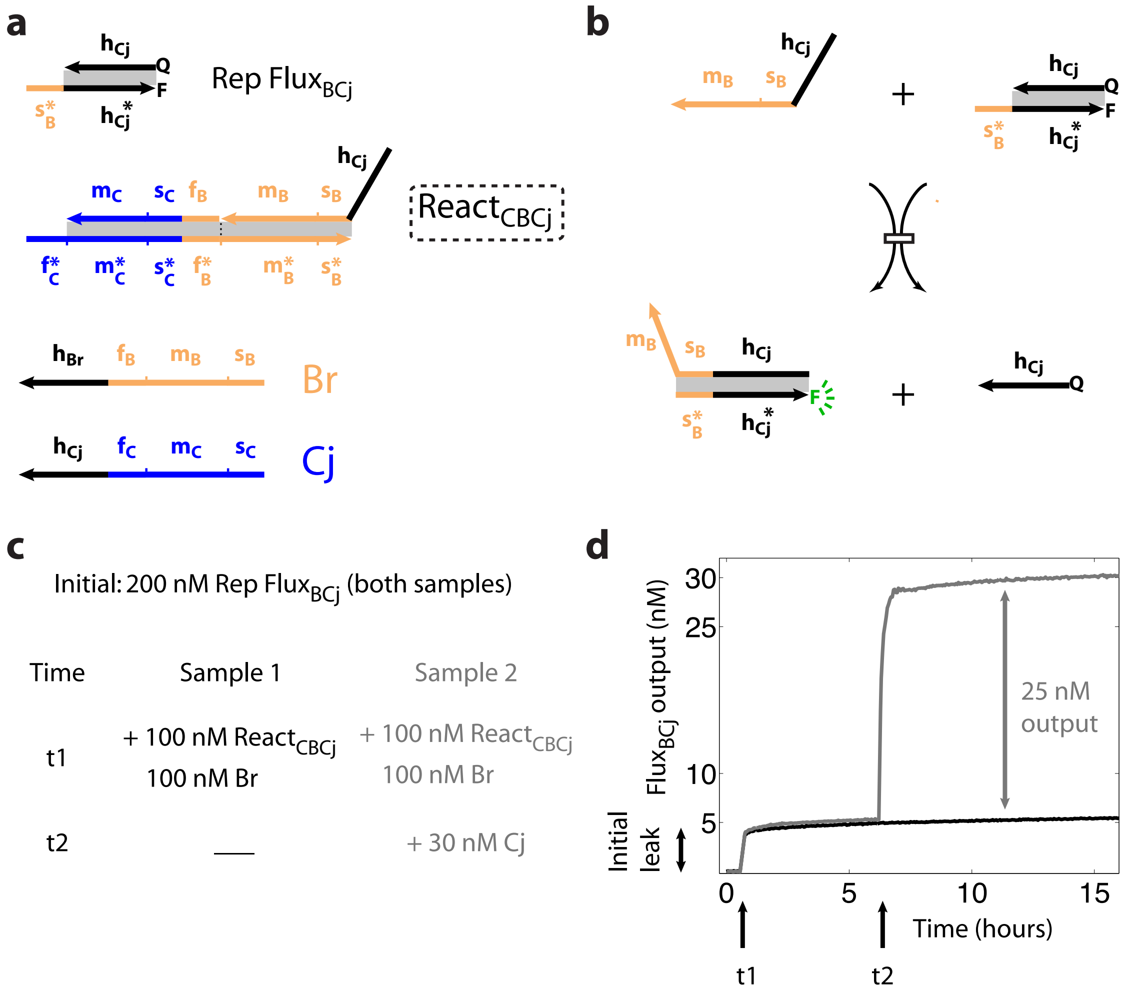

Figure S22: **Reduced initial and gradual leaks in Design 3.** Shown are measurements of React$_{\mathrm{CBCj}}$-Br leaks. (**a**) The molecules involved. RepFlux$_{\mathrm{BCj}}$ is a reporter for Flux$_{\mathrm{BCj}}$, which works like RepA in Fig. S20. (**b**) The reporter mechanism. (**c**) Experimental setup. Both sample 1 and 2 contain 200 nM RepFlux$_{\mathrm{BCj}}$ initially, and 100 nM React$_{\mathrm{CBCj}}$ and 100 nM Br are added to both at time $t_1$. (**d**) Experimental results. The initial leak is under 5%, which is 2x-3x lower than in Designs 1 and 2. After the initial leak goes to completion, only Sample 2 is triggered with 30 nM of Cj at time $t_2$. Note the fast triggering in Sample 2 and the much reduced gradual leak in Sample 1 (in general, 5x-10x lower than Design 1; see Fig. S20 for an example).

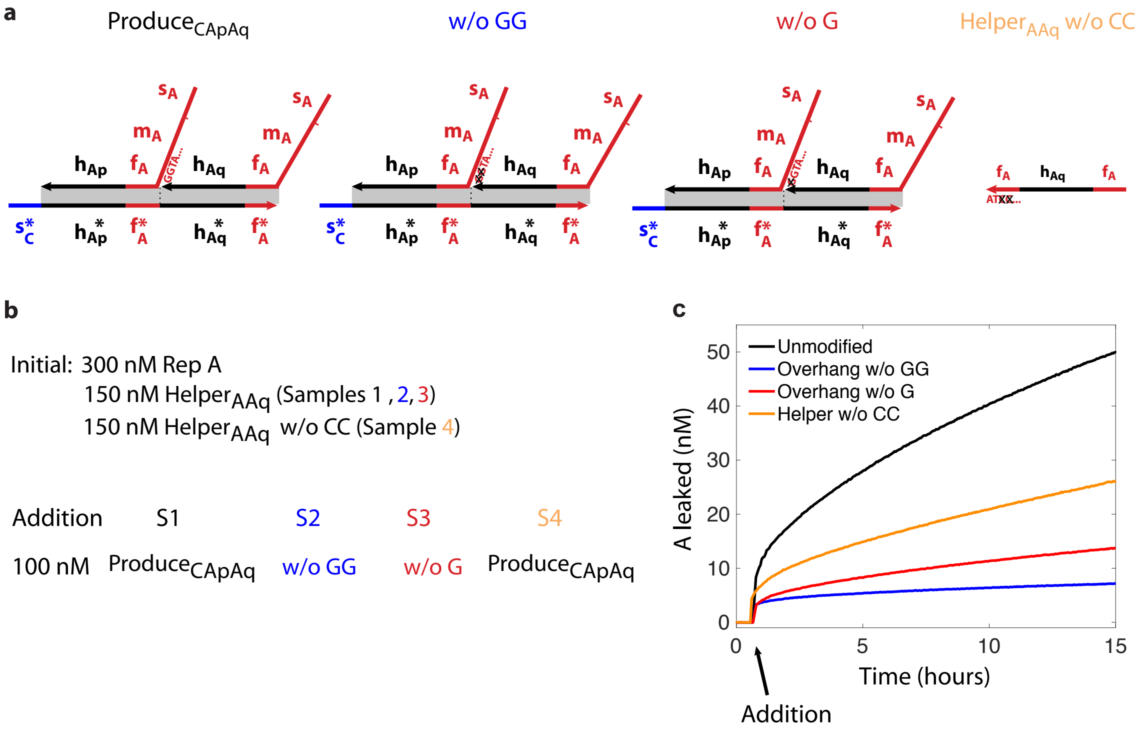

Figure S23: **Testing sequence-dependence of leak at nicks with tails (Design 3).** (**a**) Experiments used three variants of the complex $\mathrm{Produce}_{\mathrm{CApAq}}$ (unmodified, and with one or two deletions) and two variants of the strand $\mathrm{Helper}_{\mathrm{AAq}}$ (unmodified, and with two deletions). Black crosses indicate bases that were deleted within the respective synthesized oligonucleotides in each modified version. The relevant unmodified strands are the bottom 4 in Table S13 (i.e. D3_Produce_BOT_CApAq, D3_Ap, D3_Aq, and D3_Helper_AAq). (**b**) Experimental setup. $\mathrm{RepA}$ (also known as $\mathrm{Th}_{\mathrm{A}}$) is a fluorescent reporter for the signal strand A; the readout mechanism is shown in Fig. S20. (**c**) Quantitative estimates of bimolecular rate constants for these leak pathways, calculated according to the methodology described in Section S4.2.3, are listed in Table S6.

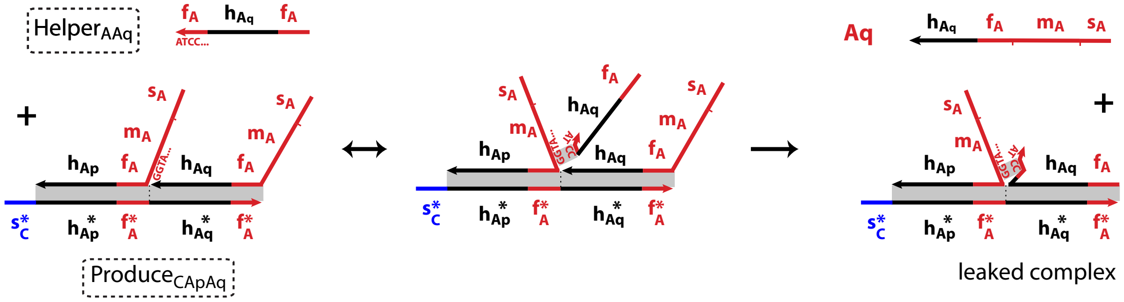

Figure S24: **Postulated remote toehold pathway for sequence-dependent leak at nicks.** Based on experiments measuring gradual leak rates with single-base changes at the positions illustrated ('ATCC' in $\mathrm{Helper}_{\mathrm{AAq}}$ and 'GGTA' in $\mathrm{Produce}_{\mathrm{CApAq}}$; see Table S6), these bases contribute to the high gradual leak between $\mathrm{Produce}_{\mathrm{CApAq}}$ and $\mathrm{Helper}_{\mathrm{AAq}}$ in Design 3. We hypothesize a remote-toehold mechanism for this leak: the complementarity between 'CC' of $\mathrm{Helper}_{\mathrm{AAq}}$ and 'GG' of $\mathrm{Produce}_{\mathrm{CApAq}}$ could co-localize the molecules fleetingly to accelerate strand displacement, acting similarly to a strong 2-base pair toehold (52). Note that another remote-toehold consisting of ATC/GGT base-pairs (with the middle T-G being a wobble base-pair) could also facilitate this spurious strand displacement reaction. This alternative possibility is not shown in the figure.

these two fuel species. We hypothesize a remote-toehold mechanism for this leak: the complementarity between 'CC' of $\mathrm{Helper}_{\mathrm{AAq}}$ and 'GG' of $\mathrm{Produce}_{\mathrm{CApAq}}$ could co-localize the molecules fleetingly to accelerate strand displacement, acting similarly to a strong 2-base pair toehold (52). We design against this particular gradual leak pathway in Design 4 (Section S4.6).

### S4.5.2 The role of cation choice in gradual leak: $\mathrm{Mg}^{++}$ vs $\mathrm{Na}^{+}$

While discussing leak measurements for Design 3 with Paul W. K. Rothemund, he suggested that performing these experiments with 0.5 - 1 M $\mathrm{Na}^{+}$ (as opposed to 12.5 mM $\mathrm{Mg}^{++}$) may result in lower gradual leak since $\mathrm{Mg}^{++}$ is known to stabilize DNA-DNA junctions (88–90). (This could in turn facilitate gradual leak pathways, by, for example, stabilizing the invasion of Helper strands at the junction of the Produce complex.)

When we repeated gradual leak measurements with Design 3 in 0.5 M $\mathrm{Na}^{+}$, we found that there was a reduction (across the board) by approximately a factor of 2. So, we altered our protocol at this stage to use 0.5 M $\mathrm{Na}^{+}$ instead of 12.5 mM $\mathrm{Mg}^{++}$. Even though DNA strand displacement kinetics in high sodium (0.5 -1 M $\mathrm{Na}^{+}$) (34, 37) was observed to be quite similar to that in 12.5 mM $\mathrm{Mg}^{++}$ (35), we experimentally verified that the kinetics of our desired pathways did not slow down significantly due to the change in salt conditions (experiments not shown).

### S4.5.3 Kinetics of desired pathways

Apart from investigating leaks, we also experimentally checked whether the desired strand displacement reactions were occurring with (roughly) the expected kinetics. We found that $\mathrm{React}_{\mathrm{BABr}}$ and $\mathrm{React}_{\mathrm{ACAp}}$ were slow to "trigger" — that is, when both their inputs were present, $\mathrm{React}_{\mathrm{BABr}}$ and $\mathrm{React}_{\mathrm{ACAp}}$ were much slower to release their outputs than expected. Compared to $\mathrm{React}_{\mathrm{CBCj}}$, where this triggering process takes about 20 minutes (Fig. S22), $\mathrm{React}_{\mathrm{BABr}}$ and $\mathrm{React}_{\mathrm{ACAp}}$ took about 10 hours (slower by a factor of 30).

We re-examined the MFE structures and partition functions of all the complexes involved in these slow strand displacement reactions in NUPACK. We found that the signal strands Ap and Aq, which serve as inputs to both $\mathrm{React}_{\mathrm{BABr}}$ and $\mathrm{React}_{\mathrm{ACAp}}$, had formed unintended hairpin structures in Design 3 (Fig. S25). In addition to the MFE structures, we found that the first two bases of the branch migration domain $\mathrm{m_A}$, both G's, were bound almost all the time in some (weak) hairpin or the other. This location is especially critical, as initiation of the first branch migration step is known to be among the slowest unimolecular steps in the strand displacement process and is important in determining kinetics (36). Given that Ap and Aq serve as inputs to both React complexes, we hypothesized that this unintended secondary structure was responsible for the slowdown in triggering both react steps.

### S4.6 Sequence design 4

In Design 4, we wanted to modify Design 3 to (i) speed up the triggering of $\mathrm{React}_{\mathrm{BABr}}$ and $\mathrm{React}_{\mathrm{ACAp}}$ by removing unintended secondary structure in Ap and Aq (Fig. S25) and (ii) reduce the gradual leak between $\mathrm{Produce}_{\mathrm{CApAq}}$ and $\mathrm{Helper}_{\mathrm{AAq}}$ by eliminating the remote-toehold mechanism postulated in Fig. S24.

First, we constructed a new heuristic score that seeks to quantify the presence of significant secondary structure in strands that are intended to be single-stranded. For a given base $b$ in a strand $S$, let $\mathrm{p}_{\mathrm{unpaired}}(b, S)$ be the fraction of the population that is unpaired at equilibrium in a solution where only $S$ is present, as predicted by NUPACK (considering single-stranded complexes only). Then the heuristic measure, which we call Single-Strand Unpaired (SSU), is the minimum of $\mathrm{p}_{\mathrm{unpaired}}$ across all bases in all strands that are supposed to be free of secondary structure. That is, if $T$ is the set of all strands that are supposed to be free of secondary structure,

$$\mathrm{SSU} := \min_{S\,\in\,T}\,\min_{b\,\in\,S}\,\mathrm{p}_{\mathrm{unpaired}}(b, S). \tag{16}$$

For Design 3, the SSU was only 0.13, and the base which was paired the most was one of the first two bases in the branch migration region $\mathrm{m_A}$ (illustrated in Fig. S25). This in itself could account for a 10-fold slowdown in strand displacement reactions involving Ap or Aq. Note that, among all the heuristic measures we have defined, SSU is the only measure where "larger is better".

We decided to modify Design 3 "by hand" to mitigate the problems described above. We identified 8 bases that, if changed, seemed to mitigate one or both of those issues, and identified by trial and error what degrees of freedom those bases had (that is, which options for their new identity did not introduce new secondary structure or malformed complexes as predicted by NUPACK). We changed 3 bases by hand as there seemed to be a clear "best choice" for those 3 bases. For the other 5 bases, we evaluated all possible candidates by brute force on our heuristic measures and chose a design that seemed satisfactory on all those measures. In particular, the SSU for the new design, which we call "Design 4-PRE" increased to 0.76, which was encouraging.

Experimentally, we found (i) a dramatic reduction in the $\mathrm{Produce}_{\mathrm{CApAq}}$-$\mathrm{Helper}_{\mathrm{AAq}}$ gradual leak, which reduced 10-fold from approximately 150 /M /s to 15 /M /s, and (ii) a dramatic (30-fold) speedup in the triggering of $\mathrm{React}_{\mathrm{BABr}}$, which was now comparable to $\mathrm{React}_{\mathrm{CBCj}}$. However, surprisingly, there was no speedup in the triggering of $\mathrm{React}_{\mathrm{ACAp}}$, which suggested that another factor was responsible for the slow triggering of $\mathrm{React}_{\mathrm{ACAp}}$.

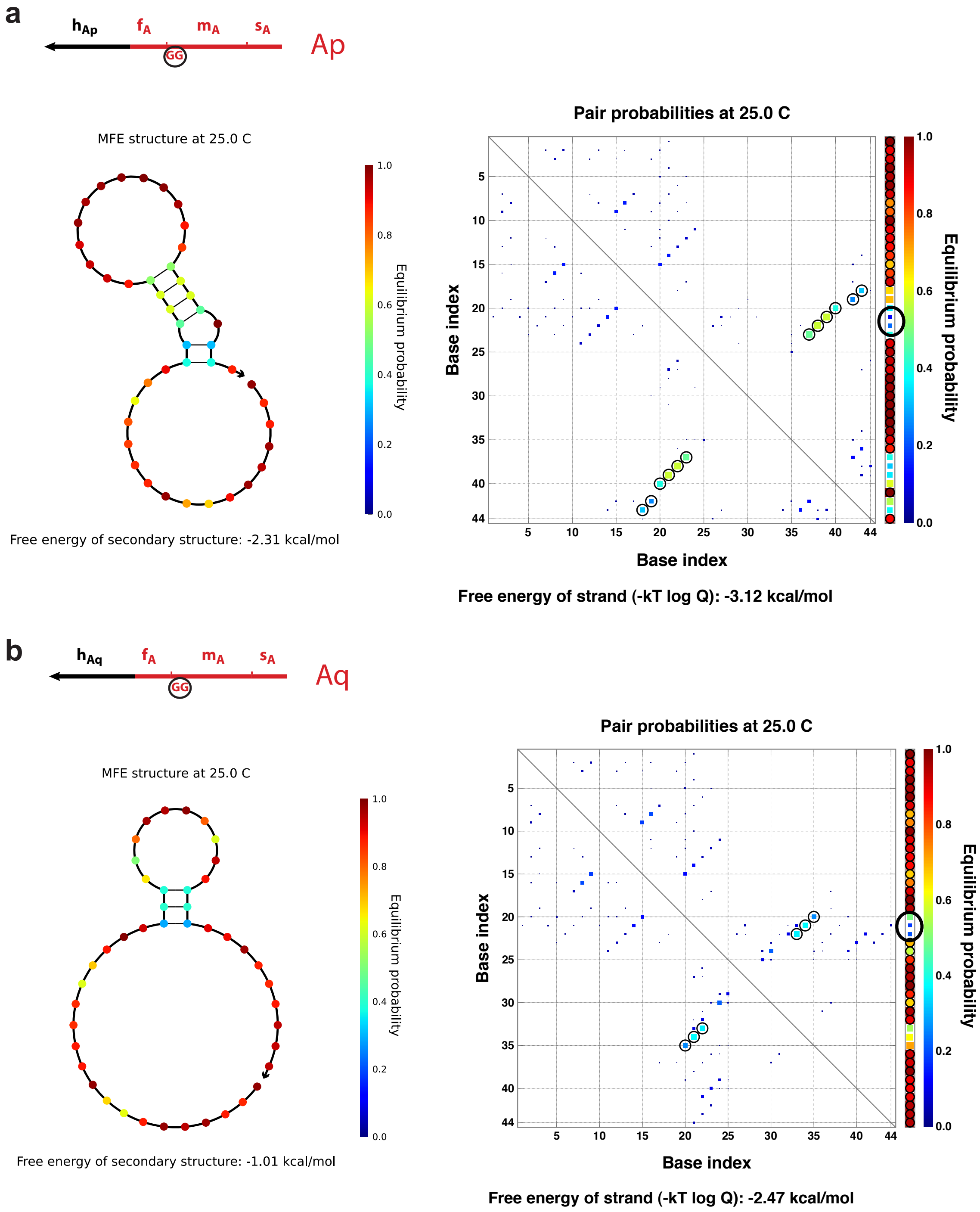

Figure S25: **Secondary structure is predicted to influence reaction rates.** NUPACK-predicted MFE structure and pair-probabilities matrix for Ap (**a**) and Aq (**b**) from Design 3. This secondary structure could slow down desired strand displacement pathways involving these strands. In particular, the first two bases (GG) of the branch migration region are base-paired most of the time (as a part of several weak hairpins).

On close re-examination of the thermodynamics of all the complexes, including intermediates, involved in triggering $\mathrm{React}_{\mathrm{ACAp}}$, we noticed that the initial toehold exchange reaction involved the two most imbalanced toeholds. The "forward" toehold, $\mathrm{f}_{\mathrm{A}}$, was the weakest and the "backward" toehold, $\mathrm{f}_{\mathrm{C}}$, was the strongest. In addition to that, $\mathrm{f}_{\mathrm{C}}$, being an "internal" toehold, would have an additional (coaxial) stack when bound (see Fig. S26). According to the principles of toehold exchange kinetics first explained in Zhang & Winfree (35), this imbalance of $\Delta\Delta G = \Delta G_{\mathrm{f}_{\mathrm{C}}} - \Delta G_{\mathrm{f}_{\mathrm{A}}}$ would slow down the forward toehold exchange rate by a factor of about $10^{\Delta\Delta G}$.

We attempted to balance these toehold energies by removing two base pairs from the internal toehold as shown in Fig. S26, effectively modifying $\mathrm{React}_{\mathrm{ACAp}}$ and $\mathrm{Back}_{\mathrm{AC}}$ to have a truncated toehold $\mathrm{f}_{\mathrm{C}}$. We named the resulting species $\mathrm{React}_{\mathrm{ACApi2}}$ and $\mathrm{Back}_{\mathrm{ACi2}}$. We call this new design, augmented with the 2-base truncations described above, Design 4. Experimentally, the two base-pair truncation resulted in a dramatic 30-fold speedup. All 3 react and all 3 produce steps in Design 4 had, according to our modeling, low enough gradual leak rates and high enough triggering rates that the DNA implementation could show oscillatory behavior.

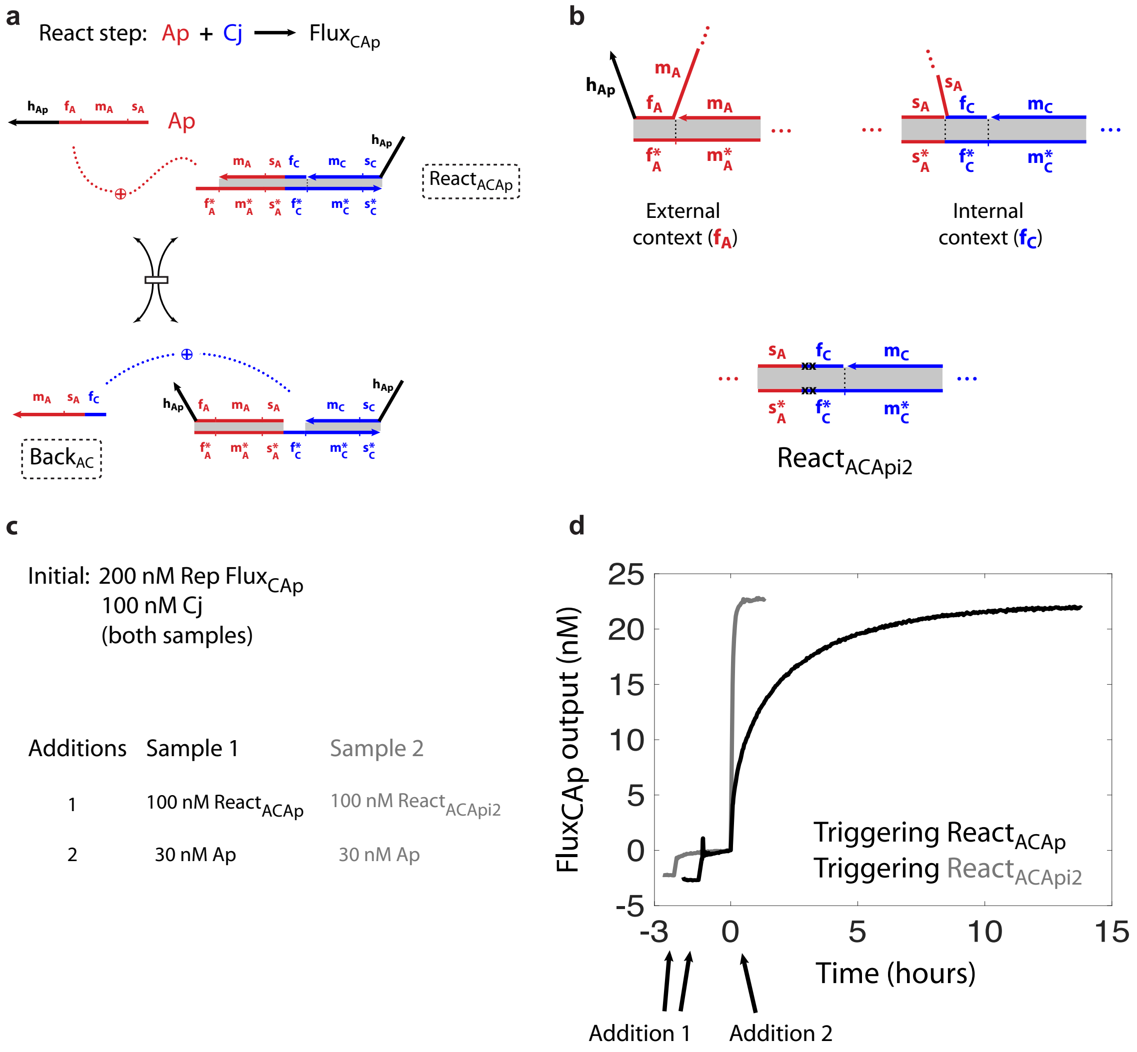

Initial: 200 nM Rep Flux$_{CAp}$
100 nM Cj
(both samples)

| Additions | Sample 1 | Sample 2 |
|---|---|---|
| 1 | 100 nM React$_{ACAp}$ | 100 nM React$_{ACApi2}$ |
| 2 | 30 nM Ap | 30 nM Ap |

Figure S26: **Toehold context affects kinetics.** Energy imbalance between the external toehold ($\mathrm{f_A}$) and the internal toehold ($\mathrm{f_C}$) causes slow triggering of $\mathrm{React_{ACAp}}$. (**a**) Recap of the toehold exchange reaction in triggering $\mathrm{React_{ACAp}}$. (**b**) External and internal contexts. The external toehold, when bound, has only one coaxial stack, whereas the internal toehold has one on either side. In order to balance the energies, we removed two base pairs from the internal toehold as indicated by truncating the $\mathrm{Back_{AC}}$ strand and the bottom strand of $\mathrm{React_{ACAp}}$ to yield $\mathrm{Back_{ACi2}}$ and $\mathrm{React_{ACApi2}}$. (**c**, **d**) Experiment illustrating that triggering $\mathrm{React_{ACApi2}}$ (Design 4) is much faster than $\mathrm{React_{ACAp}}$ (Design 4-PRE). Notice also the substoichiometric yield: addition of 30 nM of Ap results in the release of about 23 nM of $\mathrm{Flux_{CAp}}$, which is approximately 23% less than expected.

# S5 Experimental implementation of the Displacillator

## S5.1 Quantitative fluorescent readouts for measuring DNA implementation kinetics

Quantitative measurement of the dynamics of the DNA implementation is challenging because irreversibly consuming the signal strands A, B, C (e.g. using Reporter complexes of the kind described in Fig. S20) would in itself alter the kinetics one seeks to measure. An alternative method would be to tag the signal strands directly with fluorophores; however, the only distinction between free signal strands and bound signal strands in our CRN-to-DNA scheme is the state of the first toehold (e.g. $f_A$). Therefore, implementing this method would involve placing a fluorophore in the middle of every first toehold, which could perturb the kinetics of the DNA implementation since toehold energies are critical for strand displacement kinetics (35, 36).

Instead, we chose to observe the consumption of the fuel species, which provides an indirect measurement of the kinetics of the DNA implementation. In particular, we tag the Helper and CatHelper strands with fluorophores at the 5’ end, and the Produce complexes with quenchers at the 3’ end of the bottom strand (see Fig. S14). By using a distinct fluorophore for each pair of Helper and CatHelper strands, we can measure the kinetics of all three autocatalytic modules simultaneously. In all Displacillator experiments, the CatHelper strand is also present, and the term “Helper concentration” (e.g. as used in Fig. S27b, bottom) refers to the sum of Helper and CatHelper concentrations.

**a**

Initial: 100 nM React and Back species (both samples)

| Sample 1 | Sample 2 |
|---|---|
| 10 nM $\mathrm{Th_A, Th_B, Th_C}$ | 10 nM $\mathrm{Th_A}^\dagger, \mathrm{Th_B}^\dagger, \mathrm{Th_C}^\dagger$ |
| 75 nM Helpers $\mathrm{AAq}^\dagger, \mathrm{BBs}^\dagger, \mathrm{CCk}^\dagger$ | 75 nM Helpers AAq, BBs, CCk |
| 25 nM PL-CatHelpers $\mathrm{AAq}^\dagger, \mathrm{BBs}^\dagger, \mathrm{CCk}^\dagger$ | 25 nM CatHelpers AAq, BBs, CCk |

---

Addition 1: + 100 nM Produce species to both samples

Addition 2: + (0, 10, 13) nM of (Ap, Br, Cj) to both samples

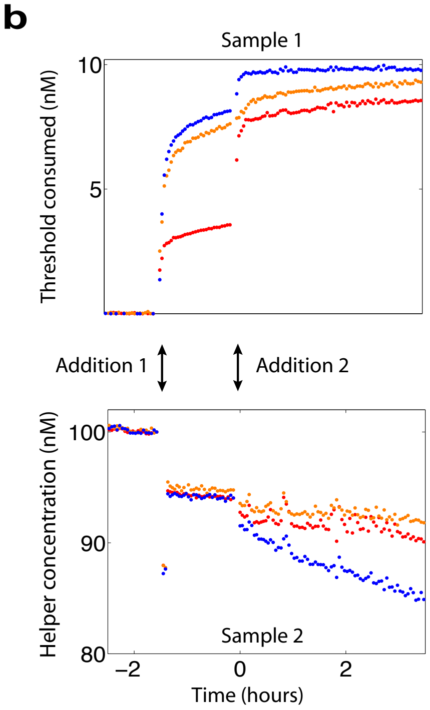

Figure S27: **Experimental setup for Displacillator experiments (Design 4).** (**a**) Two samples are used for each experiment: Sample 1 uses "plain" versions of Helper and CatHelper (marked by a $^\dagger$), which do not contain fluorophores, and thresholds $\mathrm{Th_A}$, $\mathrm{Th_B}$, and $\mathrm{Th_C}$ with fluorophores. Sample 2 uses plain versions of thresholds (marked by a $^\dagger$), which do not contain fluorophores, and Helper and CatHelper strands with fluorophores. Otherwise Samples 1 and 2 are identical. (In particular, Produce complexes in both samples are labeled with a quencher on the bottom strand). The ratio of Helper:CatHelper initial concentrations was experimentally optimized to the value 3:1. All fuel species except Produce complexes are present initially, along with 10 nM of each threshold. (**b**) After measuring the background, a mixture containing 100 nM of each Produce complex is added to each sample. This causes initial leak of signal strands A, B, and C, which is reflected in (i) the initial drop in Helper concentration (Sample 2), since Helper and CatHelper strands are consumed and quenched during initial leak and (ii) the initial spike in consumption of Thresholds (Sample 1) as the leaked signal strands are consumed. Once the initial leak stabilizes, we add (A, B, C) to kickstart oscillation with the initial conditions we desire.

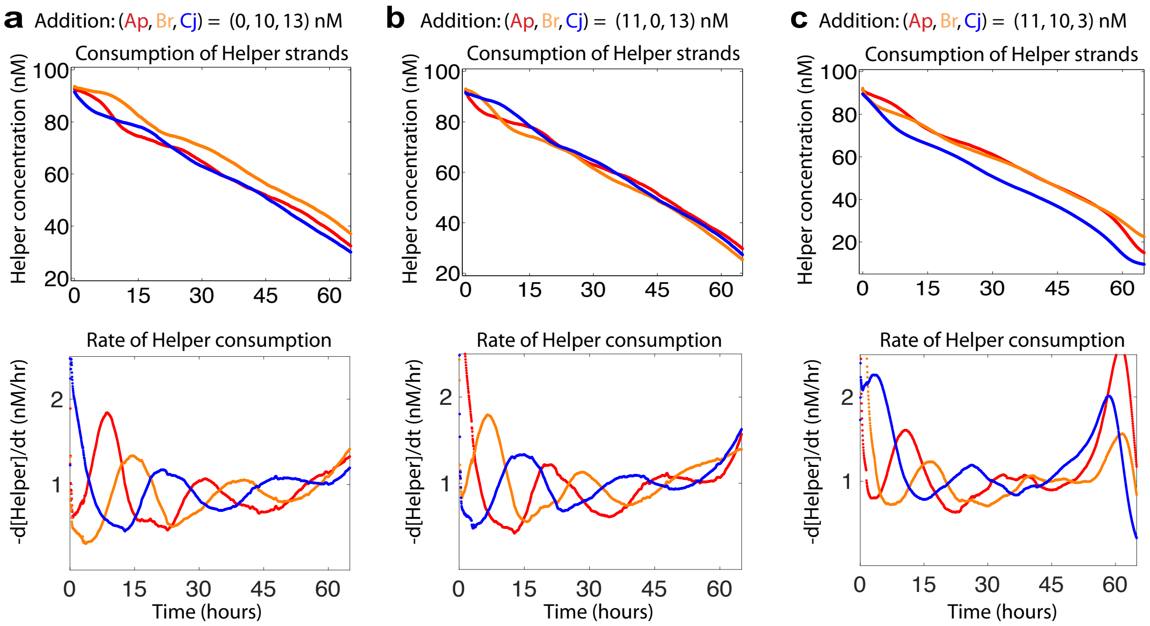

Figure S28: **Displacillator experiments from multiple initial conditions (Design 4).** (**a-c**) Helper concentrations are presented in the top row; time derivatives of those measurements are presented in the bottom row. Time derivatives indicate the instantaneous rate (in nM/hr) for each autocatalytic module, apart from the reduction of Helper concentration due to gradual leak. The sequential 'firing' of the autocatalytic modules in the expected order (as long as the fuel species are at significant concentration) indicates oscillatory behavior. This is the full data from the experiments described in Fig. 4 of the main text.

# S6 Mechanistic modeling

The predictable nature of the strand displacement reaction allows for kinetic modeling at the mechanistic level. Even the undesired non-idealities (leak, substoichiometric yield, toehold occlusion) are sufficiently understood that they can be captured in a mechanism-level kinetic model. In this section we describe how we constructed the mechanistic model of both the intended reactions and the undesired pathways, and how we fitted parameters to obtain a good fit with the measured oscillator dynamics. Importantly, this mechanistic model was used to obtain the extrapolated signal concentrations plotted in Fig. 4D of the main text.

**Formal CRNs as molecular programs vs. mechanistic-level CRNs as models.** It is important to keep in mind the two distinct roles that CRNs have in this work. First, a formal CRN is the molecular program that specifies the dynamics we wish to realize. For example, the rock-paper-scissors CRN (Fig. 1A of the main text) is the target of implementation. This is not to be confused with the mechanistic level CRN which describes the individual strand displacement steps. Our process of constructing the latter is described in Sections S6.1–S6.4 below.

The theory developed in ref. (43) for a closely related CRN implementation scheme, argues that the mechanistic CRN should approximate the formal CRN in the limit of high concentration of fuel species. However, that work did not explicitly model imperfections—leak reactions, incomplete yield, and toehold occlusion—as we do here. In Section S6.5 we numerically confirm that our mechanistic model well-approximates the rock-paper-scissors CRN in our regime. This allows us to argue that the cause of the oscillations in the strand displacement implementation is captured by the ideal rock-paper-scissors CRN.

**Software for simulation and fitting.** Mathematica (Wolfram Research) was used to simulate the mechanistic model and perform parameter fitting. The model was constructed with the help of the CRNSimulator package (91), which automatically constructs and simulates the system of ODEs for numerical simulation of a CRN. The Mathematica notebooks describing the mechanistic model, the fitting routines, as well as the datasets used for fitting, are available online (92).

## S6.1 Desired pathway modeling

Each intended strand displacement interaction (Figs. S7–S9) is modeled as a bimolecular reaction

$$[\text{complex}]_1 + [\text{strand}]_1 \xrightarrow{k} [\text{complex}]_2 + [\text{strand}]_2, \tag{17}$$

where $[\text{strand}]_1$ and $[\text{strand}]_2$ are the displacing and displaced strands respectively, and $[\text{complex}]_1$ and $[\text{complex}]_2$ are the complexes before and after displacement. The rate constants $k$ are potentially unique for every displacement reaction and were determined in separate experiments (see Table S2). Here we think of reversible strand displacement reactions as two separate reactions with different $k$. If $[\text{complex}]_2$ does not have an open toehold, we consider it to be effectively inert and omit it in the model.

As discussed in the main text and Fig. S17, we observed that the intended strand displacement reactions had less than expected yield (substoichiometric yield). This was consistent with the hypothesis that some fraction of bad fuel species consume inputs without releasing functioning outputs. To model this, we assume that a fraction of outputs of React and Produce complexes are inert (truncated). Specifically, fraction $\tau$ of React complexes has a truncated Flux strand, and fraction $1 - \tau$ is error-free. For Produce complexes, fraction $\tau$ has a truncated first output signal, fraction $\tau$ has a truncated second output signal, and the remaining fraction $1 - \tau$ is error-free. (For small $\tau$ it is unlikely that both outputs are truncated.)

Together with separate reactions for React and Produce complexes with truncated fuels, the strand displacement interactions shown in Fig. S7–S9 are described by $84$ chemical reactions in the mechanistic model.

## S6.2 Leak pathway modeling

Of the 3 types of gradual leak shown in Fig. S10, our mechanistic model includes only the "Produce-Helper" leak. The exclusion of other leak types is based on theoretical and experimental considerations as follows.

The modeled "Produce-Helper" gradual leak is expected to be significant because it occurs between two high concentration fuel species. Further, the putative gradual leak mechanism, where the Helper strand invades at the nick of the Produce complex (between the two outputs), cannot be mitigated by clamps. Indeed, this leak was experimentally shown to be significant (Table S6).

In contrast, the omitted "React-second input" gradual leak occurs between a high concentration auxiliary species (React) and a low concentration signal species. Further, although the "React-Produce" gradual leak occurs between two high concentration auxiliary species, the clamp on the React complex is expected to significantly diminish the rate of the blunt-end strand displacement. Indeed, experimental measurements of this leak confirmed that it was at least a factor of $10$ less than the "Produce-Helper" leak (data not shown).

Leak interactions result not only in undesired release of otherwise sequestered strands, but also the production of unwanted complexes that may have downstream effects. The complex produced as a result of the "Produce-Helper" leak (Fig. S10b) can undergo a strand displacement interaction with a Flux strand generating one signal strand (Fig. S11b). Note that this is fewer than the expected 2 signal strands produced by a fresh Produce complex. Thus, leak can contribute to apparent substoichiometric yield. We incorporated this reaction into our model; however, it was not sufficient to explain the dampening we observed, suggesting that other mechanisms are responsible for substoichiometric yield (see Section S6.1).

The 3 leak reactions (one for each of the three formal reactions) and their consequences contribute an additional 6 reactions to the mechanistic model.

In addition to the gradual leak discussed above, we observed substantial amount of initial leak (see e.g., Table S4 and Fig. S26). Initial leak mechanisms are not well understood and thus in general present a challenge to mechanistic level modeling. To avoid unnecessarily complicating our mechanistic model, we chose to simulate initial leak as, effectively, instantaneous gradual leak. In other words, we start the simulation with fraction $\lambda$ of Produce and Helper fuels already leaked, resulting in a corresponding increase in initial signal along with the leaked complexes (Fig. S10, S11).

## S6.3 Occlusion modeling

An open toehold domain and its complement occur not only between a complex and its displacing strand, but also in contexts where a strand displacement cannot occur (Fig. S13). These "toehold occlusion" interactions are expected to have an overall slowdown effect on the kinetics (see the

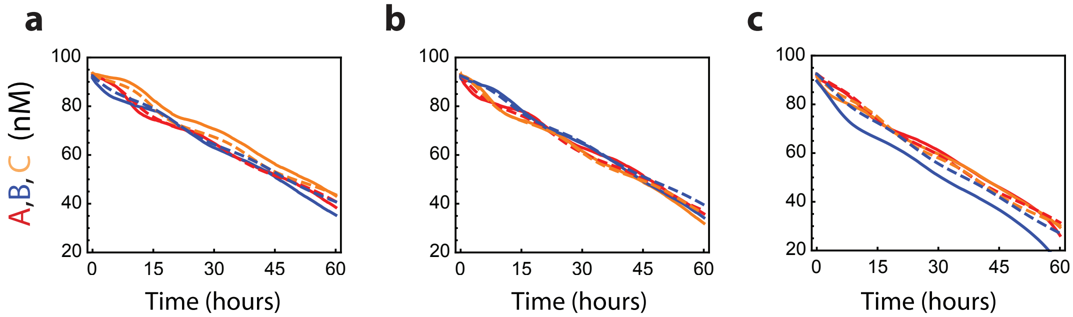

Figure S29: **Comparison of mechanistic model to experimental data.** (**a**)-(**c**) Measured Helper A, B, C concentrations (solid) versus model fit (dashed) are shown for the three sets of initial conditions used in experiments. Note that the fit is performed not to the Helper concentrations but to their derivatives (see Fig. 4B in the main text).

discussion of spurious toehold binding in ref. (39)). We model toehold occlusion interactions by a reversible bimolecular reaction specific to each toehold shared between complex and strand:

$$[\text{complex}] + [\text{strand}] \underset{k_{\text{off}}}{\overset{k_{\text{on}}}{\rightleftharpoons}} [\text{inactive-complex-strand}]. \tag{18}$$

The [inactive-complex-strand] species do not interact in strand displacement reactions; in this way, the amount of available [complex] and [strand] is reduced. Since leak reactions are toehold-independent, Helper strands and Produce complexes sequestered in [inactive-complex-strand] can still leak in our model. Thus the leak rate is not a function of toehold occlusion.

Kinetic parameter $k_{\text{on}}$ was (somewhat arbitrarily) set to $2 \times 10^6$/M/s. Kinetic parameter $k_{\text{off}}$ was fit (see below).

## S6.4 Parameter fitting

**Full oscillator.** We fit three global parameters: $\tau$, the fraction of truncated outputs; $\lambda$, the fraction of Produce and Helper fuels involved in initial leak; and $k_{\text{off}}$, the spurious toehold binding dissociation rate. Further, we fit the initial amounts of signal strands (A, B, C) for each of the three experiments that were initialized with different amounts of the signals. These additional parameters compensate for uncertainty in initial signal concentration due to leak and pipetting, as well as for inaccuracies of assuming that each reaction module is governed by identical truncation, initial leak, and toehold occlusion parameters. These initial signal values modify (add or subtract to) the amount of signals generated in the initial leak.

The Helper traces in all three initial conditions quickly reached a value consistent with roughly $0.075$ initial leak $\lambda$, the value that we used throughout (see Fig. S29). The other parameters were fit to the Helper numerical derivatives (Fig. 4B of the main text), which are expected to be less susceptible to systematic offsets than the absolute Helper signal. The fitting is performed by Mathematica's `FindMinimum` function, with a mean squared error loss function.

In order to obtain relatively noise-free numerical derivatives of Helper consumption to use in fitting, we smoothed the collected data using a 30 datapoint moving average. The numerical derivatives were then computed using Mathematica's `DerivativeFilter` function. In order to focus on the most meaningful part of the trajectory—ignoring initial transients and the dynamics after

| $\tau$ | $\lambda$ | $k_{\text{off}}$ |
|---|---|---|
| 0.11 | 0.075 | 0.226 /s |

| initial condition | $A$ | $B$ | $C$ |
|---|---|---|---|
| 1 | $-6.32$ nM | $-0.94$ nM | 1.06 nM |
| 2 | $-3.28$ nM | $-4.92$ nM | 2.74 nM |
| 3 | $-2.82$ nM | $-0.09$ nM | $-0.07$ nM |

Table S7: **Fitted parameters for the full oscillator.** $\tau$: truncated output fraction, $\lambda$: initial leak fraction, $k_{\text{off}}$: spurious toehold binding dissociation rate. Meaning of the initial A, B, C concentration parameters: We expect that the initial signal concentrations correspond to the amount leaked, minus the amount consumed by the Threshold complexes, plus the amount manually added. Parameter $\lambda$ captures the initial leak, while the initial A, B, C concentration parameters capture the difference between the amount manually added and the Threshold complexes. Note that the interaction of Threshold with the signals is assumed to be fast compared with the rest of the system dynamics and is not explicitly modeled here. Thus negative signal concentrations correspond to the net removal of leaked signal due to Threshold complexes. The fitting is done to minimize mean squared error of the Helper derivatives (Fig. 4B of the main text) as described in this section. The three initial conditions correspond to the three runs shown in Fig. 4B of the main text, with added amounts of (A, B, C) being $(0, 10, 13)$ nM, $(11, 0, 13)$ nM, and $(11, 10, 13)$ nM, respectively

fuels are consumed—we removed the first 20 data points (corresponding to $\sim 52$ minutes), and set the end of fitting at data point 1000 corresponding to $\sim 50$ hours.

The fitted parameters are shown in Table S7.

**Autocatalytic modules.** We used the three global parameters $\tau$, $\lambda$, and $k_{\text{off}}$ from the full oscillator fit. Since the time of onset of exponential amplification is sensitive to the exact threshold concentration, for each of the three modules we additionally fit the initial amount of threshold. (Alternatively, we could have fit three "$\Delta\lambda$" parameters to account for module-dependent initial leak; we make no claim as to the origin of threshold concentration perturbations, be they pipetting inaccuracy, leak pathways, or other effects.) The fit was to the numerical derivatives of the Helper strand concentration, computed as in the full oscillator.

## S6.5 Agreement of the mechanistic model with the molecular program CRN

Our pipeline starts with the formal CRN specification: in this case, the rock-paper-scissors CRN. Are the realized signal dynamics quantitatively consistent with the specification? Although we did not have direct access to signal concentrations in the test tube, we used the signal concentrations extrapolated from the mechanistic model and checked their consistency with the ideal CRN dynamics.

In our pipeline we used the topology of the rock-paper-scissors CRN as specification, but did not attempt to target particular reaction rate constants. The theoretical treatment developed in ref. (43) derives the reaction rate constants of the simulated CRN as a function of the rate constants of each strand displacement step and fuel concentrations. Thus, we utilize this analysis in order to obtain the rate constants of the ideal rock-paper-scissors CRN that should be most consistent with the mechanistic model, and thus with the test tube implementation. Note that analytically deriving the rock-paper-scissors rate constants from the mechanistic model, rather than through numerical

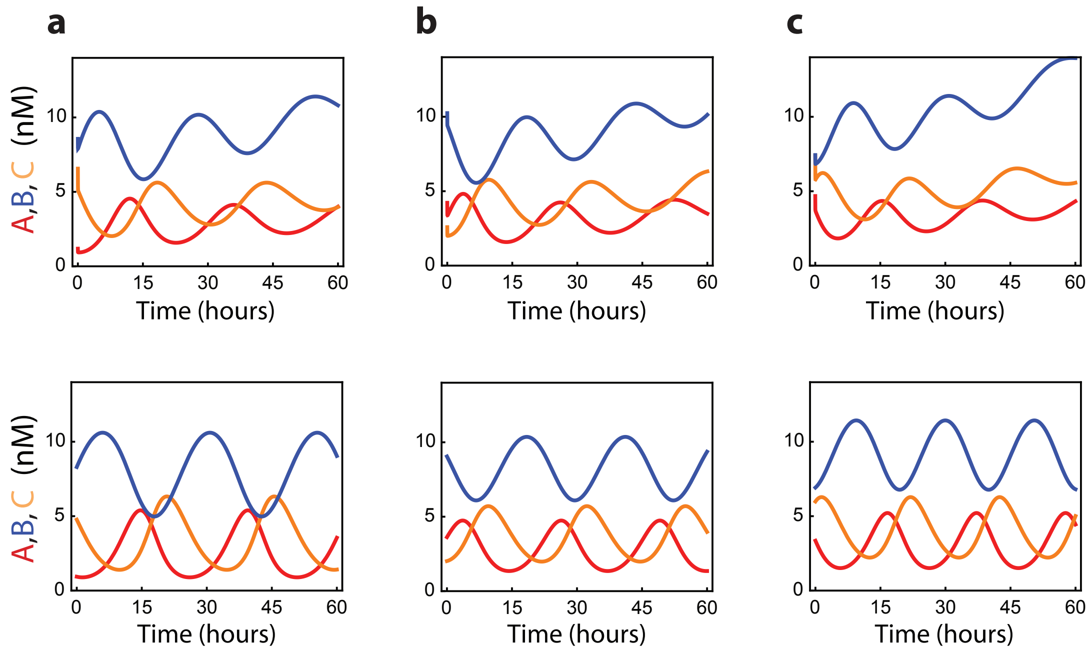

Figure S30: **Comparison of mechanistic model and corresponding formal CRN.** (**a**)-(**c**) Extrapolated A, B, C signal concentrations (top) versus formal CRN (bottom) are shown for the three sets of initial conditions used in experiments.

fitting, reiterates the efficaciousness of our understanding of the mechanism.

We modify the treatment of ref. (43) in two ways. First, we take into account toehold occlusion, which slows down the kinetics. Second, we disregard the "buffering effect" that occurs when a large fraction of signals is sequestered in $\mathrm{ReactInt}$ complexes. We are justified in doing so because the measured forward ($k_{\mathrm{fwd1}}$) and backward ($k_{\mathrm{back}}$) rate constants for the first react step (Table S2) are strongly biased backward, suggesting that most of the signals remain free.

The mechanistic model makes the following predictions regarding toehold occlusion and fuel concentrations. The fraction of occluded signal strands varies roughly between $0.25$ (initially) and $0.15$ (at $60$ hours). The amounts of non-occluded React fuels ranges from about $40$ nM to $20$ nM, and the amount of non-occluded Backward fuels ranges from about $60$ nM to $100$ nM. The variation occurs roughly linearly with the progress of the reaction over 60 hours. For each of these fractions and concentrations, we take the average of the regime limits: let $\phi = 0.8$ be the average fraction of signal strands that are not occluded, let $c_{\mathrm{React}} = 30$ nM and $c_{\mathrm{Back}} = 80$ nM be the average concentrations of non-occluded React complex and Backward strand fuels, respectively.

In the following discussion, we derive the formal rate constant for the reaction $\mathrm{B} + \mathrm{A} \to 2\,\mathrm{B}$ (see Fig. S9). The formal rate constants for the other two reactions are determined in the same manner. Let $[\mathrm{A}]$ be the total concentration of signal strands A, with any history domain. This amount consists of two populations: the non-occluded (free) strands $\mathrm{A}_{\mathrm{free}}$, and the occluded strands $\mathrm{A}_{\mathrm{occ}}$. Thus, $[\mathrm{A}] = [\mathrm{A}_{\mathrm{free}}] + [\mathrm{A}_{\mathrm{occ}}]$. In the same fashion, we will use subscripts "free" and "occ" to indicate non-occluded and occluded versions of other complexes and strands as well. Let $[\mathrm{ReactInt}_{\mathrm{free}}]$ be the concentration of non-occluded ReactInt complex (summing over the two possible history domains of the sequestered $B$ input). The displacement of the Flux strand from ReactInt by signal

A is expected to be the rate limiting step of the entire module, as argued in ref. (43). (This is essentially because all other forward reactions involve at least one fuel, which is present in high concentration. In contrast in this step both ReactInt and A are non-fuel, low concentration species.) The instantaneous rate of ReactInt + A strand displacement reaction is $k_{\text{fwd2}} \cdot [\text{ReactInt}_{\text{free}}] \cdot [\text{A}_{\text{free}}]$ which can be re-written as (by multiplying by 1):

$$k_{\text{fwd2}} \cdot \frac{[\text{B}_{\text{free}}]}{[\text{B}]} \cdot \frac{[\text{A}_{\text{free}}]}{[\text{A}]} \cdot \frac{[\text{ReactInt}_{\text{free}}]}{[\text{B}_{\text{free}}]} \cdot [\text{B}] \cdot [\text{A}], \tag{19}$$

We assume signal B (again summed over the different history domains) is in pseudoequilibrium with ReactInt through the strand displacement reaction $\text{B}_{\text{free}} + \text{React}_{\text{free}} \underset{k_{\text{back}}}{\overset{k_{\text{fwd1}}}{\rightleftharpoons}} \text{Backward}_{\text{free}} + \text{ReactInt}_{\text{free}}$. If we further assume that the concentrations of fuels (React complex and Backward strand) are constant, we obtain the relationship:

$$\frac{[\text{ReactInt}_{\text{free}}]}{[\text{B}_{\text{free}}]} = \frac{k_{\text{fwd1}} \cdot c_{\text{React}}}{k_{\text{back}} \cdot c_{\text{Back}}}.$$

Further, assuming $\text{A}_{\text{free}}$ and $\text{B}_{\text{free}}$ are in pseudo-equilibrium with their occluded versions such that a fixed fraction $\phi$ is non-occluded, we have $\phi = \frac{[\text{A}_{\text{free}}]}{[\text{A}]} = \frac{[\text{B}_{\text{free}}]}{[\text{B}]}$. Thus, eq. 19 can be written as:

$$k_{\text{fwd2}} \cdot \phi^2 \cdot \frac{k_{\text{fwd1}} \cdot c_{\text{React}}}{k_{\text{back}} \cdot c_{\text{Back}}} \cdot [\text{B}] \cdot [\text{A}]. \tag{20}$$

Thus the rate constant for the effective reaction $B + A \xrightarrow{k} 2B$, acting on total signal strand concentrations, is:

$$k = k_{\text{fwd2}} \cdot \phi^2 \cdot \frac{k_{\text{fwd1}} \cdot c_{\text{React}}}{k_{\text{back}} \cdot c_{\text{Back}}}. \tag{21}$$

Instantiating $\phi$, $c_{\text{React}}$, and $c_{\text{Back}}$ with the averages discussed above, and using the separately measured $k_{\text{fwd1}}$, $k_{\text{back}}$, $k_{\text{fwd2}}$ for each reaction module (from Table S2), we derive the following formal CRN with numerical rate constants (units of /M/s):

$$\text{B} + \text{A} \xrightarrow{18813} 2\ \text{B}$$

$$\text{C} + \text{B} \xrightarrow{6318} 2\ \text{C}$$

$$\text{A} + \text{C} \xrightarrow{8247} 2\ \text{A}.$$

Deterministic mass-action ODE simulations of this three-reaction CRN (Fig. S30), using the same initial concentrations [A], [B], and [C] that appear in the mechanistic model, we obtain qualitatively similar trajectories, with comparable frequencies, amplitudes, offsets, and phases.

## S6.6 Using the mechanistic model to interrogate deviations from ideal CRN behavior

While the target formal CRN gives an idealized description of the high level behavior, the mechanistic model can be used to better understand the deviations from the ideal behavior due to the underlying strand displacement implementation, including the previously described non-idealities. In this section we consider changes to the initial concentrations of fuels and signal species, and describe how the mechanistic model gives us more insight into the behavior of the system beyond that possible by analyzing only the target CRN. Our effort focuses on maximizing the number of oscillations, and on speeding-up the time scale of the oscillations.

First, consider the effect of tuning the CatHelper concentration. Recall that CatHelper is intended to compensate for the dampening due to substoichiometric completion caused by truncated outputs. Fig. S31 shows that without CatHelper the oscillations are severely dampened even before the fuels run out, and that with too much CatHelper the system is instead amplifying. Our choice of $0.25$ of CatHelper seems to compensate well for the truncated outputs.

To better understand the parameters tuning the total number of oscillations and the oscillation period, we deobfuscate the contribution of different factors by removing leak (initial and gradual) and dampening due to substoichiometric completion (truncation fraction) from the mechanistic model. Note that remaining sources of deviation from ideal CRN dynamics include the kinetic approximations such as those in Section S6.5, the consumption of the fuels, and the non-idealities due to toehold occlusion. Fig. S32ab confirms that increasing the initial concentrations of fuels permits a longer running oscillator, with more oscillations overall.

To speed up the oscillations, first note that scaling up the initial signal concentrations in the rock-paper-scissors CRN shortens the period by the same factor. (Indeed, the kinetics of any CRN with exclusively bimolecular reactions speeds up by a factor of $c$ if all initial concentrations are increased by the same factor $c$.) Thus, it is natural to increase the initial signal concentrations in the mechanistic model. Fig. S32c shows that this indeed speeds up the oscillations, but at the cost of sustaining fewer of them overall. This tradeoff is due to faster fuel consumption with increased oscillation amplitude. To compensate, we can increase the fuel concentrations as well. Increasing the initial signal and fuel concentrations in Fig. S32d by a factor of $2$ speeds up the dynamics only very slightly. This effect is due to toehold occlusion becoming more dominant at higher concentrations. (Less than linear speedup is due entirely to toehold occlusion. This is because the only unimolecular reactions in the mechanistic model are the reactions describing the dissociation of occluded species. Without toehold occlusion, the mechanistic model would be entirely bimolecular, and the usual bimolecular scaling would apply. )

Finally, we repeat the same simulations but using the full mechanistic model with the non-idealities of leak and substoichiometric completion in Fig. S33. The effect of these non-idealities substantially degrades oscillator performance. This argues that reducing leak and substoichiometric completion is essential to further improvements in the oscillator—an observation that likely extends to other dynamical systems.

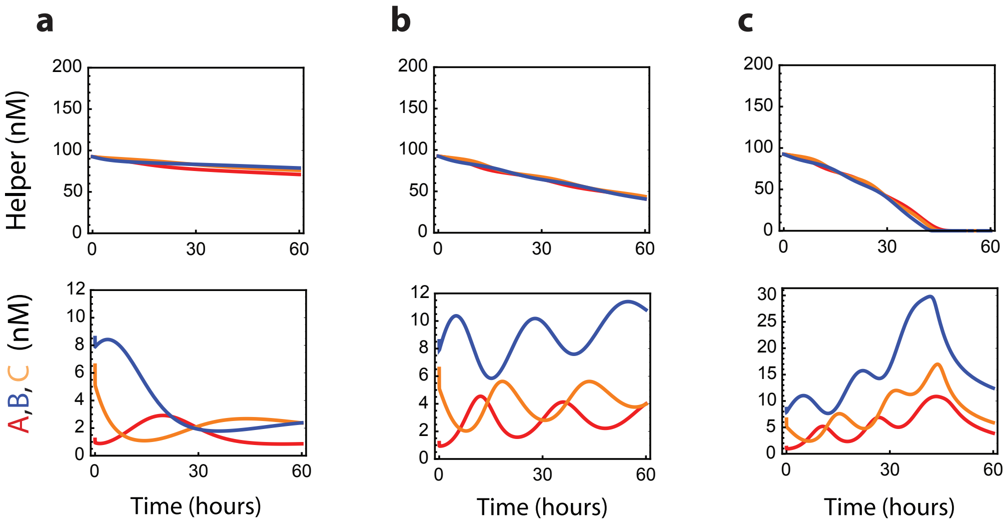

Figure S31: **Effect of CatHelper in the mechanistic model.** Other than the CatHelper fraction, all parameters are as those described in Section S6.4 (best fit) corresponding to initial condition 1. (**a**) No CatHelper. (**b**) 0.25 fraction of CatHelper (used experimentally). (**c**) 0.3 fraction of CatHelper.

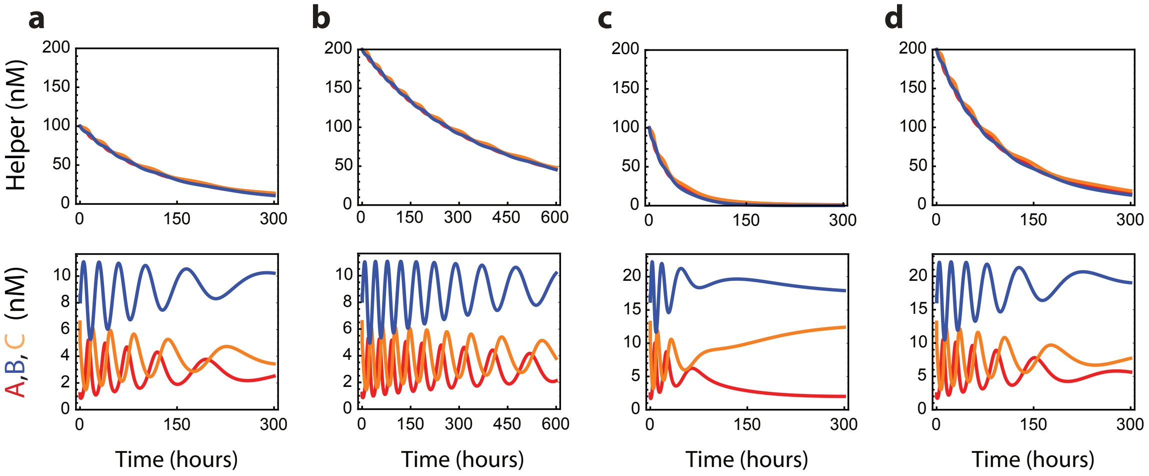

Figure S32: **Toward more and faster oscillations in the mechanistic model without leak and truncation ($\tau = 0$).** Since there is no dampening due to truncated signals, we also use no CatHelper. (**a**) Normal parameters corresponding to initial condition 1 in Section S6.4. Fuels are initially at 100 nM. (**b**) 2× as much fuels. (**c**) 2× as much initial signals. (**d**) 2× as much fuels and initial signals.

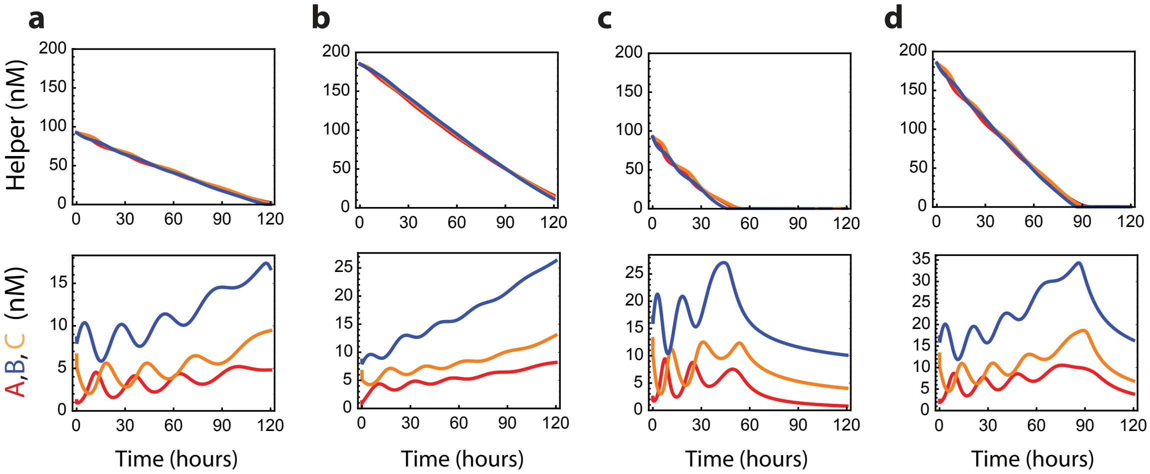

Figure S33: **Toward more and faster oscillations in the mechanistic model with leak and truncations.** Same as Fig. S32, but using the normal (best fit) parameters for gradual and initial leak, and truncation fraction from Section S6.4, as well as the normal CatHelper fraction of $0.25$. (**a**) Normal parameters corresponding to initial condition $1$ in Section S6.4. Fuels are initially at $100$ nM. (**b**) $2\times$ as much fuels. (**c**) $2\times$ as much initial signals. (**d**) $2\times$ as much fuels and initial signals.

## S7 Piperine: A CRN-to-DNA compiler

Through the four rounds of sequence design and experimental debugging presented in Sections S4.2, S4.4, S4.5, and S4.6, we identified domain-level and sequence-level design principles for mitigating spurious "leak" reactions and balancing rate constants in DNA strand displacement reaction cascades. We translated these design principles into a set of quantitative heuristic functions. Each individual function in this set calculates a number that describes the violations of one design principal in a given DNA strand displacement cascade. Taken together, they detect sequence-level motifs that may contribute to poor experimental performance (see Section S4.3).

During the many design-experiment iterations mentioned above, these heuristics allowed us to track the incremental improvements made with each design alteration. This encouraged us to construct an automated sequence design pipeline that incorporates these heuristic functions to help ensure good experimental performance of the DNA systems it generates. To test this possibility, we wrote an automated CRN-to-DNA compiler named "Piperine", which interfaces intimately with the Pepper Compiler, StickyDesign, and related DNA design and analysis tools (54). The Piperine compiler accepts a plain-text file describing a formal CRN and returns the sequences of a DNA implementation intended to approximate its dynamical behavior. This section describes the basic principles underlying our Piperine compiler; Section S8 describes our use of an earlier version of the software to generate another DNA implementation of the rock-paper-scissors formal CRN which demonstrated oscillatory dynamics in the test-tube with no subsequent re-design and optimization.

Piperine generates a list of candidate sequence designs implementing the target CRN, ranks them according to the heuristic measures, then selects the optimal design for the user to purchase and use in experiments. This process begins with converting lines of text, each describing a component reaction of the input CRN, into the domain-level complementarity rules for the DNA implementation. Piperine compiles these rules into nucleotide-level complementarity constraints and populates the toehold domains with sequences designed to be energetically balanced in all relevant binding contexts. Piperine then generates nucleotide sequences satisfying these constraints through sequence symmetry minimization (29). The algorithms performing toehold design and sequence symmetry minimization are stochastic, meaning each execution using the same set of constraints yields a different sequence design. Piperine generates many candidate designs in this manner before calculating their scores according to the heuristic measures. The lowest sum-of-ranks over the heuristic scores is selected as the "best" design, which Piperine reports to the user. Fig. S34 shows a detailed overview of this process.

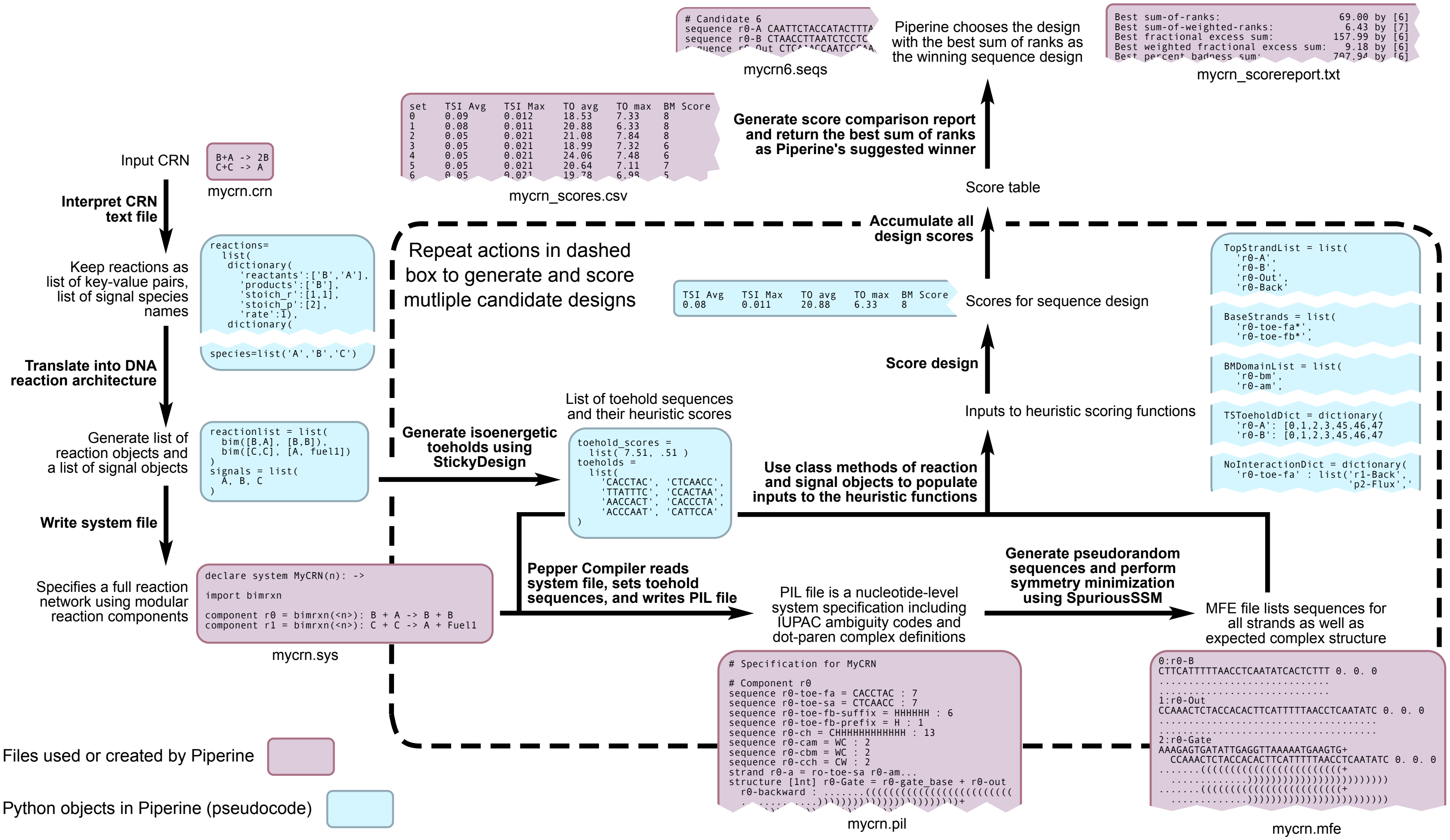

mycrn.crn
```
B+A -> 2B
C+C -> A
```

```
reactions=
  list(
   dictionary(
     'reactants':['B','A'],
     'products':['B'],
     'stoich_r':[1,1],
     'stoich_p':[2],
     'rate':1),
   dictionary(

species=list('A','B','C')
```

```
reactionlist = list(
  bim([B,A], [B,B]),
  bim([C,C], [A, fuel1])
)
signals = list(
  A, B, C
)
```

mycrn.sys
```
declare system MyCRN(n): ->

import bimrxn

component r0 = bimrxn(<n>): B + A -> B + B
component r1 = bimrxn(<n>): C + C -> A + Fuel1
```

```
toehold_scores =
  list( 7.51, .51 )
toeholds =
  list(
    'CACCTAC', 'CTCAACC',
    'TTATTTC', 'CCACTAA',
    'AACCACT', 'CACCCTA',
    'ACCCAAT', 'CATTCCA'
)
```

mycrn.pil
```
# Specification for MyCRN

# Component r0
sequence r0-toe-fa = CACCTAC : 7
sequence r0-toe-sa = CTCAACC : 7
sequence r0-toe-fb-suffix = HHHHHH : 6
sequence r0-toe-fb-prefix = H : 1
sequence r0-ch = CHHHHHHHHHHHH : 13
sequence r0-cam = WC : 2
sequence r0-cbm = WC : 2
sequence r0-cch = CW : 2
strand r0-a = ro-toe-sa r0-am...
structure [1nt] r0-Gate = r0-gate_base + r0-out
  r0-backward : .......(((((((((((((((((((((((((
```

mycrn.mfe
```
0:r0-B
CTTCATTTTTAACCTCAATATCACTCTTT 0. 0. 0
.............................
.............................
1:r0-Out
CCAAACTCTACCACACTTCATTTTTAACCTCAATATC 0. 0. 0
.....................................
.....................................
2:r0-Gate
AAAGAGTGATATTGAGGTTAAAAATGAAGTG+
  CCAAACTCTACCACACTTCATTTTTAACCTCAATATC 0. 0. 0
.......((((((((((((((((((((((((+
  ..............))))))))))))))))))))))))
.......((((((((((((((((((((((((+
  ..............))))))))))))))))))))))))
```

```
TopStrandList = list(
  'r0-A',
  'r0-B',
  'r0-Out',
  'r0-Back'

BaseStrands = list(
  'r0-toe-fa*',
  'r0-toe-fb*',

BMDomainList = list(
  'r0-bm',
  'r0-am',

TSToeholdDict = dictionary(
  'r0-A': [0,1,2,3,45,46,47
  'r0-B': [0,1,2,3,45,46,47

NoInteractionDict = dictionary(
  'r0-toe-fa' : list('r1-Back',
                     'p2-Flux','
```

```
TSI Avg    TSI Max    TO avg    TO max   BM Score
0.08       0.011      20.88     6.33     8
```

mycrn_scores.csv
```
set   TSI Avg   TSI Max   TO avg   TO max   BM Score
0     0.09      0.012     18.53    7.33     8
1     0.08      0.011     20.88    6.33     8
2     0.05      0.021     21.08    7.84     8
3     0.05      0.021     18.99    7.32     6
4     0.05      0.021     24.06    7.48     6
5     0.05      0.021     20.64    7.11     7
6     0.05      0.021     19.78    6.98     5
```

mycrn6.seqs
```
# Candidate 6
sequence r0-A CAATTCTACCATACTTTA
sequence r0-B CTAACCTTAATCTCCTC
sequence r0-Out CTCAAACCAATCCCAA
```

mycrn_scorereport.txt
```
Best sum-of-ranks:                          69.00 by [6]
Best sum-of-weighted-ranks:                  6.43 by [7]
Best fractional excess sum:                157.99 by [6]
Best weighted fractional excess sum:         9.18 by [6]
Best percent badness sum:                  707.94 by [6]
```

Figure S34: **Overview of the Piperine sequence design pipeline.** Mauve boxes show example input and output text files for each stage of the compilation pipeline in an example run of the software. Blue boxes illustrate internal data structures. Bold statements describe operations performed on data and standard-case statements explain the contents of that data. Sawtooth breaks in text bubbles indicate that a portion of that data or text is hidden for display purposes.

## S7.1 Translating an abstract CRN into domain-level specification of DNA strands and complexes

Piperine translates component reactions into the strand displacement architecture shown in Fig. 1DE, so it may only design sequences for CRNs whose component reactions have at most two reactants and two products. For formal reactions with less than two input or output strands, Piperine adds placeholders so that the final reaction has two reactants and two products. These placeholder strands have the same domain structure as signal strands, but they do not represent formal species of the CRN. They interact with only one complex in the strand displacement cascade; either they are sequestered by a React complex or released by a Produce complex. Following these rules, the DNA implementation is composed entirely of bimolecular reactions that follow the form shown in Fig. 1E of the main text. This mapping of abstract reactions to DNA strand displacement cascades, together with the design principles shown in Fig. 3 of the main text, constitute the domain-level specification for the DNA system in combination with key sequence-level constraints.

Piperine employs a strand displacement reaction paradigm that allows for independent tuning of individual reaction's kinetic rates. Rather than exploiting differences in toehold binding energies to tune rate constants, Piperine balances the binding energies of all toeholds in all kinetically relevant contexts (Fig. S36). Of particular importance is the reversible toehold-exchange reaction that controls Backward strand release in the react step. This is the rate-determining reaction step for the overall bimolecular architecture; all other rate dependence is a function of species concentrations (43). When toehold energies are balanced, the expected rate constant of a bimolecular reaction will be proportional to the concentrations of its respective fuel complexes. Furthermore, each rate may be tuned independently as the fuel complexes are unique to each reaction.

## S7.2 Generating candidate sequence designs from domain-level specifications

Piperine applies a CRN-to-DNA translation scheme, shown in Fig. S35, that is nearly identical to that described in Fig. 1DE and Fig. 3 of the main text. Piperine constrains all signal strands to have only A, C, or T nucleotides (ambiguity code H) in order to reduce secondary structure in the single-stranded species. Clamp domains are located at the $3'$ ends of branch migration domains to prevent fraying helix ends. All history domains are clamped by the nucleotide pair CW and all branch migration domains are closed by WC[2]. With these sequence features, Piperine guarantees a strong base-pair stack near the ends of helices, avoids strong remote toeholds, and prevents incessant base-pair exchange at nicks with tails as in the pathological case shown by Fig. S24. Furthermore, the $5'$-most nucleotides of history domains and second toeholds are fixed to be C's, and the internal toehold contexts in React complexes are truncated by a single base-pair. These nucleotide prescriptions enforce flanking C's at both the external and internal contexts of the React complex where first toeholds bind as shown in Fig. S36, thus making it easier to balance effective toehold binding energies as described below[3].

The toehold binding energies in the reversible portion of the react step must be balanced between

---

[2] In Design 5, all candidates' clamp domains were constrained to be CA and TC for history and branch migration domains respectively.

[3] Design 5 candidate sequences were not constrained to have second toeholds with $5'$ C bases. Rather, StickyDesign created one pool of sequences for each candidate and intelligently sorted them among first and second toeholds such that the worst-case energy imbalance between the internal and external binding contexts on a React complex was minimized. As it happened, the final chosen Design 5 sequence had $5'$ C's on all second toeholds, anyway.

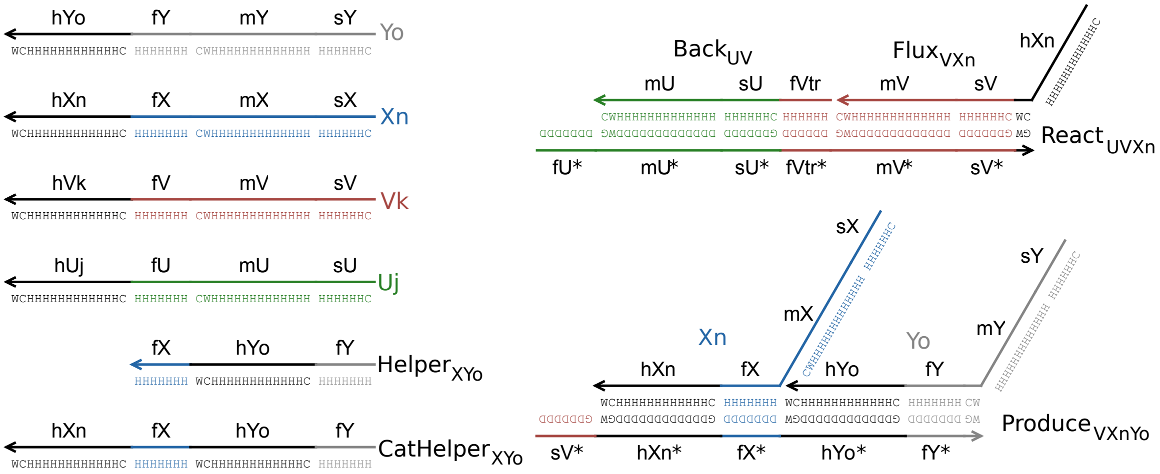

Figure S35: **Domain-level templates for bimolecular reactions used by Piperine.** Following the naming convention and color scheme introduced in Fig. 1E in the main text, this figure additionally lists the nucleotides or IUPAC nucleotide ambiguity codes that constrain the identity at each position of each domain. These DNA strands and complexes participate in the same network of strand displacement reactions as depicted in Fig. 1E as well. The nucleotide constraints for distinct domains are separated by short spaces. Shown in this figure, but not in Fig. 1E, is $f_{\mathrm{Vtr}}$ the truncated toehold domain in the backwards strand that binds to the internal toehold of the React complex. Also shown here, but not in Fig. 1E, are the 2-nucleotide clamps on the output side of the React and Produce complexes.

all bimolecular reactions. Otherwise, the rates of each react step may differ substantially between each bimolecular reaction. (Fig. S26 shows how changing the binding energy of the internal toehold context dramatically impacts the kinetics of the react step.) To achieve this, Piperine first generates orthogonal toehold sequences that are isoenergetic for both internal and external contexts of this reversible strand exchange reaction (Fig. S36) and assigns them to first toehold domains. Then, the compiler generates sequences with fixed $5'$ C nucleotides to define the second toehold domains in a manner that minimizes off-target interactions among all toeholds.

The software that generates toehold sequences for Piperine, Constantine Evans' StickyDesign, performs a fast, stochastic search through sequence space to find a set of sequences that describe balanced, orthogonal, and strong toehold binding contexts (55). For example, StickyDesign reduces crosstalk in the set of toeholds and toehold complements by ensuring that undesired and misaligned toehold binding events have low energy. Piperine ensures similar rate constants for all react steps by generating sequences for first toehold domains that are within a user-defined range of binding energies, as calculated by StickyDesign using thermodynamic parameters from refs. (27) and (36). In doing so, StickyDesign considers both contexts shown in Fig. S36 and takes the value furthest from the user-specified target energy as that toehold's binding energy. Designing against the worst-case values ensures that both critical toehold contexts fall in the desired range of binding energies for react steps, and that other toeholds and contexts are not too far off.

Piperine generates sequences for branch migration domains through sequence symmetry minimization after setting toehold sequences. This allows the compiler to create a set of energetically balanced toeholds and ensures that the sequence symmetry minimization routine will design against spurious toehold-binding sequences appearing in the other domains. As described above, Piperine translates each formal reaction to a domain-level representation of a bimolecular strand displace-

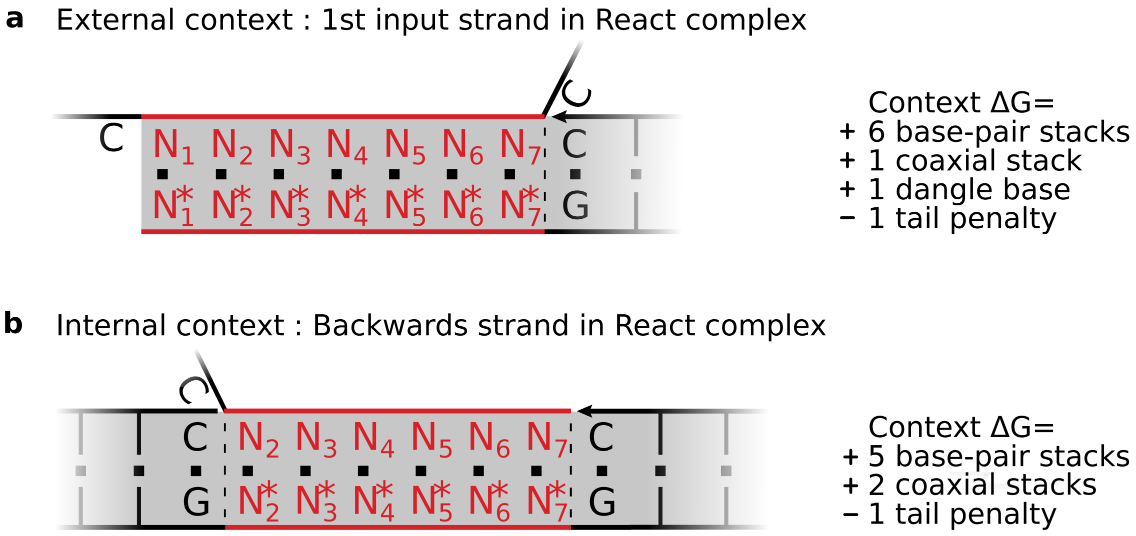

Figure S36: **Energetics accounting for the two toehold binding contexts that comprise the reversible toehold-exchange reaction of the react step.** The expected binding energy of a toehold depends on the characteristics and identities of its flanking nucleotides, not only its own nucleotide composition. Subfigures **a** and **b** show the binding contexts and energetic features of the two toehold-binding events that significantly impact a bimolecular reaction's overall kinetic rate. The indexed $\mathbf{N}_i$ characters represent the seven nucleotide bases, and asterisked characters their complements, that compose a toehold. The internal context uses a shorter toehold (lacking base $\mathbf{N}_1$) because a flanking coaxial stack and a base-pair similarly stabilize the bound toehold. The contexts shown in this figure applies to all React complexes in Design 5, though not to all React complexes of the Design 5 candidates. Some candidates had a base other than a C on the $3'$ flank of the internal context. See footnote 3.

ment cascade. Piperine then passes the domain-level specification, including the position-specific nucleotide constraints and toehold sequences, to SpuriousSSM, a sequence symmetry minimizer. SpuriousSSM stochastically produces DNA sequences satisfying the domain-level constraints, then iteratively edits undesirable sequence motifs and unintended subsequence matches until the occurrence of these features reaches a local minimum. Because this process is stochastic, SpuriousSSM produces different sequences for repeated executions with identical arguments. Piperine takes advantage of this to produce multiple candidate sequence designs for the system (29).

### S7.3 Selecting a winning candidate

Piperine applies the same heuristics described in Sections S4.3 and S4.6, with a few notable differences. First, Piperine's "NUPACK interaction score" assumes 0.5 M $\text{Na}^+$ rather than 50 mM $\text{Na}^+$ and 12.5 mM $\text{Mg}^{++}$. For this reason, the TSI, TO, and SSU scores for Designs 1 and 2 calculated by Piperine and listed in Table S9 are not identical to those listed in Table S5 or described in Section S4.2. Second, the set of strands used by the WSIS and WSIS-M heuristics includes catalytic Helper strands and does not include multiple copies of the distinct signal strands. However, for technical reasons not discussed here, the set does include signal strands lacking history domains. Each bimolecular reaction contributes the following strands, named according to Fig. 1E of the main text, to the set:

$$\begin{aligned}\{\mathrm{Reaction}_{\mathrm{UVXnYo}}\} = \{&\mathrm{U}_{\text{no history domain}}, \mathrm{V}_{\text{no history domain}}, \mathrm{Xn}, \mathrm{Yo}, \mathrm{Back}_{\mathrm{UV}}, \mathrm{Flux}_{\mathrm{VXn}} \\ &\mathrm{Helper}_{\mathrm{XYo}}, \mathrm{CatHelper}_{\mathrm{XnYo}}, \mathrm{ReactBot}_{\mathrm{UVXn}}, \mathrm{ProduceBot}_{\mathrm{VXnYo}}\}\end{aligned} \tag{22}$$

The heuristics are chiefly summations of a given metric over a set of strands or a set of strand groups. However, this approach may disguise the most egregious violations that significantly distort reaction dynamics on their own. Piperine determines both the average and most extreme value under each of the heuristics to capture both the overall and worst-case non-idealities.

In addition to these heuristic measures, Piperine considers scores based on Single-Strand Toehold Unpaired (SSTU), Bad Nucleotide Percent (BN%), Weighted-Sum Intra-Strand (WSAS), Verboten, and toehold energetics calculations. Based on the SSU heuristic, SSTU scoring involves finding the minimum unpaired probability for nucleotides within toehold regions and the first three bases to participate in strand displacement. This heuristic reflects the contribution of top strands' secondary structure to toehold occlusion. The SSTU score is calculated as below, where $T$ is the set of all strands designed to be free of secondary structure and $R$ is a function that maps a strand to its nucleotides composing the toehold and three initial strand-displacement positions.

$$\mathrm{SSTU} := \min_{S \,\in\, T} \left( \min_{b \,\in\, R(S)} \mathrm{p}_{\mathrm{unpaired}}(\mathrm{b}, \mathrm{S}) \right). \tag{23}$$

The BN% heuristic captures how well complexes form at equilibrium from 1 µM of each component strand. The two terms in the numerator account for structural and concentration defect which, when summed and divided by the target nucleotide concentration, gives the fraction of nucleotides expected to form incorrect base-pairing states. Structural defect refers to the nucleotides that form incorrect base-pairs within a complex. The expectation is for no less than 1 µM of perfect complexes, therefore any strands that do not participate in the target complex contribute incorrect nucleotides to the concentration defect.

The following definitions pertain to the equation below. $\phi_j$ is the sequence of complex $j$ and $s_j$ is its target base-pairing structure. $n(\phi_j, s_j)$ is NUPACK's estimate for the number of nucleotides in sequence $\phi_j$ that are not in the state prescribed by complex structure $s_j$, $x_j$ is the estimated concentration of complex $s_j$, and $y_j$ is its target concentration.

$$\mathrm{BN\%}(\phi_j, s_j) := \frac{n(\phi_j, s_j)\mathrm{min}(x_j, y_j) + |\phi_j|\mathrm{max}(y_j - x_j, 0)}{y_j|\phi_j|}$$

Piperine evaluates this measure over each complex, including waste and intermediate complexes, and counts as scores the maximum BN% value, the identity of the complex contributing the maximum value (for sequence debugging rather than scoring comparison purposes), and the mean value. We adopted this score to estimate each complexes' propensity to engage in leak pathways that are initiated through remote toeholds in malformed complexes and how far the designed complexes are from perfect complex formation generally.

Based on the WSIS (*I*nter-strand) scores described in Section S4.3, the WSAS score tallies spurious subsequence matches within strands (intr*A*-strand). The WSIS and WSAS heuristics both consider all DNA strands during their calculations. However, subsequence matches that are implied by design do not contribute to the score.

$$\text{WSAS} := \sum_{S_i} \left( \sum_{(s,s')\ \in \Phi(S_i)\times\Phi(S_i)} W_{lin}(s,s') \right), \tag{24}$$

Where $\Phi(S_i)$ once again is the multiset of all subsequences of $S_i$ and $W_{lin}$ is defined as

$$W_{lin}(s,s') := \begin{cases} 0 & \text{if } |s| < 6 \text{ or if } s \text{ does not match } s' \text{ or if } s \text{ is an intended match} \\ |s| - 5 & \text{if } |s| \in [6,12] \text{ and } s \text{ matches } s' \text{ unintentionally} \\ 7 & \text{if } |s| > 12 \text{ and } s \text{ matches } s' \text{ unintentionally.} \end{cases}$$

WSAS-M is calculated similarly, but requires a single mismatch between subsequences.

The Verboten heuristic measures the prevalence of specific subsequences that are expected to cause structural faults. We consider four distinct classes of verboten subsequences and employ weights in proportion to their severity as defined below. The verboten motifs are written in the IUPAC nucleotide ambiguity codes.

$$W_{verboten}(s) := \begin{cases} 1 & \text{if } s \in \{\text{WWWWWW, SWWWWW, WWWWWS, TTTT, AAAA}\} \\ 2 & \text{if } s \in \{\text{SSSSSS, SSSSSW, WSSSSS, GGG, CCC}\} \\ 1000 & \text{if } s \in \{\text{GGGG, CCCC}\} \\ 0.5 & \text{if } s \in \{\text{RRRRRR, YYYYYY, RYRYRY, YRYRYR,} \\ & \qquad \text{GCGC, GGCC, CCGG, CGCG}\} \\ 0 & \text{otherwise} \end{cases}$$

With this weighting, the Verboten heuristic calculates the weighted sum over the set of all subsequences of all strands, $\{S_i\}$.

$$\text{Verboten} := \sum_{S_i} \left( \sum_{s\ \in \Phi(S_i)} W_{verboten}(s) \right), \tag{25}$$

Piperine performs two measurements of toehold energetics imperfection, $\Delta G$ Error and $\Delta G$ Range. For the purpose of ranking designs relative to the target $\Delta G$ and the range of binding energies, Piperine calculates the $\Delta G$ of each first toehold (e.g. $\mathrm{f_A}$) in both React complex contexts shown in Fig. S36. The $\Delta G$ Error and $\Delta G$ Range scores are calculated from this list of binding energies. $\Delta G$ Error is the absolute difference between the mean toehold binding energy and the target binding energy. $\Delta G$ Range is the difference between the maximum and minimum binding energies. We used 7.7 kcal/mol as the target $\Delta G$ for toehold design. The second toehold sequences (e.g. $\mathrm{s_A}$) are not considered in these scores.

Our heuristic measures are intended to capture the tendency of a candidate design to misfold, to participate in leak reactions, or to exhibit reaction kinetics that are too fast or too slow. Although these heuristic measures were developed to identify and correct experimentally observed non-idealities, we do not have a model that relates heuristic scores to absolute levels of non-ideal behavior, nor one that combines the scores into a single performance metric. Therefore, to make comparisons between candidate designs that each perform well in some measures but not others, Piperine offers several methods for choosing a “winner” that does well relative to the other designs on most scores. In this work, we ask Piperine to calculate a rank for each candidate according to each heuristic measure, and then to select the candidate with the lowest sum-of-ranks as the winner.

## S8 Putting the design pipeline to the test

The design-experiment feedback approach to engineering an oscillating DNA strand displacement system demanded significant effort and time. To convince ourselves that the design principles used to generate that DNA system were sufficient, we attempted to design a second oscillating DNA system using only the principles described in the main paper and no design iterations. Furthermore, we formalized these design principles in a software package that automates the process of compiling abstract CRNs to DNA systems that emulate them, presented above in Section S7. This section describes the use of an early version of this compiler to generate a new set of DNA strands implementing the rock-paper-scissors formal reaction network and also summarizes its experimental characterization.

### S8.1 Generating and selecting candidates

We used a precursor of Piperine to generate and score ten candidate strand sets. For that reason, the scores used to guide our candidate selection and the scores presented in Table S8 are trivially different. The arguments and conclusions made here apply to either table of scores, such were the slight differences in scores. This precursor software was not automated, but otherwise had all features described in Section S7. These steps were performed as was done for Designs 1 through 4 with a single exception: we included the catalytic Helper in strand and complex definitions while designing this sequence set. This kind of strand was absent from the *in silico* domain templates while designing Designs 1-4. After generating ten candidates, we decided to select a promising candidate (#9 in Table S8) to improve by selective mutation of problematic nucleotides. While this design appeared favorable to others, we were concerned about balance in toehold availability. All candidates had large differences between the average and maximum values of SSTU scores, suggesting that kinetic bottlenecks caused by unintended base-pairing in toehold regions may disrupt the intended balance between all reaction pathways.

Using the precursor software to Piperine, we identified the nucleotides responsible for the SSTU Min values. Keeping all other nucleotides fixed, these positions were re-designed using SpuriousSSM to generate the “9-m” sequence set. The “mutation” improved the SSTU scores and the design ended up the best sum-of-ranks candidate, which we selected to be Design 5 and ordered for experiments. Critically, the selection by discussion and the directed alteration of winning candidate before purchasing were both manual operations. However, both were necessary to establish how an automated candidate selection should operate and to emphasize that heuristics allow one to detect and correct sequence defects before purchasing DNA.

Table S8: **Heuristic scores for sequence design candidates generated by Piperine.**

Legend: TSI: Top Strand Interactions; TO: Toehold Occlusion; WS-BM: Weighted Sum - Branch Migration; Max-BM: Length of largest subsequence match between BM domains; SSU: Single Strand Unpaired; SSTU: Single Strand Toehold Unpaired; BN%: Bad Nucleotide percent; WSIS: Weighted Sum - Inter-Strand; WSAS: Weighted Sum - Intra-Strand; $\Delta G$ Error: Absolute error between mean toehold binding energy and target toehold binding energy; $\Delta G$ Range: Maximum minus minimum toehold binding energies; ↑: Higher score is assigned lower rank; ↓: Lower score is assigned lower rank.

| **Design #** | **TSI avg ↓** | **TSI max ↓** | **TO avg ↓** | **TO max ↓** | **WS-BM ↓** | **Max-BM ↓** | **SSU min ↑** | **SSU avg ↑** | **SSTU min ↑** | **SSTU avg ↑** |
|---|---|---|---|---|---|---|---|---|---|---|
| 1 | 0.08 | 0.12 | 4.58 | 10.65 | 8 | 5 | 0.39 | 0.94 | 0.49 | 0.95 |
| 2 | 0.11 | 0.20 | 4.47 | 9.30 | 10 | 6 | 0.16 | 0.93 | 0.22 | 0.94 |
| 3 | 0.11 | 0.21 | 5.07 | 11.69 | 6 | 5 | 0.41 | 0.93 | 0.51 | 0.95 |
| 4 | 0.12 | 0.19 | 5.32 | 13.52 | 6 | 5 | 0.34 | 0.93 | 0.51 | 0.94 |
| 5 | 0.10 | 0.17 | 5.96 | 9.57 | 3 | 5 | 0.32 | 0.95 | 0.32 | 0.95 |
| 6 | 0.14 | 0.21 | 4.50 | 7.77 | 7 | 5 | 0.53 | 0.94 | 0.72 | 0.95 |
| 7 | 0.12 | 0.19 | 2.20 | 4.59 | 8 | 5 | 0.49 | 0.94 | 0.49 | 0.95 |
| 8 | 0.10 | 0.15 | 5.17 | 10.42 | 12 | 5 | 0.29 | 0.92 | 0.38 | 0.92 |
| 9 | 0.11 | 0.17 | 4.28 | 8.26 | 7 | 5 | 0.55 | 0.95 | 0.55 | 0.95 |
| 9-m | 0.08 | 0.12 | 6.06 | 13.18 | 14 | 6 | 0.60 | 0.96 | 0.60 | 0.95 |
| 10 | 0.08 | 0.16 | 7.66 | 24.28 | 9 | 6 | 0.33 | 0.94 | 0.33 | 0.92 |

| **Design candidate** | **BN% max ↓** | **BN% avg ↓** | **WSAS ↓** | **WSIS ↓** | **WSAS-M ↓** | **WSIS-M ↓** | **Verboten ↓** | **$\Delta G$ Error ↓** | **$\Delta G$ Range ↓** | **Rank sum** |
|---|---|---|---|---|---|---|---|---|---|---|
| 1 | 12.23 | 4.51 | 36 | 506 | 6 | 3143 | 24 910.5 | 0.07 | 0.42 | 79 |
| 2 | 7.48 | 3.92 | 36 | 521 | 0 | 3709 | 20 903.5 | 0.04 | 0.31 | 81 |
| 3 | 10.41 | 4.38 | 36 | 505 | 2 | 3940 | 910.5 | 0.04 | 0.31 | 76 |
| 4 | 11.92 | 4.65 | 58 | 1148 | 3 | 3941 | 20 962.5 | 0.04 | 0.11 | 104 |
| 5 | 6.64 | 3.66 | 59 | 410 | 12 | 4155 | 904.5 | 0.02 | 0.11 | 64 |
| 6 | 9.42 | 4.05 | 36 | 541 | 9 | 3981 | 940.0 | 0.05 | 0.72 | 67 |
| 7 | 11.23 | 4.14 | 37 | 627 | 1 | 2808 | 962.5 | 0.02 | 0.31 | 64 |
| 8 | 7.93 | 4.11 | 36 | 557 | 1 | 4113 | 931.0 | 0.03 | 0.16 | 84 |
| 9 | 10.09 | 4.14 | 36 | 538 | 9 | 3711 | 24 903.0 | 0.07 | 0.42 | 64 |
| 9-m | 6.79 | 3.57 | 39 | 561 | 1 | 5072 | 685.0 | 0.07 | 0.42 | 62 |
| 10 | 10.37 | 4.28 | 36 | 295 | 0 | 4552 | 901.5 | 0.03 | 0.15 | 82 |

Table S9: **Heuristic scores for sequence designs that were experimentally tested.**

Legend: TSI: Top Strand Interactions; TO: Toehold Occlusion; WS-BM: Weighted Sum - Branch Migration; Max-BM: Length of largest subsequence match between BM domains; SSU: Single Strand Unpaired; SSTU: Single Strand Toehold Unpaired; BN%: Bad Nucleotide percent; WSIS: Weighted Sum - Inter-Strand; WSAS: Weighted Sum - Intra-Strand; $\Delta G$ Error: Absolute error between mean toehold binding energy and target toehold binding energy; $\Delta G$ Range: Maximum minus minimum toehold binding energies; ↑: Higher score is assigned lower rank; ↓: Lower score is assigned lower rank.

| **Design #** | **TSI avg ↓** | **TSI max ↓** | **TO avg ↓** | **TO max ↓** | **WS-BM ↓** | **Max-BM ↓** | **SSU min ↑** | **SSU avg ↑** | **SSTU min ↑** | **SSTU avg ↑** |
|---|---|---|---|---|---|---|---|---|---|---|
| 1 | 0.05 | 0.07 | 43.78 | 82.45 | 18 | 6 | 0.56 | 0.96 | 0.57 | 0.95 |
| 2 | 0.57 | 1.24 | 2.92 | 6.03 | 10 | 6 | 0.19 | 0.89 | 0.19 | 0.86 |
| 3 | 0.71 | 1.35 | 2.34 | 3.94 | 10 | 6 | 0.12 | 0.89 | 0.12 | 0.87 |
| 4 | 0.20 | 0.38 | 3.24 | 5.95 | 11 | 6 | 0.65 | 0.96 | 0.65 | 0.95 |
| 5 | 0.08 | 0.12 | 6.06 | 13.18 | 14 | 6 | 0.60 | 0.96 | 0.60 | 0.95 |

| **Design #** | **BN% max ↓** | **BN% avg ↓** | **WSAS ↓** | **WSIS ↓** | **WSAS-M ↓** | **WSIS-M ↓** | **Verboten ↓** | **$\Delta G$ Error ↓** | **$\Delta G$ Range ↓** | **Rank sum** |
|---|---|---|---|---|---|---|---|---|---|---|
| 1 | 6.59 | 4.26 | 136 | 1632 | 9 | 7673 | 917.0 | 1.05 | 1.14 | 37 |
| 2 | 8.57 | 3.43 | 3 | 74 | 59 | 2646 | 839.5 | 0.46 | 1.92 | 36 |
| 3 | 9.34 | 3.43 | 3 | 74 | 59 | 2646 | 839.5 | 0.24 | 2.21 | 35 |
| 4 | 7.32 | 3.05 | 3 | 628 | 7 | 4579 | 899.5 | 0.46 | 2.39 | 26 |
| 5 | 6.79 | 3.57 | 39 | 561 | 1 | 5072 | 685.0 | 0.07 | 0.42 | 23 |

Table S9 lists the heuristic scores that Piperine calculated using the sequences from Designs 1 through 5. As Section S4 describes, we evolved the content and length constraints for specific DNA domains in each iteration. Each design, therefore, required a different set of rules to translate general CRNs into domain-level specifications. We built Piperine to provide modular support of translation schemes, which allowed us to separately codify the different translation rules while applying the same downstream heuristic scoring processes. The iteration-specific translation code differs slightly from that used during the original design process, and as a result the scores are not identical to those presented in Table S5.

† This increase in $\Delta G$ Range between Designs 3 and 4 disguises the fact that, as explained in Section S4.6, we truncated the internal toehold of just one of the React complexes in order to improve the balance of that complex's critical toehold contexts. This $\Delta G$ range is the difference in binding energies of the other React complexes' full-length internal toeholds and the truncated internal toehold.

## S8.2 Quantifying leak for Design 5

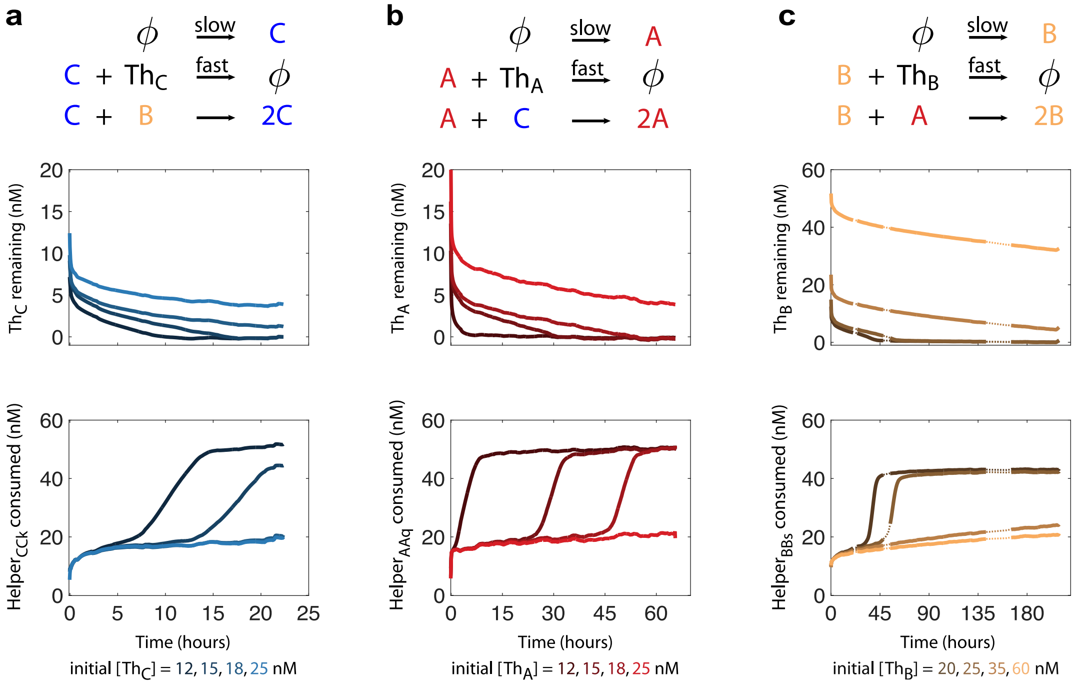

Figure S37: **Experimental characterization of autocatalytic modules (Design 5).** Columns **a**, **b**, **c** show data from experiments on three different DNA implementations of an autocatalytic reaction. At the top of each column is a formal CRN composed of, in descending order, the gradual leak, thresholding, and the formal autocatalytic reaction being implemented. The first row of plots show concentrations of Threshold complexes. Threshold complexes sequester the autocatalyst, delaying the onset of the exponential phase. Higher initial concentrations of Threshold, then, cause longer delays. The second row shows the consumption of Helper strands. Initial concentrations of Helper, Produce, and React species are all 100 nM, while the second input is 50 nM. Thus, ideal and leakless reactions would terminate with Helper completion at 50 nM. Missing data were replaced through linearly interpolation before smoothing and are represented by dotted line segments in the plots.

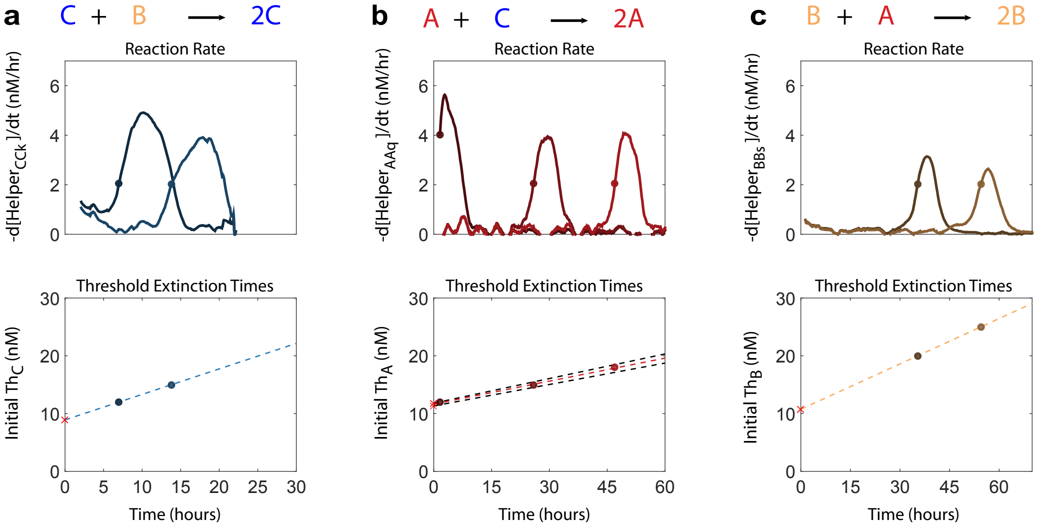

Figure S38: **Leak estimation from Design 5 autocatalyst reactions.** (**a-c**) For each of the three autocatalytic modules, the top plot shows the derivative of the corresponding data in Fig. S37, for those traces that exhausted the Thresholds. The bottom plot relates the time to initiate exponential phase, to the amount of Threshold added. The analysis performed here is identical to that described in the caption of Fig. S18, except that the Helper consumption rate level chosen to indicate the moment when Threshold complexes have been exhausted (dots) is 2 nM/hr instead of 1 nM/hr. This adjustment was made because, as discussed in Section S8.3, the Design 5 data were much noisier than previous experiments.

| Module | Initial leak (nM) | Gradual leak velocity (nM/hr) | Gradual leak rate constant (/M/s) |
|---|---|---|---|
| B + A → 2 B | 10.74 | 0.26 | 7.22 |
| C + B → 2 C | 8.91 | 0.44 | 12.22 |
| A + C → 2 A | 11.64 | 0.13 | 3.61 |

Table S10: **Leak parameters derived from autocatalyst experiments using Design 5.**

## S8.3 A note on normalization

As described in Section S8.2, we characterize the leak pathways by investigating each reaction separately as autocatalytic reactions. There are two fluorescent species in these experiments: Helper strands and strands released from Threshold complexes. In analyzing data from experiments on the Designs 1-4, fluorescence readouts were normalized relative to their minimum and maximum values. Both the Helper and Threshold fluorescence timecourse data are monotonic, being either exclusively absorbed or released during an experiment. Maximum fluorescence, then, corresponds to the total concentration of a species added to a sample. Zero-concentration levels are set by adding fluorescence quenching molecules or by measuring pre-reaction, quenched fluorescence. However, the lamp noise during experiments on Design 5 set was worse than in the earlier experiments and in some cases maximum fluorescence levels were not recorded long enough to find an average accurate enough for Maximum-Minimum normalization.

A new normalization approach, called Post-Produce Normalization, was developed to compensate for the noisy data. This approach assumes that all experimental samples of an autocatalytic reaction experience the same amount of initial leak, as we observed in data from experiments on Design 4 (Section S4.6). We first normalize the data such that their traces overlap immediately following the addition of Produce complexes and overlap once again when all Helper fluorescence is quenched. Then, we assign a concentration of 0 nM to each samples' minimum value before uniformly scaling their maximum values such that the average of all concentration data before the addition of Produces complexes is 100 nM. See Fig. S39 for a side-by-side comparison of Post-Produce and Maximum-Minimum Normalization.

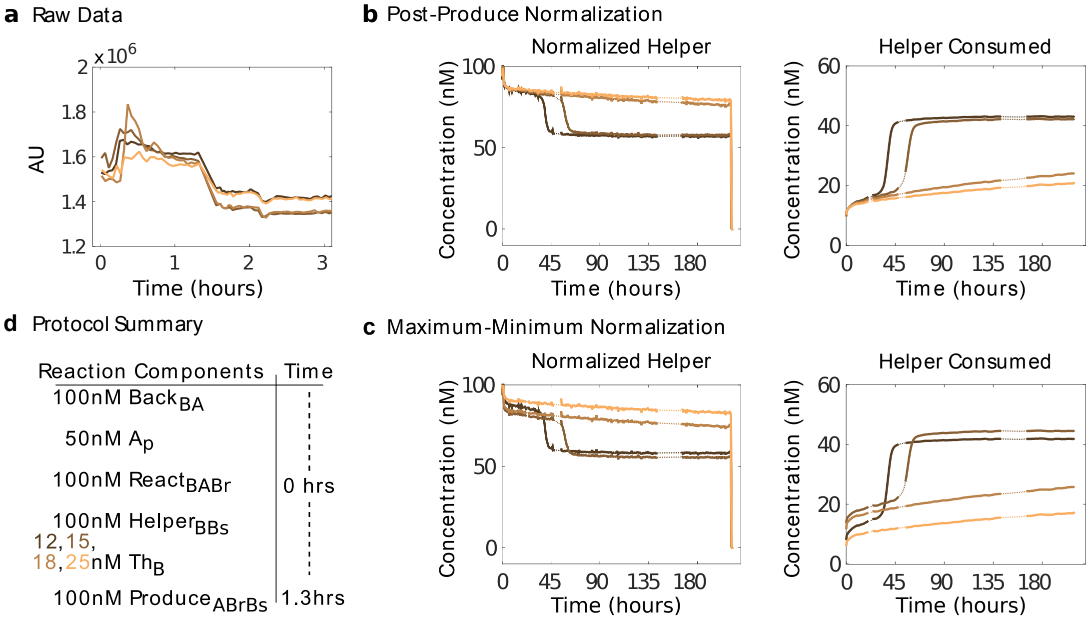

Figure S39: **A comparison of the two normalization methods using module B + A → 2 B from Design 5 as an example.** Panel **a** shows the raw fluorescence data from the four samples with initial conditions shown in panel **d**. Panel **a** presents only the first few hours of data to highlight lamp noise. Panels **b** and **c** show the results from using Post-Produce or Maximum-Minimum normalization methods, respectively.

### S8.4 Oscillator experiments using Design 5

Data from every experiment of the Design 5 Displacillator showed oscillatory behavior, validating Piperine as a tool for sequence design of dynamical strand displacement cascades. For all six experimentally tested initial conditions (Fig. S40), plots of the rate of Helper consumption (Fig. S41) show that the reaction produces signal strands in the same $\mathrm{A} \rightarrow \mathrm{B} \rightarrow \mathrm{C}$ cycle as the formal CRN. However, the significant variation between initial conditions of the different Design 5 oscillator experiments produced a diverse set of trajectories that, in some cases, contradict the expected trajectory. In each sample, we aimed to establish an initial condition with two signal strands at high concentration and one signal strand at low concentration such that only one individual autocatalytic reaction would be active at the onset of the reaction. Where samples **a,b,d,e,f** are those where the fastest initial reaction is clear in Fig. S41, **b,d,f** are in agreement with expectations based on the initial conditions. This indicates that the approaches we took to set an initial condition for the Displacillator reaction were inaccurate, especially for initial conditions with low signal concentrations.

Theoretically, the initial species concentrations of a formal CRN determine its trajectory through phase space. In the DNA dynamical systems considered here, a reaction's initial condition is set by two experimenter-controlled parameters (the concentrations of Threshold complexes and signal strands added to the test tube) and one uncontrollable parameter (concentrations of signal strands released through leak reactions). Using the estimates of initial and gradual leak derived from the autocatalyst experiments described in Section S8.2, we attempt to account for leak by first including threshold complexes at concentrations greater than the estimated leak contribution and then adding signal strands to simultaneously trigger the remaining threshold complexes and kickstart oscillations at a known, non-zero initial condition. Fig. S40 explains these calculations for the six rock-paper-scissors oscillator experiments performed using Design 5. Unless specified, experimental parameters are identical to those described in the main text. The results corresponding to the experimental parameters in Fig. S40 are shown in Fig. S41.

a Initial: (Ap,Br,Cj) = (8.8, 7, 2.7)nM

| | A | B | C |
|---|---|---|---|
| Threshold added (nM) | 13 | 16 | 12 |
| Signal leaked (nM) | 10.8 | 13 | 11.7 |
| Signal added (nM) | 11 | 10 | 3 |

b Initial: (Ap,Br,Cj) = (-0.3, 10, 13)nM

| | A | B | C |
|---|---|---|---|
| Threshold added (nM) | 13 | 16 | 12 |
| Signal leaked (nM) | 12.7 | 16 | 12 |
| Signal added (nM) | 0 | 10 | 13 |

c Initial: (Ap,Br,Cj) = (3.4, 2, -3.7)nM

| | A | B | C |
|---|---|---|---|
| Threshold added (nM) | 13 | 16 | 12 |
| Signal leaked (nM) | 3.4 | 5 | 5.3 |
| Signal added (nM) | 13 | 13 | 3 |

d Initial: (Ap,Br,Cj) = (3.7,-7.9, 6.9)nM

| | A | B | C |
|---|---|---|---|
| Threshold added (nM) | 13 | 16 | 12 |
| Signal leaked (nM) | 3.7 | 5.1 | 5.9 |
| Signal added (nM) | 13 | 3 | 13 |

e Initial: (Ap,Br,Cj) = (-0.3, 3.8, 5.4)nM

| | A | B | C |
|---|---|---|---|
| Threshold added (nM) | 10 | 10 | 10 |
| Signal leaked (nM) | 3.7 | 3.8 | 5.4 |
| Signal added (nM) | 6 | 10 | 10 |

f Initial: (Ap,Br,Cj) = (3.7,-0.1, 5.7)nM

| | A | B | C |
|---|---|---|---|
| Threshold added (nM) | 10 | 10 | 10 |
| Signal leaked (nM) | 3.7 | 3.9 | 5.7 |
| Signal added (nM) | 10 | 6 | 10 |

Figure S40: **Initial conditions for six trials of Design 5.** Tables **a**-**f** list the experimental values that determined the initial signal strand concentrations for each execution of the full Design 5 oscillator shown in Fig. S41, respecting figure labels. “Threshold added” values are the concentrations of each signal’s threshold complex prior to the addition to Produce complexes. Following the manual addition of Produce complexes, both initial and gradual leak pathways are active and introduce signal strands that react with Threshold complexes. “Signal leaked” values are the concentrations of reacted threshold complexes, measured directly through their fluorescent output strands, at the moment before the manual addition of signal strands. “Signal added” values are the concentration of each signal strand manually added to the reaction, intended to exhaust all remaining threshold complexes and set the initial condition of the chemical oscillations. The initial species concentrations, then, are the sum of leaked and added signal strand conentrations minus the initial threshold concentrations, where negative values indicate surplus threshold complexes. Experiment pairs **a** & **b**, **c** & **d**, and **e** & **f** were each prepared and executed simultaneously and each pair was executed on different days. The experimental chronology matches the alphabetical order of the labels used.

For the first four experiments (**a-d** of Fig. S40 and Fig. S41), threshold complexes were added to the preliminary reaction mixtures at concentrations higher than those expected from the initial and gradual leaks stemming from the individual autocatalytic reactions. While the first experiments conducted (pair **a-b**) exhibited initial leaks as expected, leak dropped significantly in the following experimental pair **c-d**. Most likely this is due to faster preparation of the later experiment pairs and thus less gradual leak accumulation ahead of the first fluorescence readings. Overestimation of leak in experimental pair **c-d** lead to a large surplus of threshold complexes after manual addition of signal strands and, as a result, a long delay before onset of oscillatory behavior in both experimental samples.

Having observed that initial leak estimates based on individual autocatalytic experiments may not predict initial leaks in the rock-paper-scissors reactions, the concentrations of signal strands added to experimental samples **e-f** were adjusted as data were collected, rather than set prior to the experiment, in order to more accurately establish the desired initial signal strand concentrations. From the raw threshold fluoresence data we estimated the concentration of leaked signal strands, observing whether the leak appeared more similar to samples **a-b** or **c-d**, and then tuned the concentration of added signal strands accordingly. This approach allowed us to reduce surplus threshold concentrations in experimental pair **e-f**.

Unlike Design 4, we did not determine the overall kinetic rates and yield of each autocatalytic reaction component of Design 5. Therefore these data are not amenable to the same comparisons to model simulations. There are, however, trends that stand out. The observed peak order matches that of the theoretical system, $\mathrm{A} \rightarrow \mathrm{B} \rightarrow \mathrm{C} \rightarrow \mathrm{A}$. Larger initial concentrations yield higher reaction velocities (e.g. **b** compared to **a**). Helper consumption appears to accelerate throughout all trials except **b**. This may indicate that concentration of catalytic Helper strands used in these experiments had adjusted the stoichiometry of the autocatalytic reactions above the intended ratio of two output strands for two input strands and lead to a net increase, rather than conservation, of total signal strand concentration in solution as the experiment progressed.

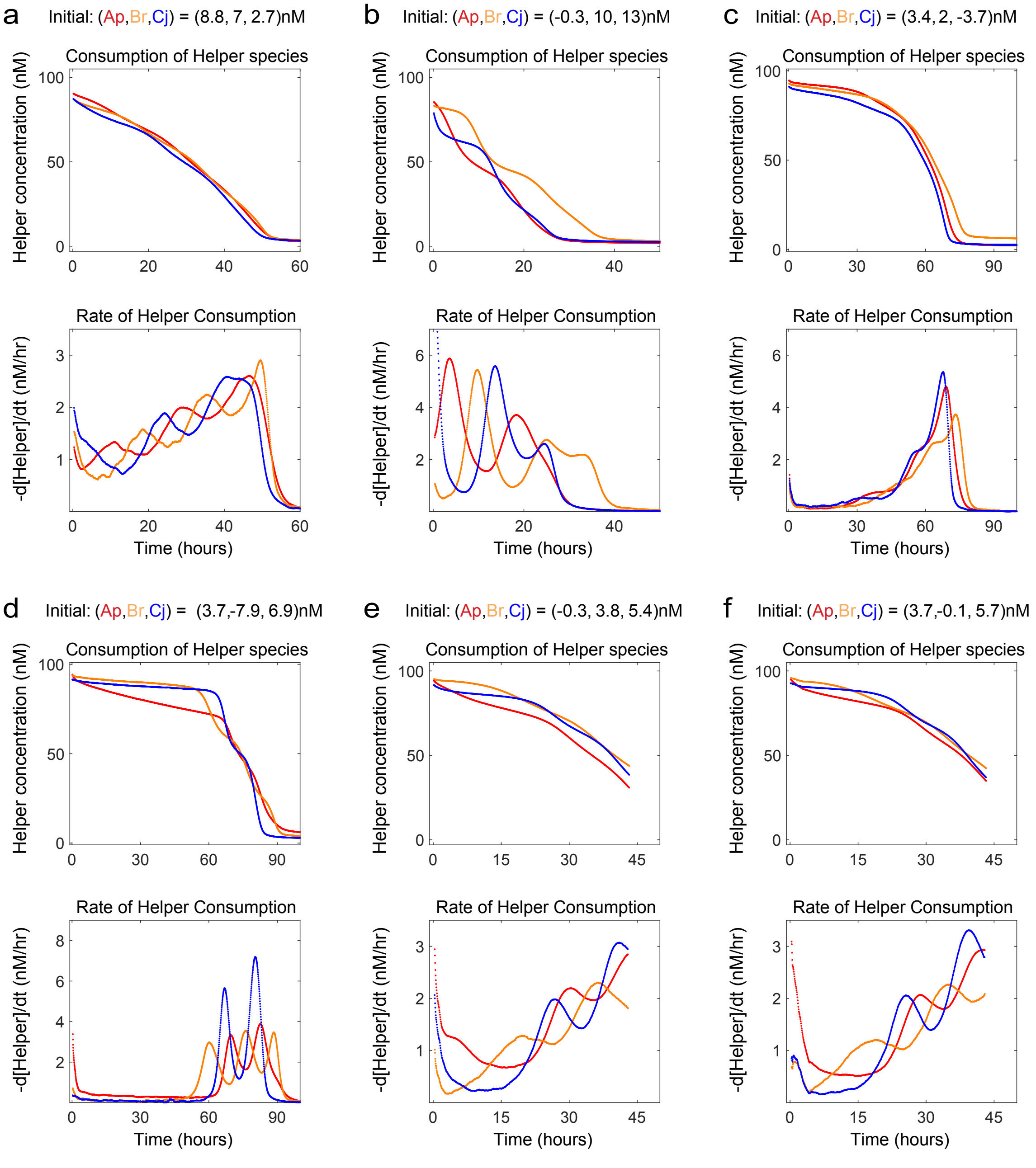

Figure S41: **Experimental results for six different runs of the Design 5 Displacillator.** (**a-f**) Plots of Helper concentrations and consumption rates along with initial signal strand concentrations. Fig. S40 shows the calculations that yield the initial conditions listed here. Negative values occur when there are expected to be surplus Threshold complexes in solution at time $t = 0$.

# S9 Sequences and molecules for Designs 1, 2, 3, 4, and 5

## S9.1 DNA sequences for Designs 1-5

DNA sequences used in this study are provided below. All sequences are written from $5'$ to $3'$.

| Strand name | Sequence |
|---|---|
| D1_React_BOT_CBCj | AGTGGGTTAGTAGAGAGTTGTTAGTGGGAAATGGGAATGTTGTGAGGAATGAGAGGGTAT |
| D1_Back_CB | CTCATTCCTCACAACATTCCCATTTCCCA |
| D1_Flux_BCj | CTAACAACTCTCTACTAACCCACTTCATACCTTATCC |
| D1_Produce_BOT_BCjCk | AGAGGGTATGAAGGTGTAAGAAGGAGGGTATGGATAAGGTATGAAGTGGGTTA |
| D1_Cj | CTTCATACCTTATCCATACCCTCTCATTCCTCACAACATTCCCA |
| D1_Ck | CCTTCTTACACCTTCATACCCTCTCATTCCTCACAACATTCCCA |
| D1_Helper_CCk | ATACCCTCCTTCTTACACCTTCATACCCT |
| D1_React_BOT_BABr | TGAGGGTTAGAGGTTTGAAGAGTGAGGGATTTGGGTTAGTAGAGAGTTGTTAGTGGGAAA |
| D1_Back_BA | CTAACAACTCTCTACTAACCCAAATCCCT |
| D1_Flux_ABr | CACTCTTCAAACCTCTAACCCTCATTCAAATCTCACC |
| D1_Produce_BOT_ABrBs | AGTGGGAAAGGAGAGAATGAATGGTGGGAAAGGTGAGATTTGAATGAGGGTTA |
| D1_Br | CATTCAAATCTCACCTTTCCCACTAACAACTCTCTACTAACCCA |
| D1_Bs | CCATTCATTCTCTCCTTTCCCACTAACAACTCTCTACTAACCCA |
| D1_Helper_BBs | TTTCCCACCATTCATTCTCTCCTTTCCCA |
| D1_React_BOT_ACAp | TGTGGGAATGTTGTGAGGAATGAGAGGGTATAGGGTTAGAGGTTTGAAGAGTGAGGGATT |
| D1_Back_AC | CACTCTTCAAACCTCTAACCCTATACCCT |
| D1_Flux_CAp | CTCATTCCTCACAACATTCCCACACAATACTATCATC |
| D1_Produce_BOT_CApAq | TGAGGGATTGTGTTTGAGTTTAGGAGGGATTGATGATAGTATTGTGTGGGAAT |
| D1_Ap | CACAATACTATCATCAATCCCTCACTCTTCAAACCTCTAACCCT |
| D1_Aq | CCTAAACTCAAACACAATCCCTCACTCTTCAAACCTCTAACCCT |
| D1_Helper_AAq | AATCCCTCCTAAACTCAAACACAATCCCT |

Table S11: **DNA sequences from Design 1.**

| Strand name | Sequence |
|---|---|
| D2_React_BOT_CBCj | TCGGGTAAAGAGATTGATTGGTGGGATATGGAGAAATGAGGAAGTTGAGAGGCTTGTTGT |
| D2_Back_CB | GCCTCTCAACTTCCTCATTTCTCCATATC |
| D2_Flux_BCj | CCACCAATCAATCTCTTTACCCGACACCTCCCTTCTA |
| D2_Produce_BOT_BCjCk | GCTTGTTGTAGGAGTGTGTTTGCGTTGTTGTTAGAAGGGAGGTGTCGGGTAAA |
| D2_Cj | GACACCTCCCTTCTAACAACAAGCCTCTCAACTTCCTCATTTCT |
| D2_Ck | CGCAAACACACTCCTACAACAAGCCTCTCAACTTCCTCATTTCT |
| D2_Helper_CCk | ACAACAACGCAAACACACTCCTACAACAA |
| D2_React_BOT_BABr | CCGTAGTGATAGTTAGTATGTACCAAAGGATGGGTAAAGAGATTGATTGGTGGGATATGG |
| D2_Back_BA | CCACCAATCAATCTCTTTACCCATCCTTT |
| D2_Flux_ABr | GGTACATACTAACTATCACTACGGCATTACATTCAAA |
| D2_Produce_BOT_ABrBs | GGGATATGGGAAGAATAGGTTGCCGATATGGTTTGAATGTAATGCCGTAGTGA |
| D2_Br | GGCATTACATTCAAACCATATCCCACCAATCAATCTCTTTACCC |
| D2_Bs | GGCAACCTATTCTTCCCATATCCCACCAATCAATCTCTTTACCC |
| D2_Helper_BBs | CCATATCGGCAACCTATTCTTCCCATATC |
| D2_React_BOT_ACAp | CCAGAAATGAGGAAGTTGAGAGGCTTGTTGTGTAGTGATAGTTAGTATGTACCAAAGGAT |
| D2_Back_AC | GGTACATACTAACTATCACTACACAACAA |
| D2_Flux_CAp | GCCTCTCAACTTCCTCATTTCTGGTCACCACACTTCT |
| D2_Produce_BOT_CApAq | CCAAAGGATTAGGGTTAGTTGTGGAAAGGATAGAAGTGTGGTGACCAGAAATG |
| D2_Ap | GGTCACCACACTTCTATCCTTTGGTACATACTAACTATCACTAC |
| D2_Aq | CCACAACTAACCCTAATCCTTTGGTACATACTAACTATCACTAC |
| D2_Helper_AAq | ATCCTTTCCACAACTAACCCTAATCCTTT |

Table S12: **DNA sequences from Design 2.**

| Strand name | Sequence |
|---|---|
| D3_React_BOT_CBCj | TGTTGTTCGGAGAGTTGAAGGAGTAAAGAGGTATAGGGTGGTTAGTTAGAGAAATGGGCT |
| D3_Back_CB | CTATACCTCTTTACTCCTTCAACTCTCCG |
| D3_Flux_BCj | ATCTTCCCTCCACAGCCCATTTCTCTAACTAACCACC |
| D3_Produce_BOT_BCjCk | AAATGGGCTGTGGAGGGAAGATTGTTGTTGCGTTTGTGTGAGGATGTTGTTCG |
| D3_Cj | TCTTTACTCCTTCAACTCTCCGAACAACAATCTTCCCTCCACAG |
| D3_Ck | TCTTTACTCCTTCAACTCTCCGAACAACATCCTCACACAAACGC |
| D3_Helper_CCk | AACAACATCCTCACACAAACGCAACAACA |
| D3_React_BOT_BABr | GGTATAGGGTGGTTAGTTAGAGAAATGGGTAGGAAACCATGTATGATTGATAGTGATGCC |
| D3_Back_BA | TTTCCTACCCATTTCTCTAACTAACCACC |
| D3_Flux_ABr | AAACTTACATTACGGCATCACTATCAATCATACATGG |
| D3_Produce_BOT_ABrBs | AGTGATGCCGTAATGTAAGTTTGGTATAGCCGTTGGATAAGAAGGGTATAGGG |
| D3_Br | CCCATTTCTCTAACTAACCACCCTATACCAAACTTACATTACGG |
| D3_Bs | CCCATTTCTCTAACTAACCACCCTATACCCTTCTTATCCAACGG |
| D3_Helper_BBs | CTATACCCTTCTTATCCAACGGCTATACC |
| D3_React_BOT_ACAp | TAGGAAACCATGTATGATTGATAGTGATGTGTTGTTCGGAGAGTTGAAGGAGTAAAGACC |
| D3_Back_AC | AACAACACATCACTATCAATCATACATGG |
| D3_Flux_CAp | TCTTCACACCACTGGTCTTTACTCCTTCAACTCTCCG |
| D3_Produce_BOT_CApAq | GTAAAGACCAGTGGTGTGAAGATAGGAAAGGTGTTGATTGGGATTAGGAAACC |
| D3_Ap | CATCACTATCAATCATACATGGTTTCCTATCTTCACACCACTGG |
| D3_Aq | CATCACTATCAATCATACATGGTTTCCTAATCCCAATCAACACC |
| D3_Helper_AAq | TTTCCTAATCCCAATCAACACCTTTCCTA |

Table S13: **DNA sequences from Design 3.**

| Strand name | Sequence |
|---|---|
| D4_React_BOT_CBCj | `TGTTGTTTGGAGAGTTGAAGGAGTAAAGAGGTATAGGGTGGTTAGTTAGAGAAATGGGCG` |
| D4_Back_CB | `CTATACCTCTTTACTCCTTCAACTCTCCA` |
| D4_Flux_BCj | `ATCTTCCCTCCACCGCCCATTTCTCTAACTAACCACC` |
| D4_Produce_BOT_BCjCk | `AAATGGGCGGTGGAGGGAAGATTGTTGTTGCGTTTGTGTGAGGATGTTGTTTG/3IAbRQSp/` |
| D4_Cj | `TCTTTACTCCTTCAACTCTCCAAACAACAATCTTCCCTCCACCG` |
| D4_Ck | `TCTTTACTCCTTCAACTCTCCAAACAACATCCTCACACAAACGC` |
| D4_Helper_CCk | `/56-ROXN/AACAACATCCTCACACAAACGCAACAACA` |
| D4_Cat_Helper_CCk | `/56-ROXN/AACAACATCCTCACACAAACGCAACAACAATCTTCCCTCCACCG` |
| D4_React_BOT_BABr | `GGTATAGGGTGGTTAGTTAGAGAAATGGGTAGGAAAAGATGTAGGATTGATAGTGATGCG` |
| D4_Back_BA | `TTTCCTACCCATTTCTCTAACTAACCACC` |
| D4_Flux_ABr | `AAACTTACATTACCGCATCACTATCAATCCTACATCT` |
| D4_Produce_BOT_ABrBs | `AGTGATGCGGTAATGTAAGTTTGGTATAGCGGTTGGATAAGAAGGGTATAGGG/3IAbRQSp/` |
| D4_Br | `CCCATTTCTCTAACTAACCACCCTATACCAAACTTACATTACCG` |
| D4_Bs | `CCCATTTCTCTAACTAACCACCCTATACCCTTCTTATCCAACCG` |
| D4_Helper_BBs | `/5Alex647N/CTATACCCTTCTTATCCAACCGCTATACC` |
| D4_Cat_Helper_BBs | `/5Alex647N/CTATACCCTTCTTATCCAACCGCTATACCAAACTTACATTACCG` |
| D4_React_BOT_ACApi2 | `TAGGAAAAGATGTAGGATTGATAGTGATGTTGTTTGGAGAGTTGAAGGAGTAAAGAAG` |
| D4_Back_ACi2 | `AACAACATCACTATCAATCCTACATCT` |
| D4_Flux_CAp | `TCTTCACACCACTCTTCTTTACTCCTTCAACTCTCCA` |
| D4_Produce_BOT_CApAq | `GTAAAGAAGAGTGGTGTGAAGATAGGAAAGGTGTTGATTGGGATTAGGAAAAG/3IABkFQ/` |
| D4_Ap | `CATCACTATCAATCCTACATCTTTTCCTATCTTCACACCACTCT` |
| D4_Aq | `CATCACTATCAATCCTACATCTTTTCCTAATCCCAATCAACACC` |
| D4_Helper_AAq | `/5Alex488N/TTTCCTAATCCCAATCAACACCTTTCCTA` |
| D4_Cat_Helper_AAq | `/5Alex488N/TTTCCTAATCCCAATCAACACCTTTCCTATCTTCACACCACTCT` |

Table S14: **DNA sequences from Design 4.**

| Strand name | Sequence |
|---|---|
| D4_Rep_BOT_C | `TGTTGTTTGGAGAGTTGAAGGAGTAAAGA/3AlexF488N/` |
| D4_Rep_TOP_B | `/5IAbRQ/CCCATTTCTCTAACTAACCACC` |
| D4_Rep_BOT_B | `GGTATAGGGTGGTTAGTTAGAGAAATGGG/3Rox_N/` |
| D4_Rep_TOP_A | `/5IAbRQ/CATCACTATCAATCCTACATCT` |
| D4_Rep_BOT_A | `TAGGAAAAGATGTAGGATTGATAGTGATG/3AlexF647N/` |
| D4_Helper_CCk† | `AACAACATCCTCACACAAACGCAACAACA` |
| D4_Cat_Helper_CCk† | `AACAACATCCTCACACAAACGCAACAACAATCTTCCCTCCACCG` |
| D4_Helper_BBs† | `CTATACCCTTCTTATCCAACCGCTATACC` |
| D4_Cat_Helper_BBs† | `CTATACCCTTCTTATCCAACCGCTATACCAAACTTACATTACCG` |
| D4_Helper_AAq† | `TTTCCTAATCCCAATCAACACCTTTCCTA` |
| D4_Cat_Helper_AAq | `TTTCCTAATCCCAATCAACACCTTTCCTATCTTCACACCACTCT` |
| D4_Rep_TOP_C† | `TCTTTACTCCTTCAACTCTCCA` |
| D4_Rep_BOT_C† | `TGTTGTTTGGAGAGTTGAAGGAGTAAAGA` |
| D4_Rep_TOP_B† | `CCCATTTCTCTAACTAACCACC` |
| D4_Rep_BOT_B† | `GGTATAGGGTGGTTAGTTAGAGAAATGGG` |
| D4_Rep_TOP_A† | `CATCACTATCAATCCTACATCT` |
| D4_Rep_BOT_A† | `TAGGAAAAGATGTAGGATTGATAGTGATG` |
| D4_Rep_TOP_C | `/5IABkFQ/TCTTTACTCCTTCAACTCTCCA` |
| D4_Que_Helper_CCk | `TGTTGTTGCGTTTGTGTGAGGATGTTGTTTG/3IAbRQSp/` |
| D4_Que_Helper_BBs | `GGTATAGCGGTTGGATAAGAAGGGTATAGGG/3IAbRQSp/` |
| D4_Que_Helper_AAq | `TAGGAAAGGTGTTGATTGGGATTAGGAAAAG/3IABkFQ/` |

Table S15: **Additional DNA sequences from Design 4.** † signifies "plain version", without fluorophores or quenchers attached. Complexes $\mathrm{RepA}$, $\mathrm{RepB}$ and $\mathrm{RepC}$, comprising the corresponding top and bottom strands, also act as Thresholds $\mathrm{Th}_\mathrm{A}$, $\mathrm{Th}_\mathrm{B}$, and $\mathrm{Th}_\mathrm{C}$.

| Strand name | Sequence |
|---|---|
| D4_Rep_Back_CB_Top | TCTTTACTCCTTCAACTCTCCA/3IAbRQSp/ |
| D4_Rep_Back_CB_Bot | /56-ROXN/TGGAGAGTTGAAGGAGTAAAGAGGTATAG |
| D4_Rep_Back_BA_Top | CCCATTTCTCTAACTAACCACC/3IAbRQSp/ |
| D4_Rep_Back_BA_Bot | /56-ROXN/GGTGGTTAGTTAGAGAAATGGGTAGGAAA |
| D4_Rep_Back_ACi2_Top | CATCACTATCAATCCTACATCT/3IAbRQSp/ |
| D4_Rep_Back_ACi2_Bot | /56-ROXN/AGATGTAGGATTGATAGTGATGTTGTT |
| D4_Rep_Flux_ABr_Top | /5IAbRQ/CAAACTTACATTACCG |
| D4_Rep_Flux_ABr_Bot | AGTGATGCGGTAATGTAAGTTTG/3Rox_N/ |
| D4_Rep_Flux_BCj_Top | /5IAbRQ/CATCTTCCCTCCACCG |
| D4_Rep_Flux_BCj_Bot | AAATGGGCGGTGGAGGGAAGATG/3Rox_N |
| D4_Rep_Flux_BCj_Top | /5IAbRQ/CATCTTCCCTCCACCG |
| D4_Rep_Flux_BCj_Bot | AAATGGGCGGTGGAGGGAAGATG/3Rox_N |
| D4_Rep_Flux_CAp_Top | /5IAbRQ/CTCTTCACACCACTCT |
| D4_Rep_Flux_CAp_Bot | GTAAAGAAGAGTGGTGTGAAGAG/3Rox_N |

Table S16: **DNA sequences used for characterizing individual rate constants in Design 4.**

| Strand name | Sequence |
|---|---|
| D5_Aq | CACATCATCCAACACCTTCCTCACTTCTCCATAACCAATCCACA |
| D5_Ap | CACATCATCCAACACCTTCCTCACTTCTCCTCTCTATACTTACA |
| D5_Br | CTTACCTTCATCCTCCACAATCTTCCATTCACCAACCTCAAACA |
| D5_Bs | CTTACCTTCATCCTCCACAATCTTCCATTCCTAACCATACTACA |
| D5_Cj | CTCAACATTTCCACTATCCTTCAACTCTTCCCTCCTACCACCCA |
| D5_Ck | CTCAACATTTCCACTATCCTTCAACTCTTCATATCTACTAAACA |
| D5_FLUX_ABr | CACCAACCTCAAACACACATCATCCAACACCTTCCTC |
| D5_FLUX_BCj | CCCTCCTACCACCCACTTACCTTCATCCTCCACAATC |
| D5_FLUX_CAp | CATAACCAATCCACACTCAACATTTCCACTATCCTTC |
| D5_BACK_BA | ACTTCTCTTACCTTCATCCTCCACAATC |
| D5_BACK_CB | TTCCATCTCAACATTTCCACTATCCTTC |
| D5_BACK_AC | AACTCTCACATCATCCAACACCTTCCTC |
| D5_REACT_BOT_BABr | AATGGAAGATTGTGGAGGATGAAGGTAAGAGAAGTGAGGAAGGTGTTGGATGATGTGTG |
| D5_REACT_BOT_CBCj | AAGAGTTGAAGGATAGTGGAAATGTTGAGATGGAAGATTGTGGAGGATGAAGGTAAGTG |
| D5_REACT_BOT_ACAp | GAGAAGTGAGGAAGGTGTTGGATGATGTGAGAGTTGAAGGATAGTGGAAATGTTGAGTG |
| D5_HELP_CAT_BBs† | TTCCATTCCTAACCATACTACATTCCATTCACCAACCTCAAACA |
| D5_HELP_CAT_CCk† | AACTCTTCATATCTACTAAACAAACTCTTCCCTCCTACCACCCA |
| D5_HELP_CAT_AAq† | ACTTCTCCTCTCTATACTTACAACTTCTCCATAACCAATCCACA |
| D5_HELP_BBs† | TTCCATTCCTAACCATACTACATTCCATT |
| D5_HELP_CCk† | AACTCTTCATATCTACTAAACAAACTCTT |
| D5_HELP_AAq† | ACTTCTCCTCTCTATACTTACAACTTCTC |
| D5_HELP_CAT_BBs | /5Alex647N/TTCCATTCCTAACCATACTACATTCCATTCACCAACCTCAAACA |
| D5_HELP_CAT_CCk | /56-ROXN/AACTCTTCATATCTACTAAACAAACTCTTCCCTCCTACCACCCA |
| D5_HELP_CAT_AAq | /5Alex488N/ACTTCTCCTCTCTATACTTACAACTTCTCCATAACCAATCCACA |
| D5_HELP_BBs | /5Alex647N/TTCCATTCCTAACCATACTACATTCCATT |
| D5_HELP_CCk | /56-ROXN/AACTCTTCATATCTACTAAACAAACTCTT |
| D5_HELP_AAq | /5Alex488N/ACTTCTCCTCTCTATACTTACAACTTCTC |
| D5_PROD_BOT_ABrBs | TGATGTGTGTTTGAGGTTGGTGAATGGAATGTAGTATGGTTAGGAATGGAAGA/3IAbRQSp/ |
| D5_PROD_BOT_BCjCk | AGGTAAGTGGGTGGTAGGAGGGAAGAGTTTGTTTAGTAGATATGAAGAGTTGA/3IAbRQSp/ |
| D5_PROD_BOT_CApAq | TGTTGAGTGTGGATTGGTTATGGAGAAGTTGTAAGTATAGAGAGGAGAAGTGA/3IABkFQ/ |
| D5_QUE_HELP_BBs | AATGGAATGTAGTATGGTTAGGAATGGAAGA/3IAbRQSp/ |
| D5_QUE_HELP_CCk | AAGAGTTTGTTTAGTAGATATGAAGAGTTGA/3IAbRQSp/ |
| D5_QUE_HELP_AAq | GAGAAGTTGTAAGTATAGAGAGGAGAAGTGA/3IABkFQ/ |
| D5_REP_A_TOP | /5IAbRQ/CACATCATCCAACACCTTCCTC |
| D5_REP_A_BOT | GAGAAGTGAGGAAGGTGTTGGATGATGTG/3AlexF647N/ |
| D5_REP_B_TOP | /5IAbRQ/CTTACCTTCATCCTCCACAATC |
| D5_REP_B_BOT | AATGGAAGATTGTGGAGGATGAAGGTAAG/3Rox_N/ |
| D5_REP_C_TOP | /5IABkFQ/CTCAACATTTCCACTATCCTTC |
| D5_REP_C_BOT | AAGAGTTGAAGGATAGTGGAAATGTTGAG/3AlexF488N/ |
| D5_REP_A_TOP† | CACATCATCCAACACCTTCCTC |
| D5_REP_A_BOT† | GAGAAGTGAGGAAGGTGTTGGATGATGTG |
| D5_REP_B_TOP† | CTTACCTTCATCCTCCACAATC |
| D5_REP_B_BOT† | AATGGAAGATTGTGGAGGATGAAGGTAAG |
| D5_REP_C_TOP† | CTCAACATTTCCACTATCCTTC |
| D5_REP_C_BOT† | AAGAGTTGAAGGATAGTGGAAATGTTGAG |

Table S17: **DNA sequences from Design 5.**

## S9.2 Molecular design diagrams for Design 4

Molecular design diagrams at the sequence level are provided for Design 4 in Figures S42 - S49. Note that (for historical reasons) the domain colors here are not identical to other figures: signal A domains are brown rather than red; signal B domains are gold rather than orange; and signal C domains are purple rather than blue. History domains are still black. We use the following abbreviations for fluorophores and quenchers: A488 = Alexa 488, A647 = Alexa 647, ROX = Rhodamine X, IB RQ = Iowa Black RQ, IB FQ = Iowa Black FQ.

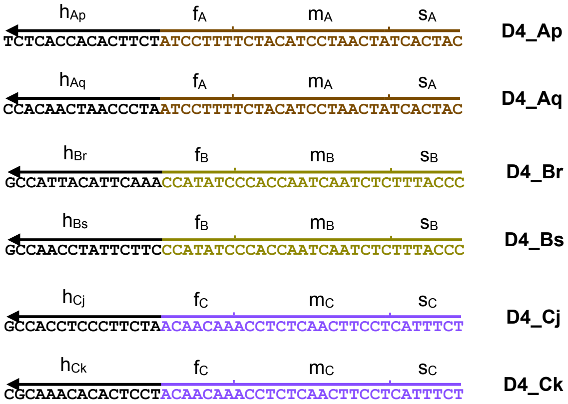

Figure S42: **Molecular design diagrams at the sequence level for signal strands in Design 4.**

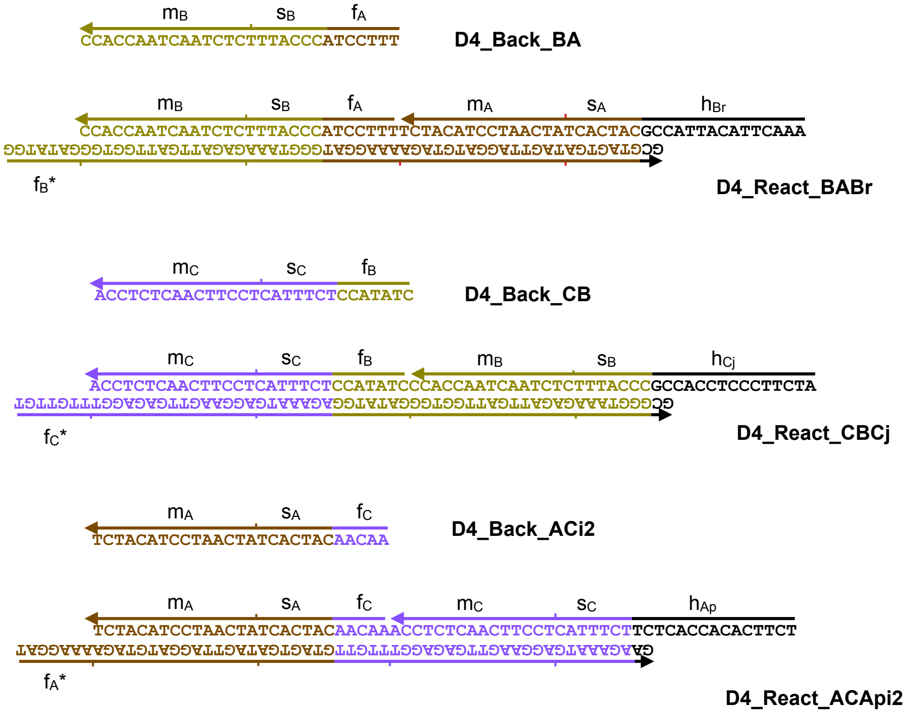

Figure S43: **Molecular design diagrams at the sequence level for the fuel species that mediate the react steps in Design 4.**

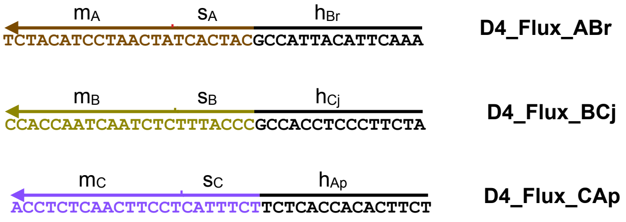

Figure S44: **Molecular design diagrams at the sequence level for the Flux species in Design 4.**

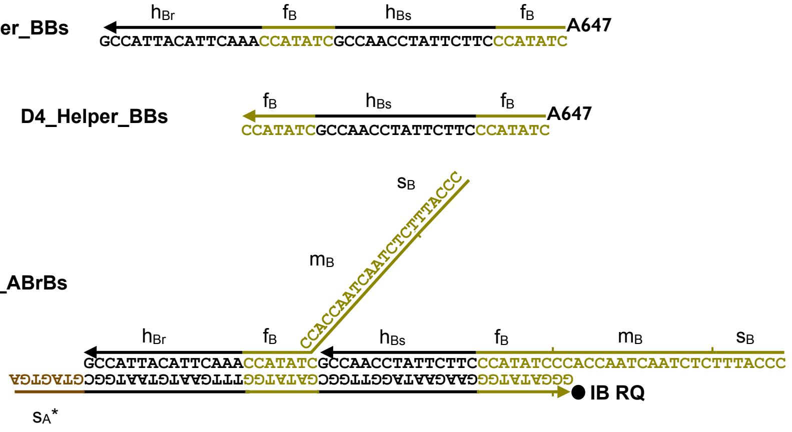

Figure S45: **Molecular design diagrams at the sequence level for the fuel species that mediate the produce step for the module B + A → 2 B in Design 4.**

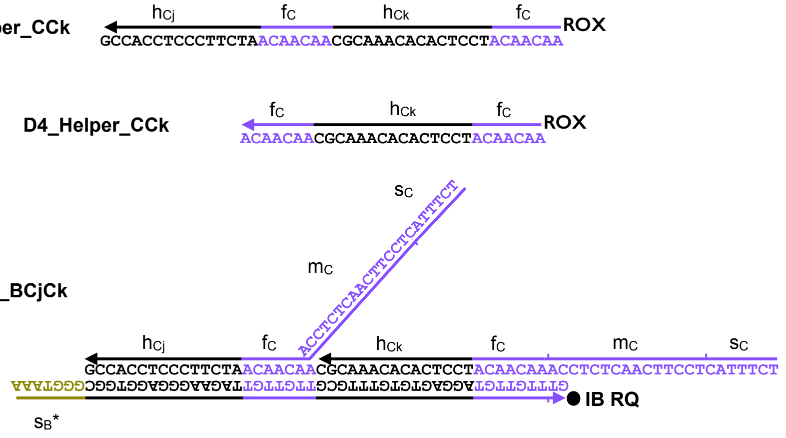

Figure S46: **Molecular design diagrams at the sequence level for the fuel species that mediate the produce step for the module C + B → 2 C in Design 4.**

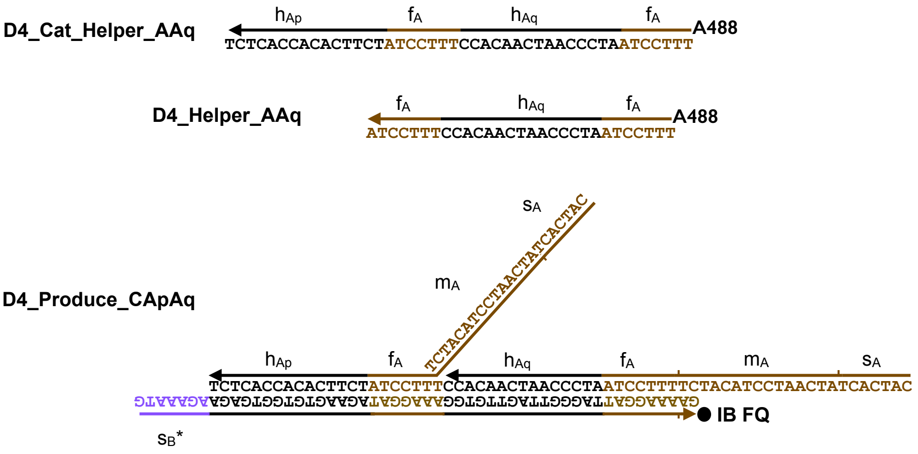

Figure S47: **Molecular design diagrams at the sequence level for the fuel species that mediate the produce step for the module A + C → 2 A in Design 4.**

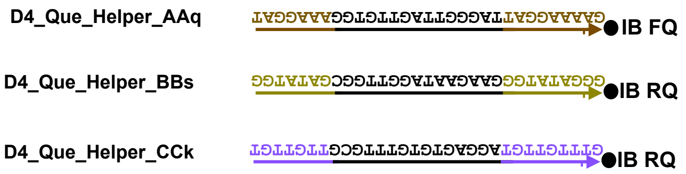

Figure S48: **Molecular design diagrams at the sequence level for the species that are used for normalizing Helper readout in Design 4.** These species are added at the end of the experiment for quenching the remaining Helper species.

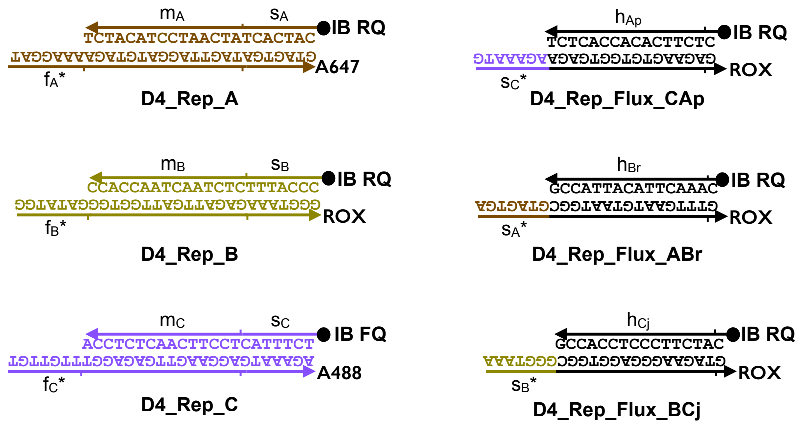

Figure S49: **Molecular design diagrams at the sequence level for the Reporter species used for reading out the concentrations of signal strands (left) and Flux strands (right) in Design 4.** Reporters for A, B, and C are also used as Thresholds in the autocatalytic delay modules and Displacillator experiments.

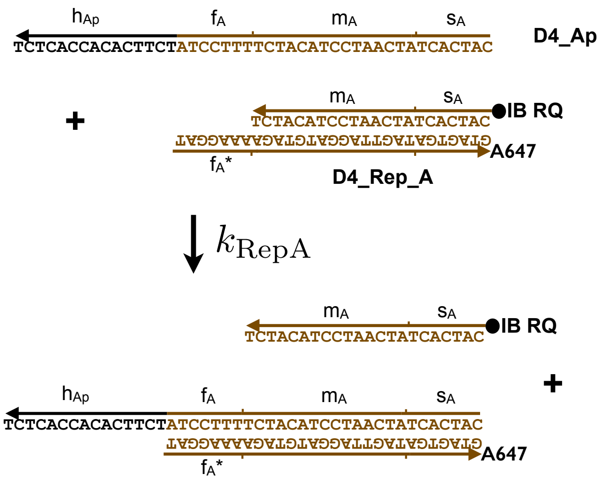

Figure S50: **Molecular design diagram at the sequence level for Reporters.** The measured value for the bimolecular rate constant for this pathway is specified in Table S3.

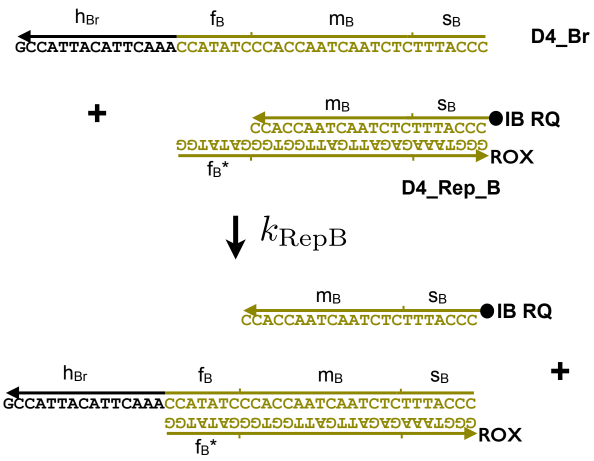

Figure S51: **Molecular design diagram at the sequence level for Reporters.** The measured value for the bimolecular rate constant for this pathway is specified in Table S3.

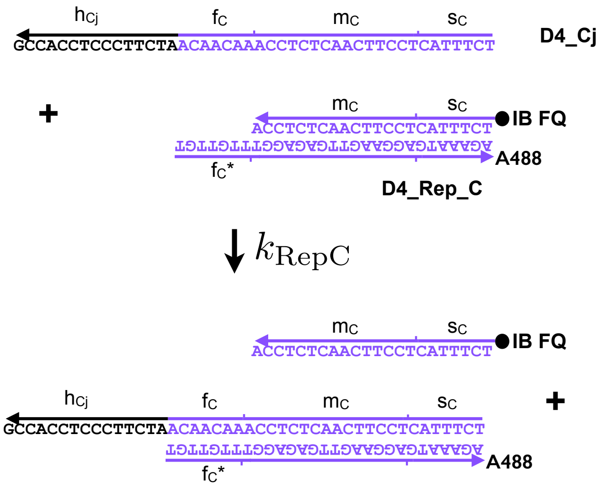

Figure S52: **Molecular design diagram at the sequence level for Reporters.** The measured value for the bimolecular rate constant for this pathway is specified in Table S3.

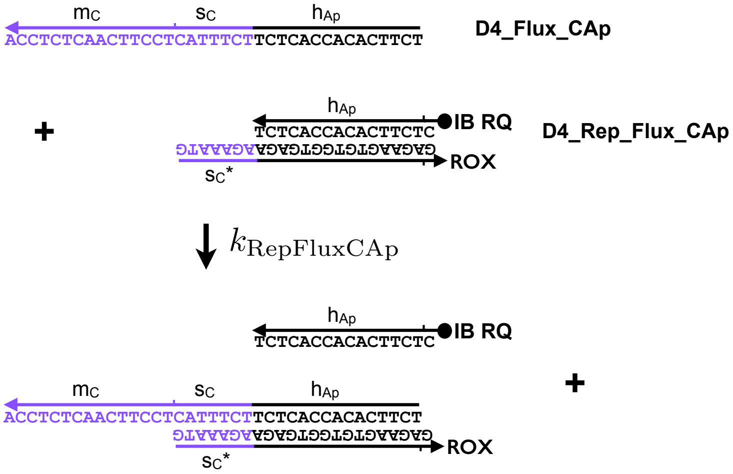

Figure S53: **Molecular design diagram at the sequence level for Reporters.** The measured value for the bimolecular rate constant for this pathway is specified in Table S1.

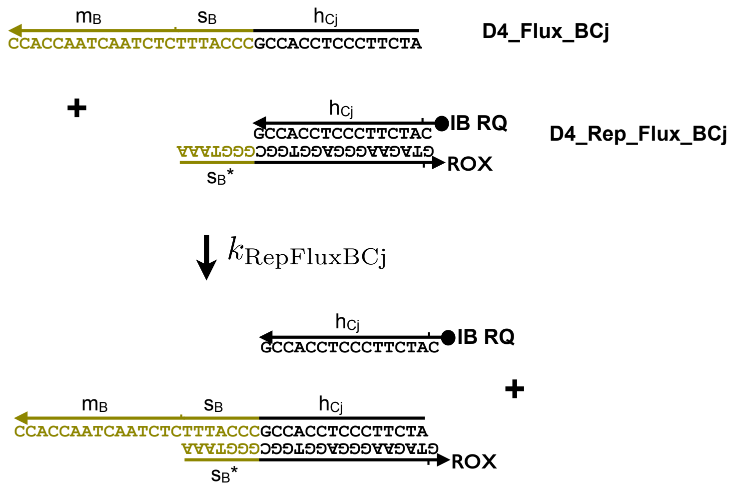

Figure S54: **Molecular design diagram at the sequence level for Reporters.** The measured value for the bimolecular rate constant for this pathway is specified in Table S1.

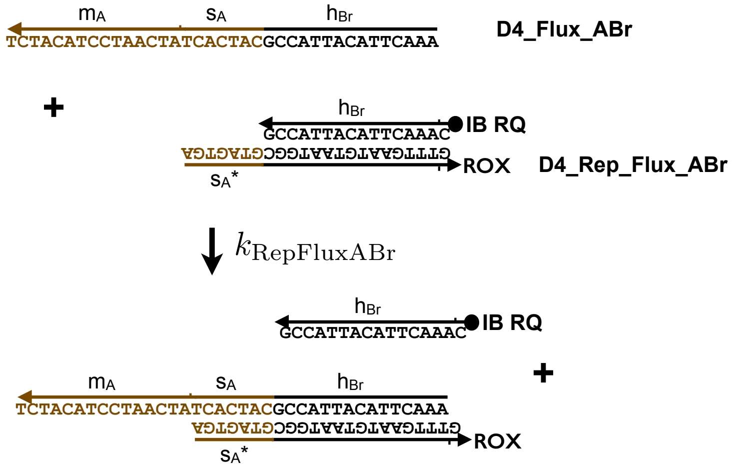

Figure S55: **Molecular design diagram at the sequence level for Reporters.** The measured value for the bimolecular rate constant for this pathway is specified in Table S1.

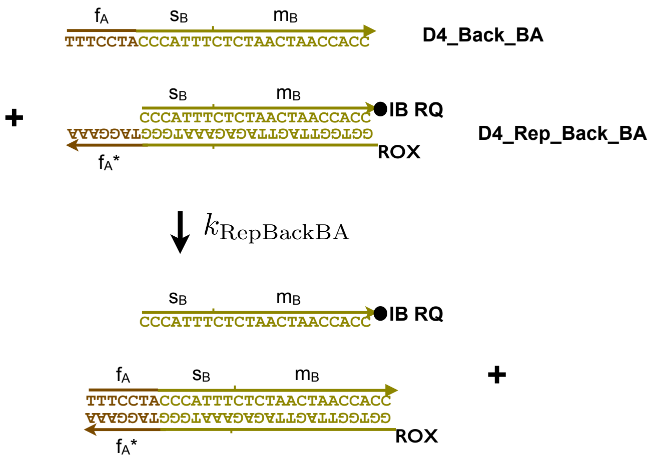

Figure S56: **Molecular design diagram at the sequence level for Reporters.** The measured value for the bimolecular rate constant for this pathway is specified in Table S1.

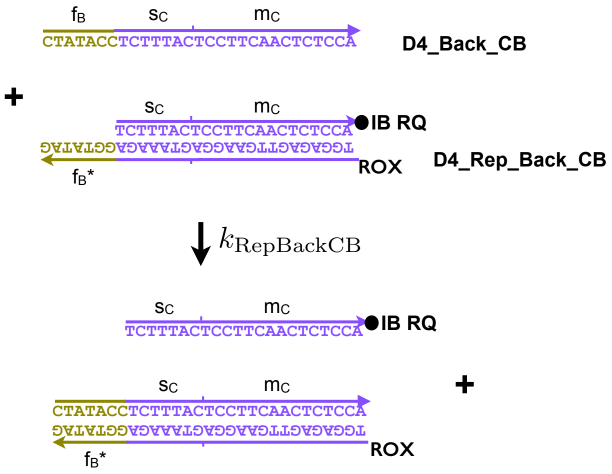

Figure S57: **Molecular design diagram at the sequence level for Reporters.** The measured value for the bimolecular rate constant for this pathway is specified in Table S1.

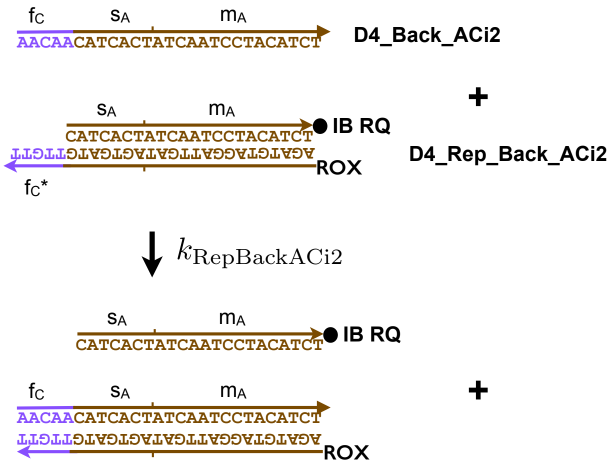

Figure S58: **Molecular design diagram at the sequence level for Reporters.** The measured value for the bimolecular rate constant for this pathway is specified in Table S1.

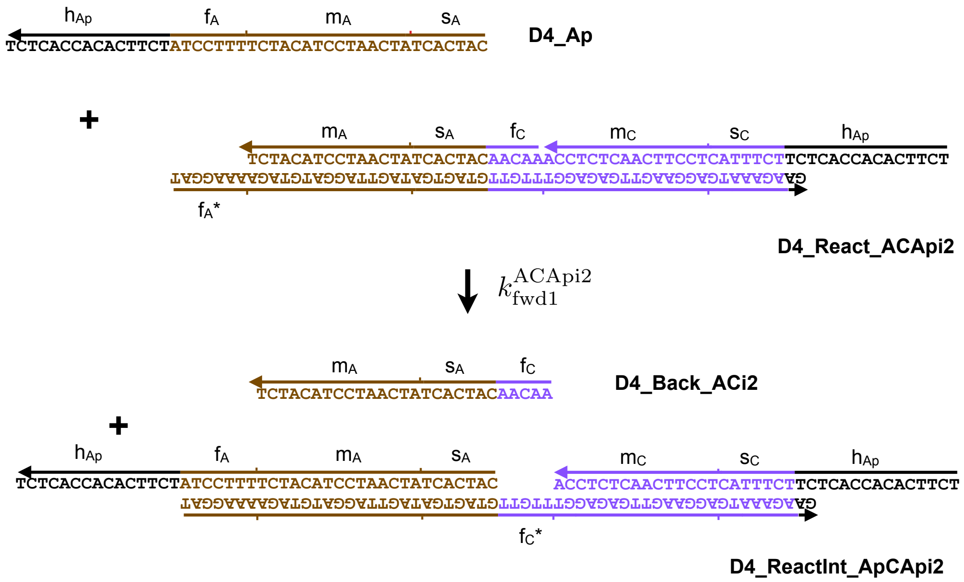

Figure S59: **Molecular design diagram at the sequence level for desired reaction pathways.** The measured value for the bimolecular rate constant for this pathway is specified in Table S2.

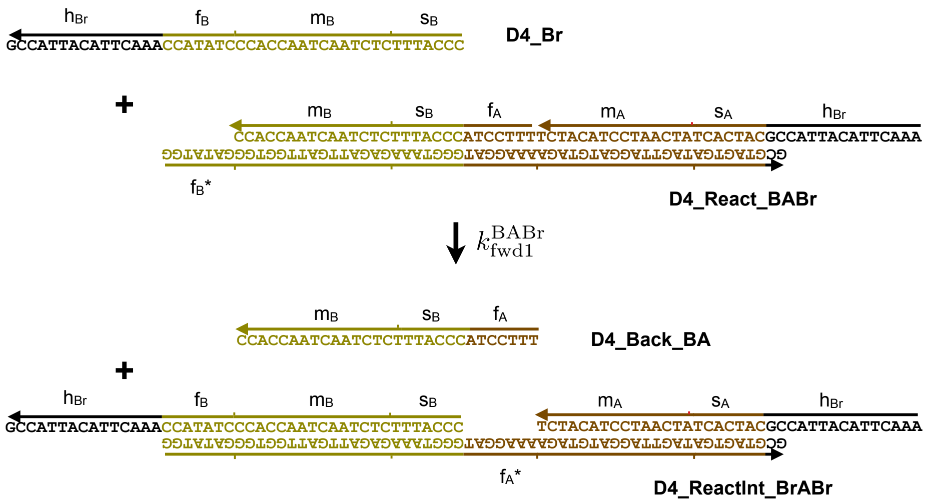

Figure S60: **Molecular design diagram at the sequence level for desired reaction pathways.** The measured value for the bimolecular rate constant for this pathway is specified in Table S2.

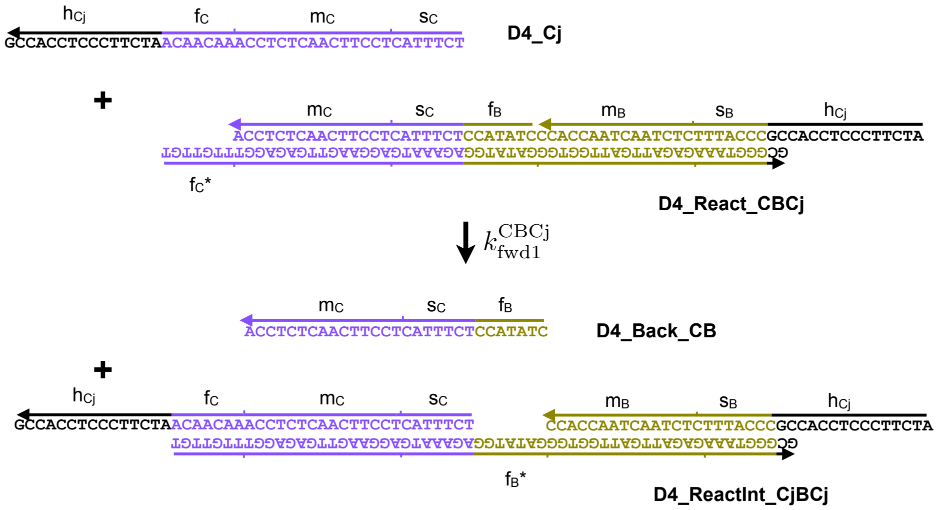

Figure S61: **Molecular design diagram at the sequence level for desired reaction pathways.** The measured value for the bimolecular rate constant for this pathway is specified in Table S2.

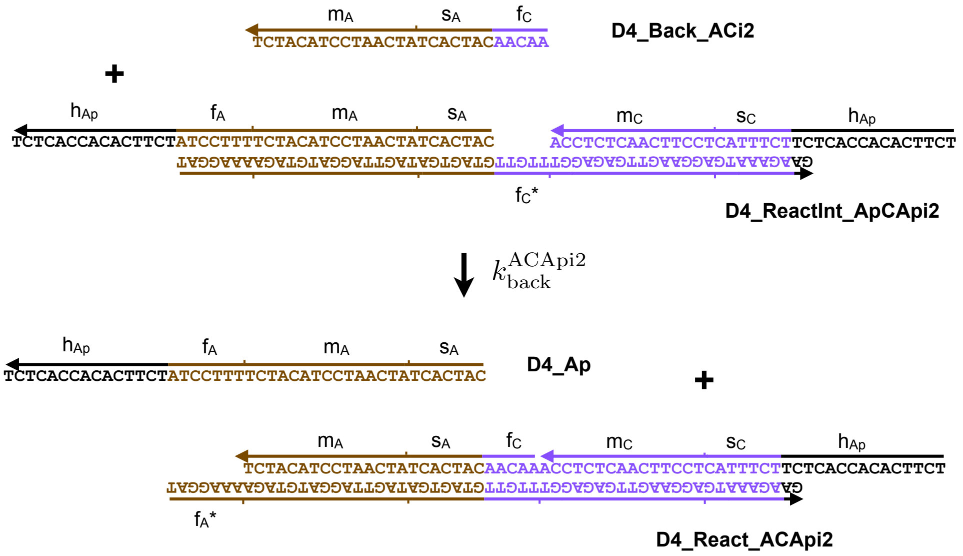

Figure S62: **Molecular design diagram at the sequence level for desired reaction pathways.** The measured value for the bimolecular rate constant for this pathway is specified in Table S2.

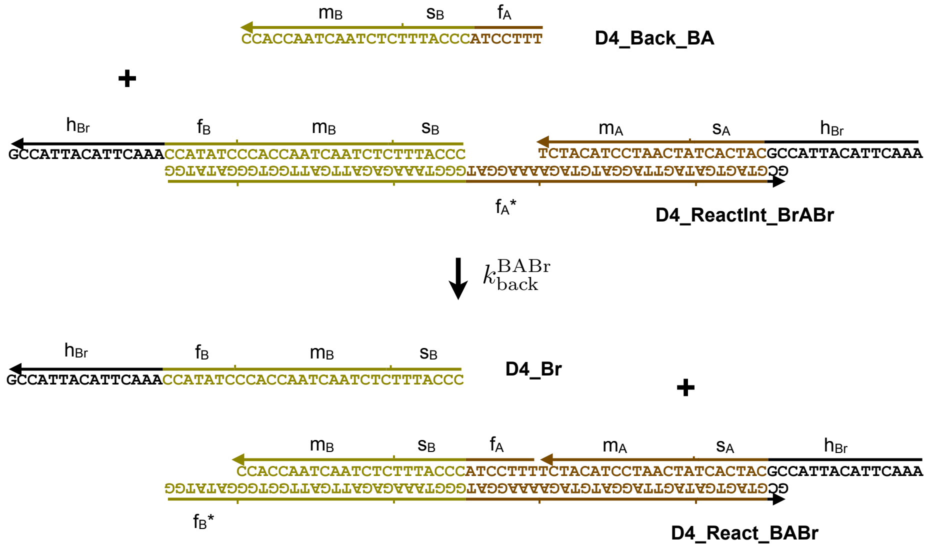

Figure S63: **Molecular design diagram at the sequence level for desired reaction pathways.** The measured value for the bimolecular rate constant for this pathway is specified in Table S2.

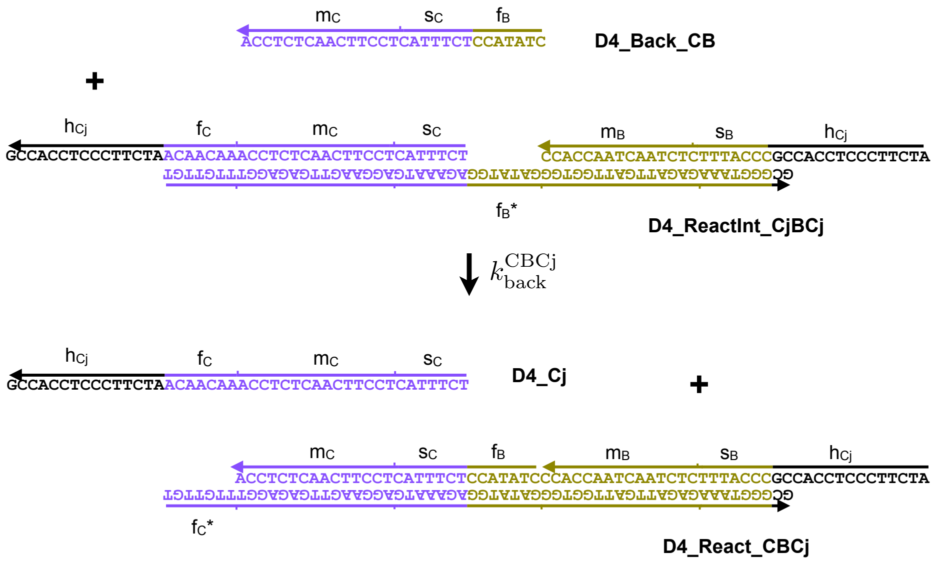

Figure S64: **Molecular design diagram at the sequence level for desired reaction pathways.** The measured value for the bimolecular rate constant for this pathway is specified in Table S2.

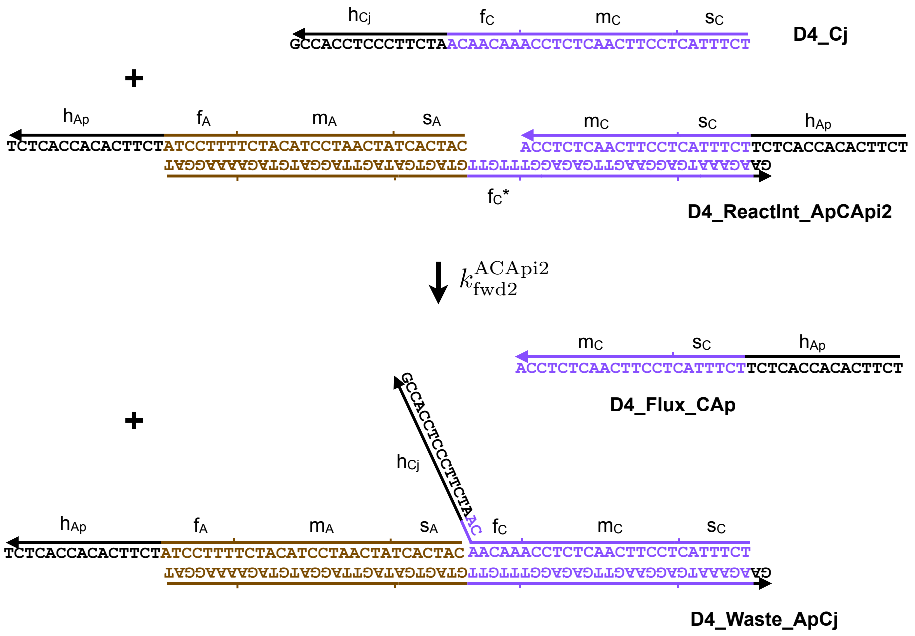

Figure S65: **Molecular design diagram at the sequence level for desired reaction pathways.** The measured value for the bimolecular rate constant for this pathway is specified in Table S2.

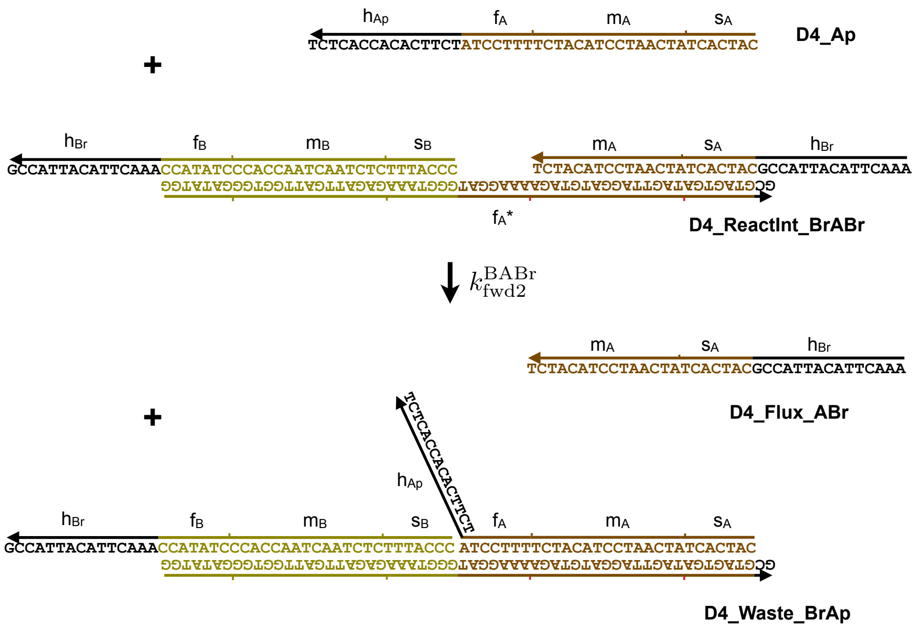

Figure S66: **Molecular design diagram at the sequence level for desired reaction pathways.** The measured value for the bimolecular rate constant for this pathway is specified in Table S2.

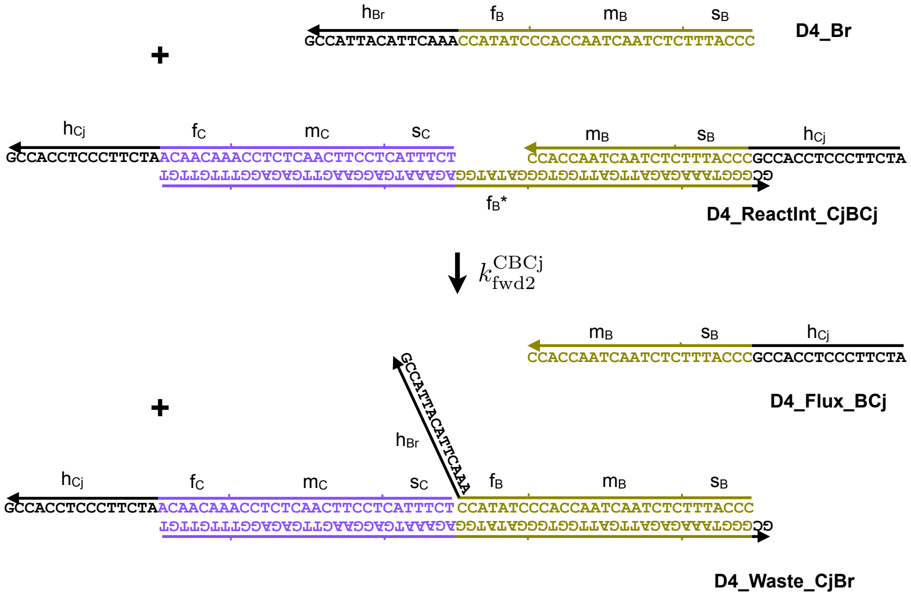

Figure S67: **Molecular design diagram at the sequence level for desired reaction pathways.** The measured value for the bimolecular rate constant for this pathway is specified in Table S2.

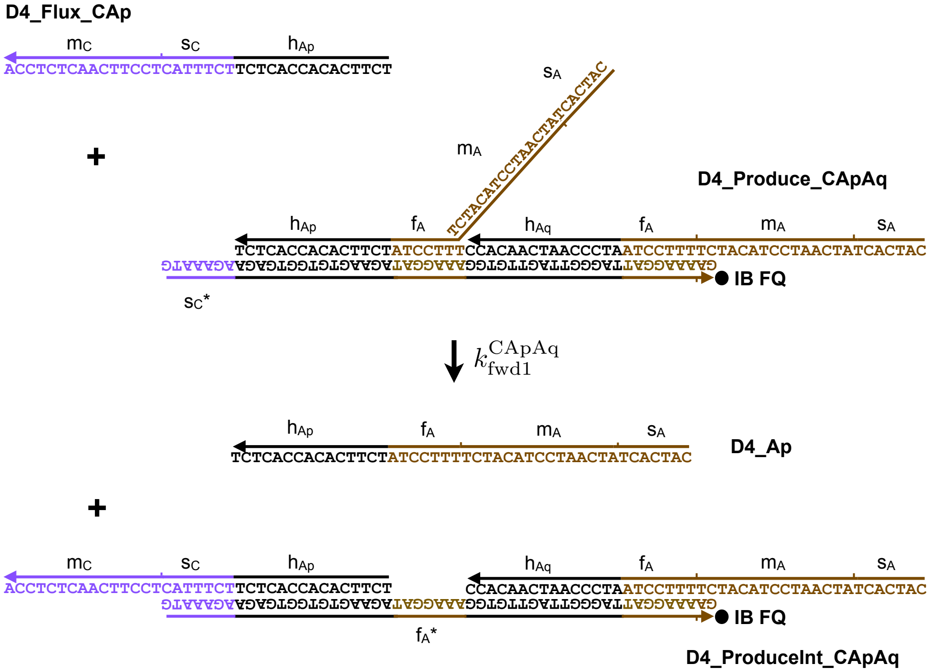

Figure S68: **Molecular design diagram at the sequence level for desired reaction pathways.** The measured value for the bimolecular rate constant for this pathway is specified in Table S2.

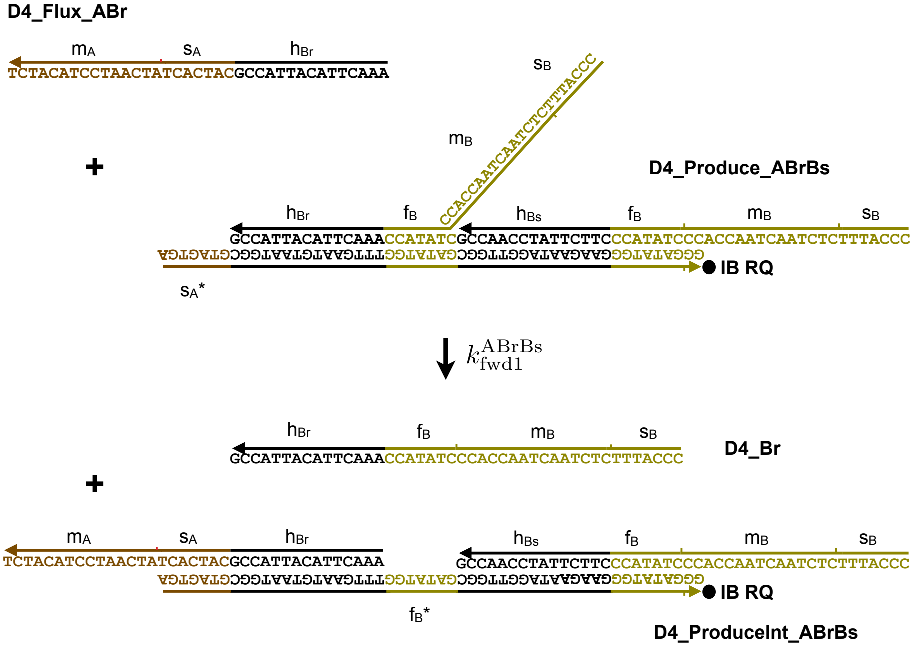

Figure S69: **Molecular design diagram at the sequence level for desired reaction pathways.** The measured value for the bimolecular rate constant for this pathway is specified in Table S2.

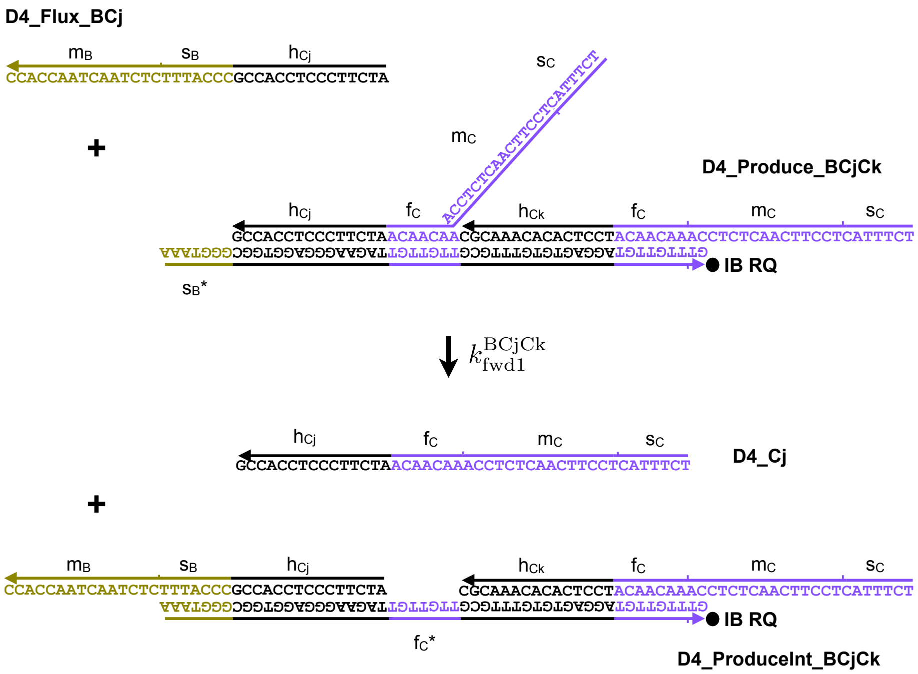

Figure S70: **Molecular design diagram at the sequence level for desired reaction pathways.** The measured value for the bimolecular rate constant for this pathway is specified in Table S2.

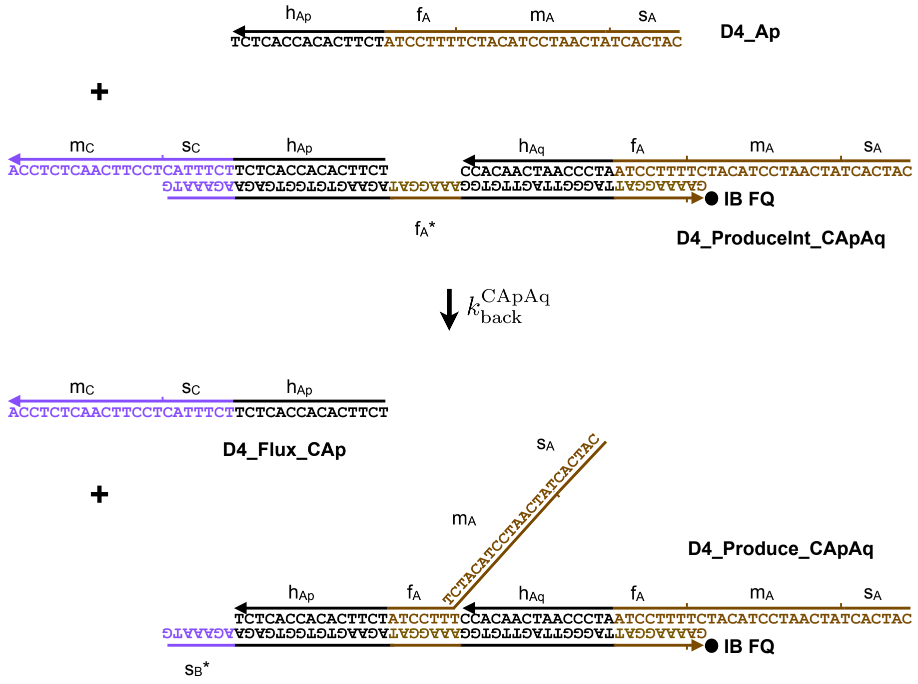

Figure S71: **Molecular design diagram at the sequence level for desired reaction pathways.** The measured value for the bimolecular rate constant for this pathway is specified in Table S2.

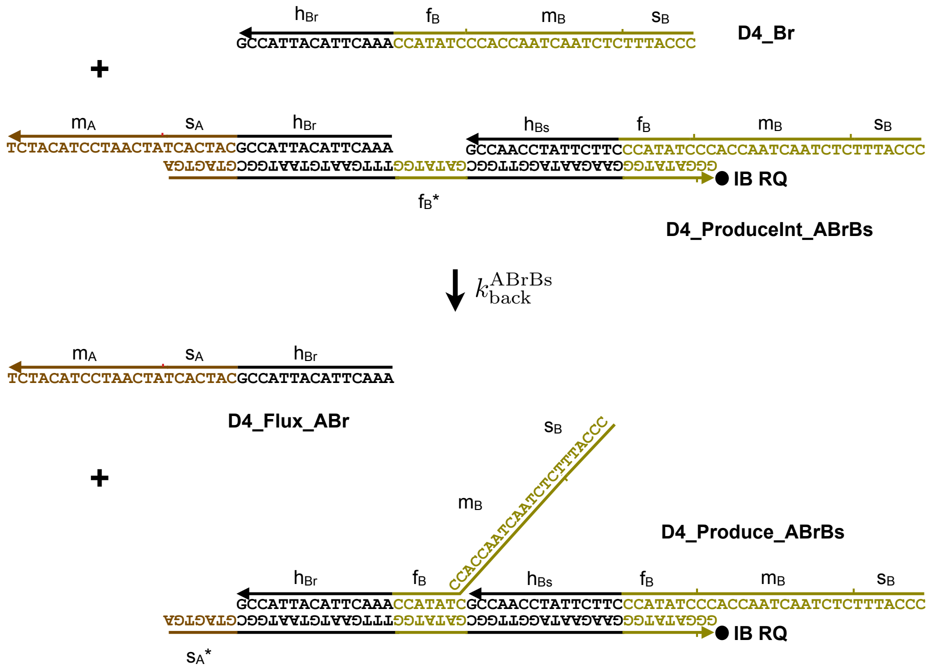

Figure S72: **Molecular design diagram at the sequence level for desired reaction pathways.** The measured value for the bimolecular rate constant for this pathway is specified in Table S2.

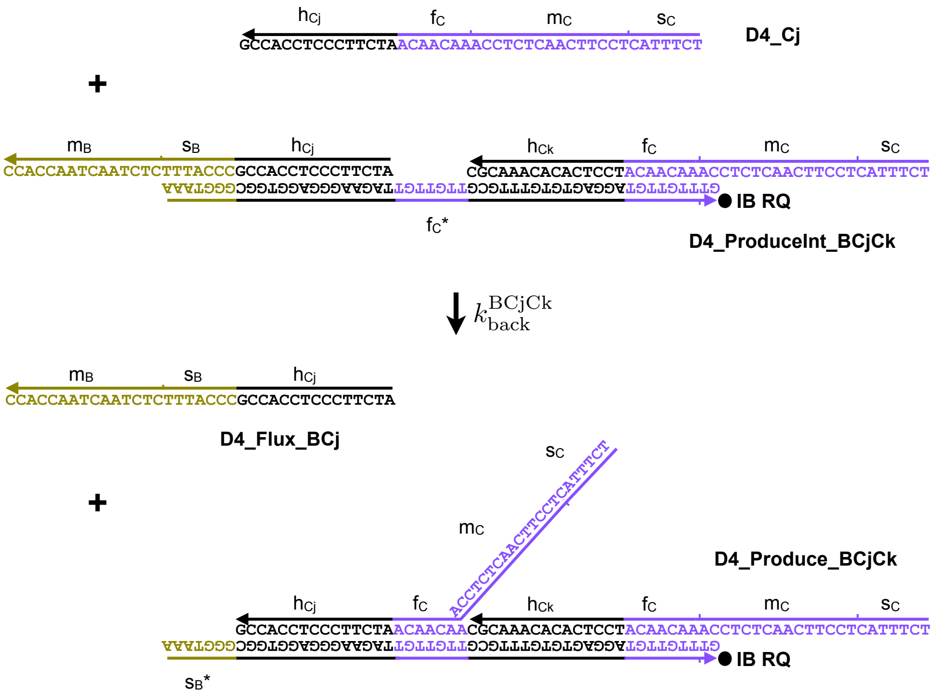

Figure S73: **Molecular design diagram at the sequence level for desired reaction pathways.** The measured value for the bimolecular rate constant for this pathway is specified in Table S2.

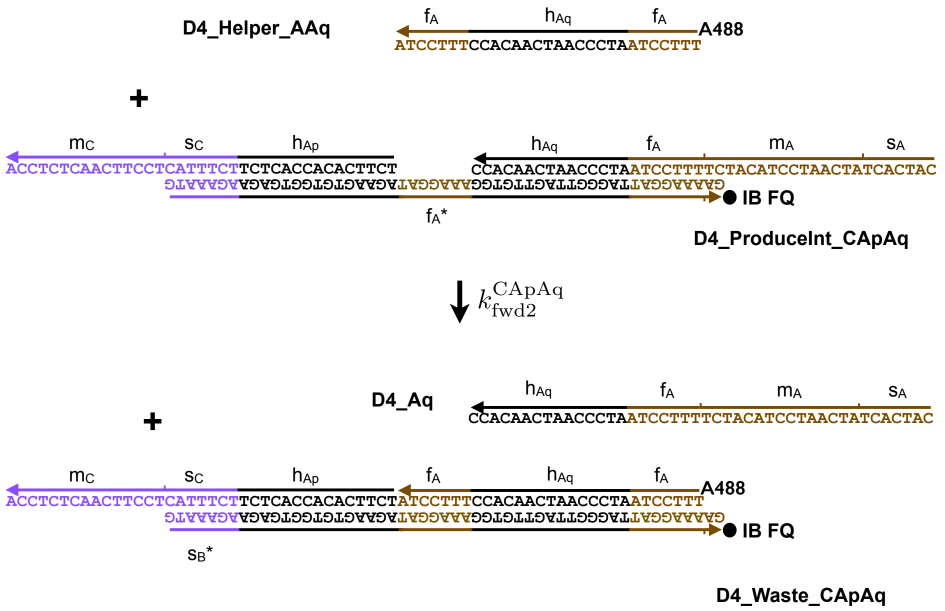

Figure S74: **Molecular design diagram at the sequence level for desired reaction pathways.** The measured value for the bimolecular rate constant for this pathway is specified in Table S2.

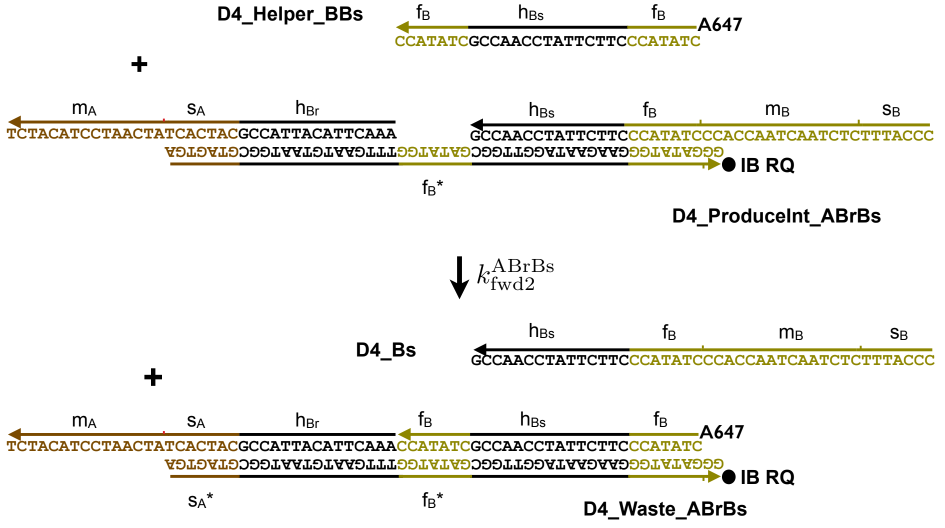

Figure S75: **Molecular design diagram at the sequence level for desired reaction pathways.** The measured value for the bimolecular rate constant for this pathway is specified in Table S2.

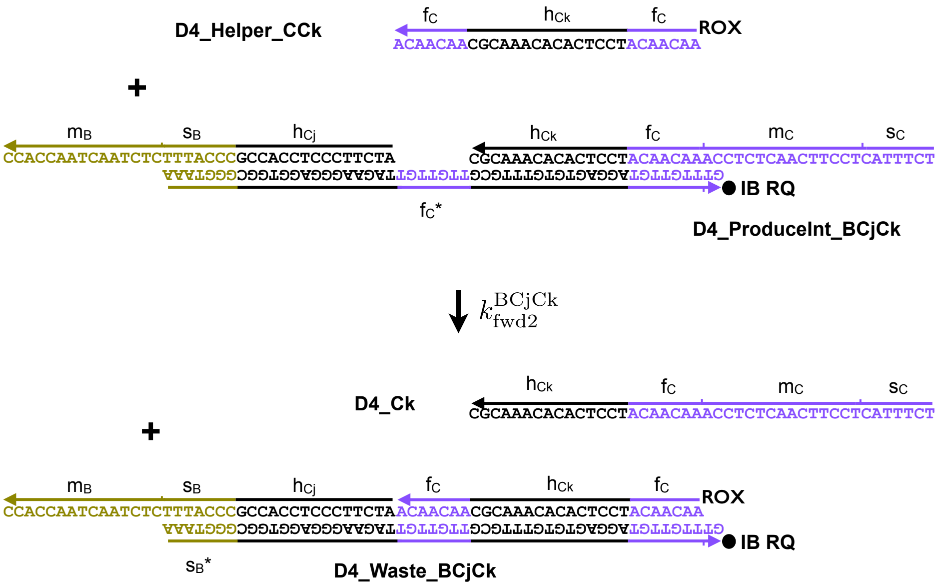

Figure S76: **Molecular design diagram at the sequence level for desired reaction pathways.** The measured value for the bimolecular rate constant for this pathway is specified in Table S2.

## References and Notes

1. W. C. Bray, A periodic reaction in homogeneous solution and its relation to catalysis. *J. Am. Chem. Soc.* **43**, 1262–1267 (1921). doi:10.1021/ja01439a007

2. B. P. Belousov, *Collection of Abstracts on Radiation Medicine* (Medgiz, 1959), pp. 145–147.

3. I. R. Epstein, J. A. Pojman, *An Introduction to Nonlinear Chemical Dynamics: Oscillations, Waves, Patterns, and Chaos* (Oxford Univ. Press, 1998).

4. T. S. Gardner, C. R. Cantor, J. J. Collins, Construction of a genetic toggle switch in *Escherichia coli*. *Nature* **403**, 339–342 (2000). doi:10.1038/35002131 Medline

5. M. B. Elowitz, S. Leibler, A synthetic oscillatory network of transcriptional regulators. *Nature* **403**, 335–338 (2000). doi:10.1038/35002125 Medline

6. M. R. Atkinson, M. A. Savageau, J. T. Myers, A. J. Ninfa, Development of genetic circuitry exhibiting toggle switch or oscillatory behavior in *Escherichia coli*. *Cell* **113**, 597–607 (2003). doi:10.1016/S0092-8674(03)00346-5 Medline

7. J. Stricker, S. Cookson, M. R. Bennett, W. H. Mather, L. S. Tsimring, J. Hasty, A fast, robust and tunable synthetic gene oscillator. *Nature* **456**, 516–519 (2008). doi:10.1038/nature07389 Medline

8. B. Wlotzka, J. S. McCaskill, A molecular predator and its prey: Coupled isothermal amplification of nucleic acids. *Chem. Biol.* **4**, 25–33 (1997). doi:10.1016/S1074-5521(97)90234-9 Medline

9. J. Kim, K. S. White, E. Winfree, Construction of an in vitro bistable circuit from synthetic transcriptional switches. *Mol. Syst. Biol.* **2**, 68 (2006). doi:10.1038/msb4100099 Medline

10. J. Kim, E. Winfree, Synthetic in vitro transcriptional oscillators. *Mol. Syst. Biol.* **7**, 465 (2011). doi:10.1038/msb.2010.119 Medline

11. K. Montagne, R. Plasson, Y. Sakai, T. Fujii, Y. Rondelez, Programming an *in vitro* DNA oscillator using a molecular networking strategy. *Mol. Syst. Biol.* **7**, 466 (2011). doi:10.1038/msb.2010.120 Medline

12. A. Padirac, T. Fujii, Y. Rondelez, Bottom-up construction of in vitro switchable memories. *Proc. Natl. Acad. Sci. U.S.A.* **109**, E3212–E3220 (2012). doi:10.1073/pnas.1212069109 Medline

13. T. Fujii, Y. Rondelez, Predator–prey molecular ecosystems. *ACS Nano* **7**, 27–34 (2013). doi:10.1021/nn3043572 Medline

14. S. N. Semenov, A. S. Y. Wong, R. M. van der Made, S. G. J. Postma, J. Groen, H. W. H. van Roekel, T. F. A. de Greef, W. T. S. Huck, Rational design of functional and tunable oscillating enzymatic networks. *Nat. Chem.* **7**, 160–165 (2015). doi:10.1038/nchem.2142 Medline

15. D. Bray, Protein molecules as computational elements in living cells. *Nature* **376**, 307–312 (1995). doi:10.1038/376307a0 Medline

16. J. J. Tyson, K. C. Chen, B. Novak, Sniffers, buzzers, toggles and blinkers: Dynamics of regulatory and signaling pathways in the cell. *Curr. Opin. Cell Biol.* **15**, 221–231 (2003). doi:10.1016/S0955-0674(03)00017-6 Medline

17. F. Horn, R. Jackson, General mass action kinetics. *Arch. Ration. Mech. Anal.* **47**, 81–116 (1972). doi:10.1007/BF00251225

18. P. Érdi, J. Tóth, *Mathematical Models of Chemical Reactions: Theory and Applications of Deterministic and Stochastic Models* (Princeton University Press, 1989).

19. M. Korzuhin, *Oscillatory Processes in Biological and Chemical Systems* (Nauka, 1967), pp. 231–251.

20. W. Klonowski, Simplifying principles for chemical and enzyme reaction kinetics. *Biophys. Chem.* **18**, 73–87 (1983). doi:10.1016/0301-4622(83)85001-7 Medline

21. K. Oishi, E. Klavins, Biomolecular implementation of linear I/O systems. *IET Syst. Biol.* **5**, 252–260 (2011). doi:10.1049/iet-syb.2010.0056 Medline

22. A. Hjelmfelt, J. Ross, Implementation of logic functions and computations by chemical kinetics. *Physica D* **84**, 180–193 (1995). doi:10.1016/0167-2789(95)00014-U

23. A. Hjelmfelt, E. D. Weinberger, J. Ross, Chemical implementation of neural networks and Turing machines. *Proc. Natl. Acad. Sci. U.S.A.* **88**, 10983–10987 (1991). doi:10.1073/pnas.88.24.10983 Medline

24. J. Aspnes, E. Ruppert, An introduction to population protocols, in *Middleware for Network Eccentric and Mobile Applications*, B. Garbinato, H. Miranda, L. Rodrigues, Eds. (Springer-Verlag, 2009), pp. 97–120.

25. A. Hjelmfelt, E. D. Weinberger, J. Ross, Chemical implementation of finite-state machines. *Proc. Natl. Acad. Sci. U.S.A.* **89**, 383–387 (1992). doi:10.1073/pnas.89.1.383 Medline

26. D. Y. Zhang, G. Seelig, Dynamic DNA nanotechnology using strand-displacement reactions. *Nat. Chem.* **3**, 103–113 (2011). doi:10.1038/nchem.957 Medline

27. J. SantaLucia Jr., D. Hicks, The thermodynamics of DNA structural motifs. *Annu. Rev. Biophys. Biomol. Struct.* **33**, 415–440 (2004). doi:10.1146/annurev.biophys.32.110601.141800 Medline

28. J. N. Zadeh, C. D. Steenberg, J. S. Bois, B. R. Wolfe, M. B. Pierce, A. R. Khan, R. M. Dirks, N. A. Pierce, NUPACK: Analysis and design of nucleic acid systems. *J. Comput. Chem.* **32**, 170–173 (2011). doi:10.1002/jcc.v32:1 Medline

29. N. C. Seeman, De novo design of sequences for nucleic acid structural engineering. *J. Biomol. Struct. Dyn.* **8**, 573–581 (1990). doi:10.1080/07391102.1990.10507829 Medline

30. R. M. Dirks, M. Lin, E. Winfree, N. A. Pierce, Paradigms for computational nucleic acid design. *Nucleic Acids Res.* **32**, 1392–1403 (2004). doi:10.1093/nar/gkh291 Medline

31. J. N. Zadeh, B. R. Wolfe, N. A. Pierce, Nucleic acid sequence design via efficient ensemble defect optimization. *J. Comput. Chem.* **32**, 439–452 (2011). doi:10.1002/jcc.21633 Medline

32. B. R. Wolfe, N. A. Pierce, Sequence design for a test tube of interacting nucleic acid strands. *ACS Synth. Biol.* **4**, 1086–1100 (2015). doi:10.1021/sb5002196 Medline

33. B. R. Wolfe, N. J. Porubsky, J. N. Zadeh, R. M. Dirks, N. A. Pierce, Constrained multistate sequence design for nucleic acid reaction pathway engineering. *J. Am. Chem. Soc.* **139**, 3134–3144 (2017). doi:10.1021/jacs.6b12693 Medline

34. B. Yurke, A. P. Mills Jr., Using DNA to power nanostructures. *Genet. Program. Evolvable Mach.* **4**, 111–122 (2003). doi:10.1023/A:1023928811651

35. D. Y. Zhang, E. Winfree, Control of DNA strand displacement kinetics using toehold exchange. *J. Am. Chem. Soc.* **131**, 17303–17314 (2009). doi:10.1021/ja906987s Medline

36. N. Srinivas, T. E. Ouldridge, P. Šulc, J. M. Schaeffer, B. Yurke, A. A. Louis, J. P. K. Doye, E. Winfree, On the biophysics and kinetics of toehold-mediated DNA strand displacement. *Nucleic Acids Res.* **41**, 10641–10658 (2013). doi:10.1093/nar/gkt801 Medline

37. B. Yurke, A. J. Turberfield, A. P. Mills Jr., F. C. Simmel, J. L. Neumann, A DNA-fuelled molecular machine made of DNA. *Nature* **406**, 605–608 (2000). doi:10.1038/35020524 Medline

38. G. Seelig, D. Soloveichik, D. Y. Zhang, E. Winfree, Enzyme-free nucleic acid logic circuits. *Science* **314**, 1585–1588 (2006). doi:10.1126/science.1132493 Medline

39. L. Qian, E. Winfree, Scaling up digital circuit computation with DNA strand displacement cascades. *Science* **332**, 1196–1201 (2011). doi:10.1126/science.1200520 Medline

40. D. Y. Zhang, A. J. Turberfield, B. Yurke, E. Winfree, Engineering entropy-driven reactions and networks catalyzed by DNA. *Science* **318**, 1121–1125 (2007). doi:10.1126/science.1148532 Medline

41. P. Yin, H. M. T. Choi, C. R. Calvert, N. A. Pierce, Programming biomolecular self-assembly pathways. *Nature* **451**, 318–322 (2008). doi:10.1038/nature06451 Medline

42. J. P. Sadowski, C. R. Calvert, D. Y. Zhang, N. A. Pierce, P. Yin, Developmental self-assembly of a DNA tetrahedron. *ACS Nano* **8**, 3251–3259 (2014). doi:10.1021/nn4038223 Medline

43. D. Soloveichik, G. Seelig, E. Winfree, DNA as a universal substrate for chemical kinetics. *Proc. Natl. Acad. Sci. U.S.A.* **107**, 5393–5398 (2010). doi:10.1073/pnas.0909380107 Medline

44. L. Cardelli, Two-domain DNA strand displacement. *Math. Struct. Comput. Sci.* **23**, 247–271 (2013). doi:10.1017/S0960129512000102

45. Y.-J. Chen, N. Dalchau, N. Srinivas, A. Phillips, L. Cardelli, D. Soloveichik, G. Seelig, Programmable chemical controllers made from DNA. *Nat. Nanotechnol.* **8**, 755–762 (2013). doi:10.1038/nnano.2013.189 Medline

46. M. Lachmann, G. Sella, The computationally complete ant colony: global coordination in a system with no hierarchy, in *Advances in Artificial Life* (*Lecture Notes in Computer Science*), F. Morán, A. Moreno, J. J. Merelo, P. Chacón, Eds. (Springer, 1995), pp. 784–800.

47. L. Cardelli, Artificial biochemistry, in *Algorithmic Bioprocesses*, A. Condon, D. Harel, J. N. Kok, A. Salomaa, E. Winfree, Eds. (Springer, 2009), pp. 429–462.

48. T. Reichenbach, M. Mobilia, E. Frey, Coexistence versus extinction in the stochastic cyclic Lotka-Volterra model. *Phys. Rev. E* **74**, 051907 (2006). doi:10.1103/PhysRevE.74.051907 Medline

49. A. Dobrinevski, E. Frey, Extinction in neutrally stable stochastic Lotka-Volterra models. *Phys. Rev. E* **85**, 051903 (2012). doi:10.1103/PhysRevE.85.051903 Medline

50. M. R. Lakin, S. Youssef, L. Cardelli, A. Phillips, Abstractions for DNA circuit design. *J. R. Soc. Interface* **9**, 470–486 (2012). doi:10.1098/rsif.2011.0343 Medline

51. L. P. Reynaldo, A. V. Vologodskii, B. P. Neri, V. I. Lyamichev, The kinetics of oligonucleotide replacements. *J. Mol. Biol.* **297**, 511–520 (2000). doi:10.1006/jmbi.2000.3573 Medline

52. A. J. Genot, D. Y. Zhang, J. Bath, A. J. Turberfield, Remote toehold: A mechanism for flexible control of DNA hybridization kinetics. *J. Am. Chem. Soc.* **133**, 2177–2182 (2011). doi:10.1021/ja1073239 Medline

53. D. Y. Zhang, E. Winfree, Robustness and modularity properties of a non-covalent DNA catalytic reaction. *Nucleic Acids Res.* **38**, 4182–4197 (2010). doi:10.1093/nar/gkq088 Medline

54. DNA and Natural Algorithms Group github page, https://github.com/DNA-and-Natural-Algorithms-Group

55. C. G. Evans, E. Winfree, in *DNA Computing and Molecular Programming*, vol. 8141, *Lecture Notes in Computer Science*, D. Soloveichik, B. Yurke, Eds. (Springer, 2013), pp. 61–75.

56. L. Cardelli, Strand algebras for DNA computing. *Nat. Comput.* **10**, 407–428 (2011). doi:10.1007/s11047-010-9236-7

57. L. Qian, D. Soloveichik, E. Winfree, Turing-universal computation with DNA polymers, in *DNA Computing and Molecular Programming*, vol 6518, *Lecture Notes in Computer Science*, Y. Sakakibara, Y. Mi, Eds. (Springer, 2011), pp. 123–140.

82. H. Niederholtmeyer, Z. Z. Sun, Y. Hori, E. Yeung, A. Verpoorte, R. M. Murray, S. J. Maerkl, Rapid cell-free forward engineering of novel genetic ring oscillators. *eLife* **4**, e09771 (2015). doi:10.7554/eLife.09771 Medline

59. A. Baccouche, K. Montagne, A. Padirac, T. Fujii, Y. Rondelez, Dynamic DNA-toolbox reaction circuits: A walkthrough. *Methods* **67**, 234–249 (2014). doi:10.1016/j.ymeth.2014.01.015 Medline

60. J. Garamella, R. Marshall, M. Rustad, V. Noireaux, The all *E. coli* TX-TL Toolbox 2.0: A platform for cell-free synthetic biology. *ACS Synth. Biol.* **5**, 344–355 (2016). doi:10.1021/acssynbio.5b00296 Medline

61. J. Kim, J. J. Hopfield, E. Winfree, Neural network computation by in vitro transcriptional circuits, in *Advances in Neural Information Processing Systems*, L. K. Saul, Y. Weiss, L. Bottou, Eds. (MIT Press, 2004), pp. 681–688.

62. Y. Shimizu, A. Inoue, Y. Tomari, T. Suzuki, T. Yokogawa, K. Nishikawa, T. Ueda, Cell-free translation reconstituted with purified components. *Nat. Biotechnol.* **19**, 751–755 (2001). doi:10.1038/90802 Medline

63. J. M. Schaeffer, C. Thachuk, E. Winfree, Stochastic simulation of the kinetics of multiple interacting nucleic acid strands, in *DNA Computing and Molecular Programming,* vol. 9211, *Lecture Notes in Computer Science*, A. Phillips, P. Yin, Eds. (Springer, 2015), pp. 194–211.

64. T. E. Ouldridge, P. Šulc, F. Romano, J. P. K. Doye, A. A. Louis, DNA hybridization kinetics: Zippering, internal displacement and sequence dependence. *Nucleic Acids Res.* **41**, 8886–8895 (2013). doi:10.1093/nar/gkt687 Medline

65. C. Thachuk, E. Winfree, D. Soloveichik, in *DNA Computing and Molecular Programming*, vol 9211, *Lecture Notes in Computer Science*, A. Phillips, P. Yin, eds. (Springer, 2015), pp. 133–153.

66. I. R. Epstein, Complex dynamical behavior in “simple” chemical systems. *J. Phys. Chem.* **88**, 187–198 (1984). doi:10.1021/j150646a007

67. D. Y. Zhang, R. F. Hariadi, H. M. T. Choi, E. Winfree, Integrating DNA strand-displacement circuitry with DNA tile self-assembly. *Nat. Commun.* **4**, 1965 (2013). doi:10.1038/ncomms2965 Medline

68. N. C. Seeman, *Structural DNA Nanotechnology* (Cambridge University Press, 2016).

69. M. N. Stojanovic, D. M. Kolpashchikov, Modular aptameric sensors. *J. Am. Chem. Soc.* **126**, 9266–9270 (2004). doi:10.1021/ja032013t Medline

70. E. J. Cho, J.-W. Lee, A. D. Ellington, Applications of aptamers as sensors. *Annu. Rev. Anal. Chem. (Palo Alto Calif.)* **2**, 241–264 (2009). doi:10.1146/annurev.anchem.1.031207.112851 Medline

71. S. Liao, N. C. Seeman, Translation of DNA signals into polymer assembly instructions. *Science* **306**, 2072–2074 (2004). doi:10.1126/science.1104299 Medline

72. Y. He, D. R. Liu, Autonomous multistep organic synthesis in a single isothermal solution mediated by a DNA walker. *Nat. Nanotechnol.* **5**, 778–782 (2010). doi:10.1038/nnano.2010.190 Medline

73. W. Meng, R. A. Muscat, M. L. McKee, P. J. Milnes, A. H. El-Sagheer, J. Bath, B. G. Davis, T. Brown, R. K. O'Reilly, A. J. Turberfield, An autonomous molecular assembler for programmable chemical synthesis. *Nat. Chem.* **8**, 542–548 (2016). doi:10.1038/nchem.2495 Medline

74. H. Gu, J. Chao, S.-J. Xiao, N. C. Seeman, A proximity-based programmable DNA nanoscale assembly line. *Nature* **465**, 202–205 (2010). doi:10.1038/nature09026 Medline

75. J. Fu, M. Liu, Y. Liu, N. W. Woodbury, H. Yan, Interenzyme substrate diffusion for an enzyme cascade organized on spatially addressable DNA nanostructures. *J. Am. Chem. Soc.* **134**, 5516–5519 (2012). doi:10.1021/ja300897h Medline

76. S. M. Douglas, I. Bachelet, G. M. Church, A logic-gated nanorobot for targeted transport of molecular payloads. *Science* **335**, 831–834 (2012). doi:10.1126/science.1214081 Medline

77. R. Schreiber, J. Do, E.-M. Roller, T. Zhang, V. J. Schüller, P. C. Nickels, J. Feldmann, T. Liedl, Hierarchical assembly of metal nanoparticles, quantum dots and organic dyes using DNA origami scaffolds. *Nat. Nanotechnol.* **9**, 74–78 (2014). doi:10.1038/nnano.2013.253 Medline

78. C. Zhou, X. Duan, N. Liu, A plasmonic nanorod that walks on DNA origami. *Nat. Commun.* **6**, 8102 (2015). doi:10.1038/ncomms9102 Medline

79. N. C. Gianneschi, M. R. Ghadiri, Design of molecular logic devices based on a programmable DNA-regulated semisynthetic enzyme. *Angew. Chem. Int. Ed.* **46**, 3955–3958 (2007). doi:10.1002/(ISSN)1521-3773 Medline

80. M. Liu, J. Fu, C. Hejesen, Y. Yang, N. W. Woodbury, K. Gothelf, Y. Liu, H. Yan, A DNA tweezer-actuated enzyme nanoreactor. *Nat. Commun.* **4**, 2127 (2013). doi:10.1038/ncomms3127 Medline

81. A. J. M. Wollman, C. Sanchez-Cano, H. M. J. Carstairs, R. A. Cross, A. J. Turberfield, Transport and self-organization across different length scales powered by motor proteins and programmed by DNA. *Nat. Nanotechnol.* **9**, 44–47 (2014). doi:10.1038/nnano.2013.230 Medline

82. V. Noireaux, Y. T. Maeda, A. Libchaber, Development of an artificial cell, from self-organization to computation and self-reproduction. *Proc. Natl. Acad. Sci. U.S.A.* **108**, 3473–3480 (2011). doi:10.1073/pnas.1017075108 Medline

83. J. D. Puglisi, I. Tinoco Jr., Absorbance melting curves of RNA. *Methods Enzymol.* **180**, 304–325 (1989). doi:10.1016/0076-6879(89)80108-9 Medline

84. E. Protozanova, P. Yakovchuk, M. D. Frank-Kamenetskii, Stacked–unstacked equilibrium at the nick site of DNA. *J. Mol. Biol.* **342**, 775–785 (2004). doi:10.1016/j.jmb.2004.07.075 Medline

85. J. SantaLucia Jr., A unified view of polymer, dumbbell, and oligonucleotide DNA nearest-neighbor thermodynamics. *Proc. Natl. Acad. Sci. U.S.A.* **95**, 1460–1465 (1998). doi:10.1073/pnas.95.4.1460 Medline

86. D. Y. Zhang, Toward domain-based sequence design for DNA strand displacement reactions, in *DNA Computing and Molecular Programming*, vol. 6518, *Lecture Notes in Computer Science*, Y. Sakakibara, Y. Mi, Eds. (Springer, 2011), pp. 162–175.

87. J. M. Schaeffer, "Stochastic simulation of the kinetics of multiple interacting nucleic acid strands," thesis, California Institute of Technology, 2013.

88. I. G. Panyutin, P. Hsieh, The kinetics of spontaneous DNA branch migration. *Proc. Natl. Acad. Sci. U.S.A.* **91**, 2021–2025 (1994). doi:10.1073/pnas.91.6.2021 Medline

89. I. G. Panyutin, I. Biswas, P. Hsieh, A pivotal role for the structure of the Holliday junction in DNA branch migration. *EMBO J.* **14**, 1819–1826 (1995). Medline

90. S. A. McKinney, A. D. J. Freeman, D. M. J. Lilley, T. Ha, Observing spontaneous branch migration of Holliday junctions one step at a time. *Proc. Natl. Acad. Sci. U.S.A.* **102**, 5715–5720 (2005). doi:10.1073/pnas.0409328102 Medline

91. D. Soloveichik, CRN Simulator Mathematica Package, http://users.ece.utexas.edu/~soloveichik/crnsimulator.html [accessed 17 July 2017].

92. D. Soloveichik, Mathematica notebook and data files for displacillator mechanistic model, http://users.ece.utexas.edu/~soloveichik/supplementary/oscillator/mechanistic_model.zip [accessed 25 July 2017].